2008

Phase Transitions of Naphthalene and Naphthalene Derivatives Confined in Mesoporous Silicas

Janice Amabel Lee
Western University

Phase Transitions of Naphthalene and Naphthalene Derivatives Confined in Mesoporous Silicas

(Spine title: Phase Transitions of Confined Aromatics)

(Thesis format: Integrated-Article)

by

Janice Amabel Lee

Graduate Program
in
Chemistry

Submitted in partial fulfilment
of the degree of
Master of Science

/

School of Graduate and Postdoctoral Studies
The University of Western Ontario
London, Ontario
Canada

THE UNIVERSITY OF WESTERN ONTARIO
SCHOOL OF GRADUATE AND POSTDOCTORAL STUDIES

CERTIFICATE OF EXAMINATION

Supervisor

Dr. Yining Huang

Advisory Committee

Dr. Zhifeng Ding

Dr. Brian Pagenkopf

Examiners

Dr. John Corrigan

Dr. Nathan Jones

Dr. Mahi Singh

This thesis by

Janice Amabel Lee

entitled:

Phase Transitions of Naphthalene and Naphthalene Derivatives Confined in Mesoporous Silicas

is accepted in partial fulfillment of the
requirements for the degree of
Master of Science

Date: _____

Chair of the Thesis Examining Board
Dr. Rob Lipson

Abstract

The phase transitions of naphthalene and its 2-substituted methyl, methoxy, and chloro derivatives confined in mesoporous silicas were investigated by differential scanning calorimetry. A depression of phase transition temperature was observed. A comparison of the naphthalene in spherical and cylindrical pore systems was made, and the effect of molecular properties on the phase transition depression of the four compounds was investigated. It was found that depression and freeze-melt hysteresis is generally greater in spherical pores, and that electronic and size effects are contributing factors to transition temperature depression. Using powder X-ray diffraction it was found that while the crystal structure of confined naphthalene is the same as the bulk, there is a lattice expansion of the crystal. Furthermore, using differential scanning calorimetry and Raman spectroscopy it was shown on both a thermodynamic and molecular level that there is a non-freezing layer on the pore walls for each confined compound.

Keywords:

phase transition, mesoporous silica, confinement, naphthalene, 2-methylnaphthalene, 2-methoxynaphthalene, 2-chloronaphthalene, transition temperature depression, molecular effects, Raman, differential scanning calorimetry, hysteresis, contact layer, nanoporous materials

Acknowledgements

First and foremost I would like to express my sincere thanks and gratitude to my supervisor, Dr. Yining Huang. Without your guidance and encouragement this thesis would not be possible. The time you have spent having discussions with me and posing endless questions has not only pushed me to further my research and skills, but has taught me to look at science with a more critical eye. I truly appreciate this experience you have provided me.

I would like to thank the members of my advisory committee: Dr. Corrigan, Dr. Jones, Dr. Ding, and Dr. Pagenkopf. A speciai thanks to Dr. Corrigan for sending out my samples for TEM imaging in Germany, and also to Dr. Haralad Rösner for acquiring the images. Furthermore, I would like to express my gratitude to Dr. Baines and Dr. Ragogna for granting me unlimited use of their DSC equipment.

I would also like to thank the past and present members of the Huang lab group: Dr. Zhimin Yan, Dr. Banghao Chen, Dr. Jianfeng Zhu, Dongxu Li, Dr. Haiyan Wang, Andre Sutrisno, and Yueqiao Fu. I am very lucky to have been able to work alongside such an intelligent group of people. I appreciate all you have shared with me.

To my parents and my sister Constance, thanks for encouraging me throughout this project. Your love and support have kept me grounded. Con - thank you, really, for pointing out the dark circles under my eyes... just you wait! To my boyfriend Danoush, thank you for your patience and faith in me, and also for packing my lunch!

Finally, I would like to thank all my friends for their support and encouragement. You have managed to be there for me even from miles away.

Table of Contents

List of Tables

List of Figures

Glossary

A	surface area
C_P	heat capacity
D	diameter
G	Gibbs free energy
H_b	heat of bulk transition
H_c	heat of confined transition
$Hyst$	hysteresis
P	pressure
S	entropy
T	temperature
T_0	reference bulk transition temperature
V	volume
V_p	porous volume
V_{N_2}	nitrogen adsorption porous volume
ΔH_{sl}	enthalpy of solid-liquid transition
Δ	change in
Φ	heat flow
γ	surface tension
κ	integral mean curvature
λ	wavelength
μ	chemical potential
∂	partial derivative
π	pi
ρ	density
°C	degrees celcius
d_{hkl}	lattice spacing
f	Laplace curvature factor
m_{SiO_2}	mass of silica sample
m_{vp}	mass in contact layer

p/p_0	relative pressure
r_p	pore radius
t	thickness of contact layer
$\mathring{A}$	angstroms
BuOH	butanol
$C_{10}H_7CH_3$	methylnaphthalene
$C_{10}H_7Cl$	chloronaphthalene
$C_{10}H_7OCH_3$	methoxynaphthalene
$C_{10}H_8$	naphthalene
H_2SO_4	sulfuric acid
HCl	hydrochloric acid
NaOH	sodium hydroxide
BdB-FHH	Broekhoff-de Boer-Frenkel-Halsey-Hills
BET	Brunauer-Emmett-Teller
BJH	Barrett-Joyner-Halenda
CPG	controlled pore glass
CTAB	cetyltrimethylammonium bromide
DSC	differential scanning calorimetry
FWHH	full width at half height
MCF	mesocellular foam
MCM-41	Mobil Composition of Matter 41
MTS	micelle templated silica
PAH	polycyclic aromatic hydrocarbon
PEO	polyethylene oxide
PPO	polypropylene oxide
PSD	pore size distribution
SBA	Santa Barbara Amorphous

SSA	specific surface area
TEM	transmission electron microscopy
TEOS	tetraethyl orthosilicate
TMB	trimethyl benzene
XRD	X-ray diffraction

Chapter 1

General Introduction

1.1 Phase Transitions

With regards to the physical sciences, a phase is defined as a set of states of a physical macroscopic system which have relatively uniform chemical composition and physical properties such as density, compressibility, and magnetization.[1] While there are many examples of phases, the most familiar of them are solids, liquids, and gases.

A phase transition is defined as a thermodynamic transformation of a state of matter. For a phase transition to occur, energy must be added or removed from the system, and the distinguishing characteristic of this is an abrupt change in one or more physical properties with a small change in a thermodynamic variable such as temperature or pressure.[1,2] For example, phase transitions between solids, liquids, and gases can occur via evaporation, boiling, melting, freezing, or sublimation.

In the modern classification scheme, phase transitions are divided into two broad categories based on latent heat association: first-order and second-order phase transitions. First-order phase transitions are those which involve a latent heat; during such a transition a system either absorbs or releases a fixed amount of energy. Because energy cannot be instantaneously transferred between the system and the surroundings, first-order phase transitions are associated with "mixed-phase regimes" where some portions of the system have completed the transition while others have

not. Thus, although the Gibbs free energy is continuous, the system exhibits a discontinuous change in the first derivative (such as enthalpy, entropy, and volume) of the free energy. First derivatives can be expressed:[2]

$$\left(\frac{\partial G}{\partial P}\right)_T = V \tag{1.1}$$

$$\left(\frac{\partial G}{\partial T}\right)_P = -S \tag{1.2}$$

Solid/liquid/gas transitions fall into the category of first-order phase transitions.

Second-order phase transitions, such as ferromagnetic and superfluid transitions, are almost always associated with a disordering process. They have no associated latent heat and therefore no discontinuity in the first derivative of the Gibbs free energy. As such, entropy, enthalpy, and volume are continuous functions of temperature. Discontinuity is displayed in the second derivative of the free energy, such as heat capacity. This can be expressed:[2]

$$\left(\frac{\partial^2 G}{\partial T^2}\right)_P = -\left(\frac{\partial S}{\partial T}\right)_p = -\frac{C_P}{T} \tag{1.3}$$

A comparison of the Gibbs free energy G, entropy S and heat capacity C_P for first- and second-order transitions is shown in Figure 1.1. In the first-order transition, G is continuous but has a kink, and the first-order derivative S is discontinuous. The second-derivative C_P therefore has a singularity. In the second-order transition, G is also continuous but has no kink, while the first-order derivative S does have a kink. The second-order derivative C_P is discontinuous.

In the present study we are concerned with first-order phase transitions, specifically solid-liquid transitions. At the transition temperature T, the system is in phase equilibrium, which necessarily means that the chemical potentials μ, or Gibbs free

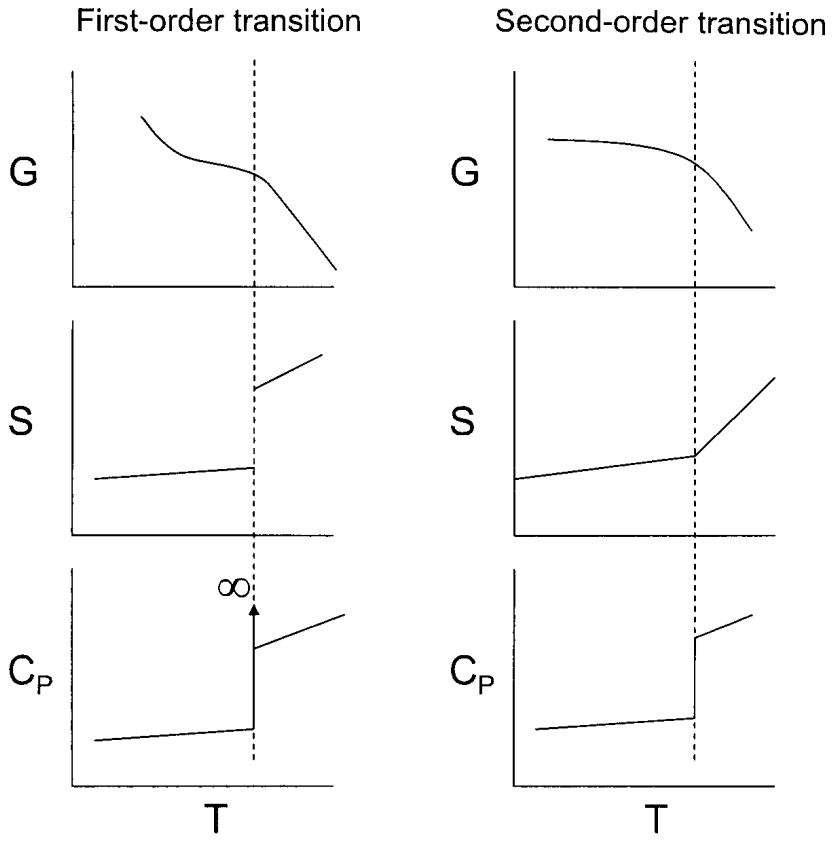

Figure 1.1. Schematic comparison of G, S, and C_P for first- and second-order transitions.

energies G are equal. Thus $\Delta\mu = 0$ and $\Delta G = 0$. If either the temperature T or pressure P is changed, the other must change to keep this equality, and so the changes in chemical potentials of both phases α and β must be equal: $d\mu_\alpha = d\mu_\beta$.[2] Because $\mu = -SdT + VdP$, this can be rewritten:

$$-S_\alpha dT + V_\alpha dP = -S_\beta dT + V_\beta dP \tag{1.4}$$

The ratio of pressure change to temperature change can then be calculated:

$$\frac{dP}{dT} = \frac{S_\alpha - S_\beta}{V_\alpha - V_\beta} = \frac{\Delta S}{\Delta V} \tag{1.5}$$

It is known that:

$$\Delta G = \Delta H - T\Delta S \tag{1.6}$$

therefore:

$$\Delta S = \frac{\Delta H}{T} \tag{1.7}$$

where ΔH is the latent heat of the transition at constant temperature and pressure. The change of the pressure and temperature of a phase transition are therefore related as:

$$\frac{dP}{dT} = \frac{\Delta H}{T\Delta V} \tag{1.8}$$

This is known as the Clapeyron equation, which describes the thermodynamics of first-order transitions.[2]

1.2 Confined Phase Transitions

While phase transitions of bulk materials have been well-studied, less is known about the phase transitions of confined materials. Phase change in porous media is a broad subject, encompassing the gas, liquid, or solid phases occupying the pore space or the solid matrix of the porous medium itself.[3] Currently there is considerable interest in the behaviour of materials in confined geometry, in particular the behaviour of liquids in porous substances and, more recently, in the formation of solids of restricted dimensions on the nanoscale.[4]

It is well known that the properties of materials confined in pores differ from those of their bulk counterparts due to geometrical confinement and interaction with the surface of the pore wall.[5] Most commonly observed are the hysteresis between freezing and melting cycles and the shift in phase transition temperatures.[6,7] The topic of phase transitions of confined materials is of considerable importance in commercial areas such as catalysis, interfacial adhesion, and separation science.[8] It also serves practical interest in such areas as frost heave and weathering of rocks.[9] In the last twenty years there has been an incredible expansion in research devoted to the controlled preparation of nanocrystals using porous materials as nanoreactors.[10] However, crystallization in confining media is not well understood.[11]

The Gibbs-Thomson equation[12,13] relates the temperature shift ΔT of crystallization to the pore size of the confining material according to:[12,14,15]

$$\frac{\Delta T}{T_0} = -2\frac{\gamma_{sl}}{r_p}\frac{\nu_s}{\Delta H_{sl}} \tag{1.9}$$

where T_0 is the bulk transition temperature, γ_{sl} the solid-liquid surface tension, ν_s the molar volume of the solid phase, r_p the pore radius, and ΔH_{sl} the latent heat of the solid-liquid transition. According to this equation the shift of the transition temperature of a confined liquid is inversely proportional to the radius of the pore in which it is confined.

However, it is known that not all of the solvent takes part in the transition; a significant portion of it remains adsorbed to the pore surface. As a result, the Gibbs-Thomson equation has been shown to inadequately describe some systems. Equation (1.9) should therefore be reformulated to include the thickness t of this adsorbed layer:[11]

$$\Delta T = \frac{k}{\Delta H_{sl}(r_p - t)} \tag{1.10}$$

where the value of t is traditionally determined by a calibration procedure using materials containing various pore sizes. The problem with this method is the underlying assumption that the thickness t does not vary with pore size. Meziane *et al.*[11] proposed a different method of measuring t which allows for the determination of its value specific to a certain pore size.

Much of the previous research on phase transitions of confined materials was conducted in porous systems such as Vycor glasses, controlled porous glasses (CPG), or porous silica.[4,6,8,16] However, these materials exhibit broad pore size distributions, inducing disorder which complicates the interpretation of results.[17] More recent research has turned its focus to mesoporous media with simple geometry instead. Specifically, mesoporous silicas are well-ordered and are characterized by narrower pore size distributions, lending advantage over CPG and Vycor glasses.[4]

1.3 Mesoporous Materials

Since the discovery of Mobil Composition of Matter (MCM)-41 and related M41S family molecular sieves by Mobil Research Scientists in the early 1990's,[18,19] mesoporous materials have become a current and intensive research field because they hold much potential in an extensive range of applications;[20] these include heterogeneous catalysis, adsorption, separation, drug delivery, development of advanced materials for electronic and optical devices and luminescence applications.[21,22]

While previously discovered molecular sieves were microporous, having a range of approximately 0.2 to 1.2 nm, the M41S materials allowed for mesoporous (>2 nm) molecular sieves. Of particular interest is MCM-41, a molecular sieve which is charaterized by a hexagonal array of relatively large and uniform pores, large surface areas (up to 1000 m^2/g), and narrow pore size distributions.[18] It is synthesized in the presence of surfactants, discussed in Section 1.3.1, which allow for the formation of

regular arrays of uniform channels.[19] By varying the chain length of the surfactant molecule, Beck *et al.*[18] were able to tailor the MCM-41 pore sizes from 1.5 to 4.5 nm. Furthermore, the use of swelling agents, discussed in Section 1.3.3, has been shown to expand the range of pore sizes accessible to MCM-41. However, the upper limit of diameters was generally approximately 10.0 nm.[22]

To overcome these limitations, Zhao *et al.*[23,24] synthesized Santa Barbara Amorphous (SBA) type materials which have reported pore sizes ranging from 2 to 30 nm. Instead of surfactants, SBA-15 is prepared using non-ionic block copolymers in acidic media. Block copolymers are discussed in Section 1.3.2.

SBA-15 was initially thought to be more or less a large-pore equivalent of MCM-41 mesoporous silica. Like MCM-41, SBA-15 has a well-ordered hexagonal mesoporous silica structure.[21] However, the framework of SBA-15 contains mesoporous channels interconnected by micropores; this is one of the fundamental differences between SBA-15 and MCM-41-type materials and is crucial to the further development of block copolymer-directed silicas.[25] With regard to this, many studies have attempted to determine whether possibilities for control and tailoring of these micropores exist.[26,27]

SBA-15 is also characterized by higher thermal and hydrothermal stability than MCM-41 because of its large wall thickness; the lack of hydrothermal stability in MCM-41 is a considerable drawback in applications requiring the presence of water.[21,28] It has been shown by Zhao *et al.*[28] that SBA-15 materials are stable for at least 48 hours in boiling water. Furthermore, the textural properties of SBA-15 can easily be controlled by variation of experimental conditions such as reaction time, aging time and temperature, and the amount of hydrophobic swelling agent. A schematic of SBA-15 formation is shown in Figure 1.2.

Exploiting the tunability of MCM-41 and SBA-15, it is possible to access cylindrical pores ranging from about 1.5 to 15 nm.

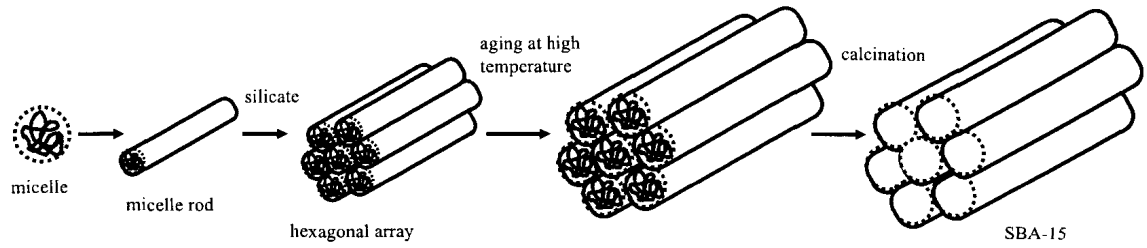

Figure 1.2. Schematic of non-ionic copolymer-templated formation of SBA-15.

1.3.1 Surfactants

Surfactants play a central role in directing the formation of the inorganic mesostructure from soluble silica species.[29] For this reason, the surfactants are often referred to as *structure-directing agents.*[30] They have small, usually ionic hydrophilic head groups with hydrophobic alkyl tails[23] and form a micellar system in solution through the favourable hydrophobic interactions between surfactant chains. Due to the preferential interaction of the negatively charged silica moieties with the positively charged ammonium group of the surfactant, the soluble silicate precursors settle on the heads which are located on the external surface of the micelles. Calcination of this material removes the surfactant, leaving behind MCM-41.[29] Specifically, MCM-41 utilizes quaternary trimethylammonium cations $C_nH_{2n+1}(CH_3)_3N^+$ (C_nTMA^+, $8 < n < 18$) as structure directing agents. Of these, C_{16}TMABr (CTAB) has been found to be most useful.[29] Beck *et al.*[18] were able to tailor the MCM-41 pore sizes from 1.5 to 4.5 nm by varying the chain length of C_nTMA^+ cations.

1.3.2 Block Copolymers

Nonionic poly(ethylene oxide) surfactants and poly (alkylene) block copolymers have been widely used in emulsifying, defoaming/antifoaming, coating, thickening, solubilizing, cleaning, lubricating, wetting, pharmaceutical, coal and petrochemical industries as well as household applications.[31–34] Curiosity regarding poly(ethylene oxide)-poly(propylene oxide)-poly(ethylene oxide) (PEO_x-PPO_y-PEO_x) triblock copolymers arose during the past decade due to their wide range of applications as nonionic surface-active agents[35–38] that are able to, as supramolecular templates, impart large pores and thick walls.[30] Furthermore, their unique behaviour has been of fundamental interest in physics.[39] Because of their mesostructural ordering properties, amphiphilic nature, low cost-commercial availability and biodegradability, PEO-PPO-PEO copolymers make excellent candidates for structure-directing agents.[24,40]

The advantage of using block copolymers for templation is that their ordering properties can be nearly continuously tuned by adjusting solvent composition, molecular weight, or copolymer architecture. Furthermore, they permit solution organization of larger structural features than is possible with low-molecular-weight surfactants. This is achieved from lower solution concentrations. The overall strategy of utilizing block copolymers in materials synthesis can be applied to any self-assembling surfactant or copolymer system in which a network-forming additive is selectively partitioned among different mesostructured components.[40]

These block copolymers posses much longer hydrophilic and hydrophobic chain lengths than surfactants[24] and thus introduce several effects which are of importance to the phase behaviour of the micellar systems (Figure 1.3) and silica materials they template. Firstly, due to the long chain hydrophilic group, hydration and entropy effects are very significant in determining the shape of the hydrophilic block and the volume it occupies.[23] Moreover, the specific nature of the interactions of PEO and

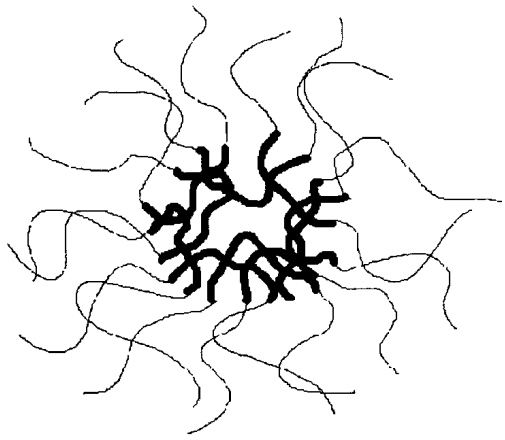

Figure 1.3. Micelle formed by block copolymer P123. Dark and light portions represent the hydrophobic PO and hydrophilic EO chains, respectively.

PPO with water affords aqueous solutions with a dramatic temperature dependency; while PPO is water soluble at temperatures below approximately 15 °C, it aggregates at higher temperatures. On the other hand, PEO is largely hydrophilic within the temperature range of 0 to 100 °C.[41] It follows that at low temperatures all PEO-PPO-PEO triblock copolymers display the characteristics of fully dissolved polymers, whereas at elevated temperatures aggregates are formed due to the PPO hydrophilic-to-hydrophobic transition.[35] Various architectures, denoted generically by PEO_x-PPO_y-PEO_x, have been studied. Additionally, it was found that the core size of the micelles tended to increase with decreasing x and increasing temperature.[35]

Solubilization of nonionic poly(alkylene oxide) block copolymers in aqueous media is due to the association of water molecules with the alkylene oxide moities through hydrogen bonding.[31] This interaction is enhanced in acidic media where hydronium ions, instead of water molecules, associate with the alkylene oxygen atoms thus adding long-range Coulombic interactions to the co-assembly process.[40]

SBA-15 is prepared using PEO_x-PPO_y-PEO_x, specifically P123 ($EO_{20}PO_{70}EO_{20}$),

as a micelle-forming templating agent. During synthesis, the use of concentrations of PEO-PPO-PEO higher than 6% by weight will result in either silica gel or no silica precipitation at all. Conversely, concentrations below 0.5% by weight will generate amorphous silica only.[24]

1.3.3 Swelling Agents

Swelling agents can be introduced to supramolecular templated systems in order to increase pore size. This occurs by the preferential solubilization of the additive into the surfactant or PEO-PPO-PEO hydrophobic micelle core. 1,3,5-Trimethylbenzene (TMB, mesitylene) has been used to swell the pore diameters of MCM-41 materials from 4 to 10 nm while maintaining the hexagonally packed pore structure.[19,23] In the same way, TMB can also be introduced to SBA-15 to increase pore size past 4-12 nm.

In a study by Lettow *et al.*,[23] it was found that varying the P123:TMB mass ratio had different effects on the pore morphology as shown in Figure 1.4. At a ratio of 0.2, there was a significant increase in the pore size of the mesoporous SBA-15 material while maintaining long, straight cylindrical pores. At ratios of 0.2-0.3, however, TEM imaging indicates a change in pore morphology in which the walls of the cylindrical pores begin to buckle, forming spherical nodes down the length of the pores. Above a ratio of 0.3 the mesoporous material no longer matches the highly ordered *p6mm* space group; instead it is transformed into a mesostructured cellular foam (mesocellular foam, MCF) composed of uniformly sized, large spherical cells which are interconnected by uniform windows, thus forming a continuous 3D pore system. The interconnected nature of these large uniform pores render MCFs promising candidates for catalyst supports and also in separations involving large molecules such as proteins.[42,43]

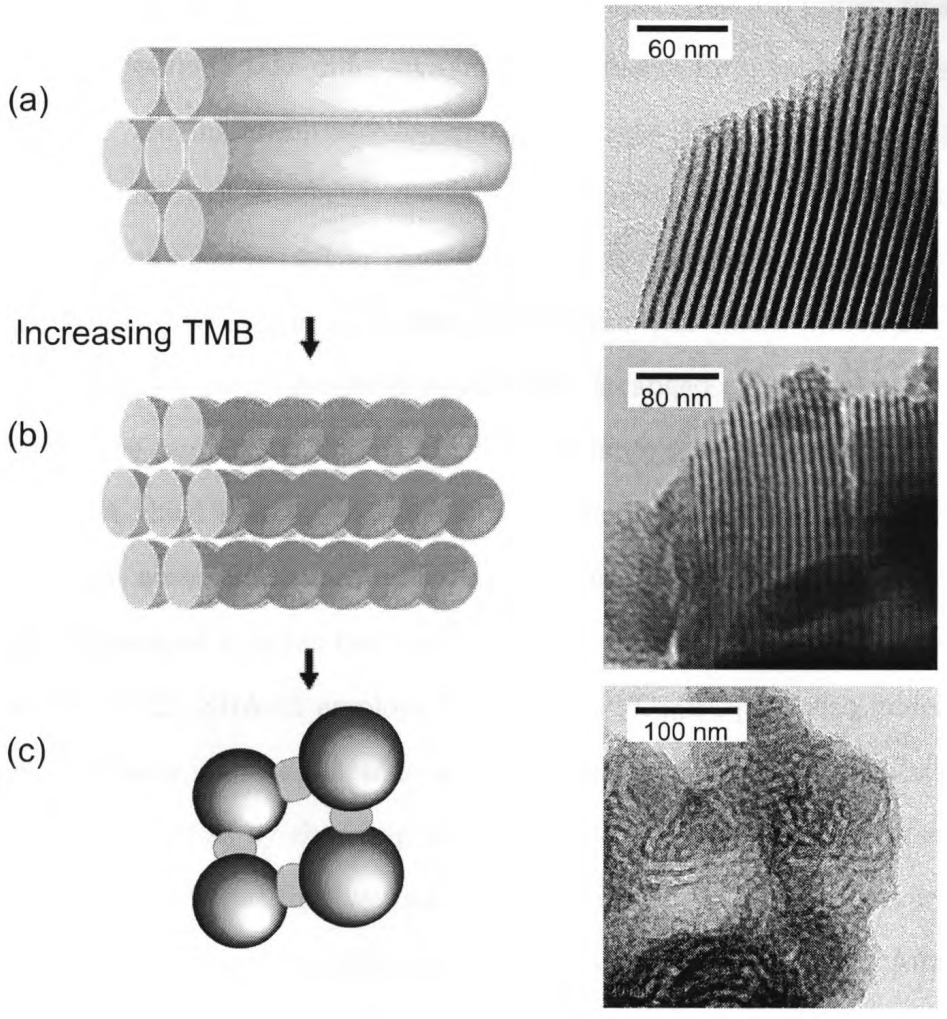

Figure 1.4. Progression of the morphological transition in P123- templated materials swollen by TMB. The proposed schemes of formation and TEM micrographs of the mesoporous silicas synthesized at TMB/P123 mass ratios of (a) 0.00, (b) 0.21, and (c) 0.50 are illustrated.[23]

1.4 Spherical Mesopores

While mesocellular foams provide access to spherical mesopores measuring approximately 24 - 42 nm in diameter,[44] they cannot form smaller spherical pores. To address this issue, it is possible to take different synthetic routes to form spherical mesopores of varying sizes. For instance, micelle-templated silicas (MTS) are also built from a cooperative assembly of micelles and silicates, employing cetyltrimethylammonium bromide (CTAB) as a surfactant in basic conditions.[45–47] Varying the TMB/CTAB ratio from 0 to 13, Ottaviani *et al.*[45] were able to synthesize MTS materials ranging from 4 to 11 nm. Low ratios rendered hexagonally arranged cylindrical pores, while at a ratio of 13 the sample was described as having large pores resembling connected soap bubbles. A third method of synthesizing spherical cavities yields SBA-16, a mesoporous silica with interconnected cage-like pores.[48] SBA-16 is a cubic material with the pores arranged in cubic body-centered $Im\bar{3}m$ symmetry.[28] Whereas SBA-15 is templated by P123, SBA-16 employs F127 ($EO_{106}PO_{70}EO_{106}$), also under acidic conditions. Similarly, pore diameters can be tuned by varying reaction time and temperature,[49] as well as by changing the quantity of swelling agent. In a study by Kleitz *et al.*,[50] it was found that varying the molar ratios of the silica precursor and BuOH swelling agent gave rise to spherical pores between 4.7 and 7.2 nm. Among the aforementioned spherical-pored materials, it is possible to access such pore geometry ranging from diameters of 4.7 to 42 nm.

1.5 Aim of Present Work

Although studies regarding confined phases have been already conducted on simple organics such as water, benzene, and cyclohexane,[8,51–53] many others have not been explored in detail. As such, one goal of our research is to examine the confinement

effects on the phase behaviour of naphthalene confined in cylindrical mesopores, and, in the interest of the effects of molecular properties on confinement, we also study several naphthalene derivatives.

Furthermore, while there is considerable interest in the behaviour of fluids confined within simple geometries, the number of studies conducted on slit and cylindrical pores[54–59] far outweighs those regarding spherical pores.[60–62] Another goal of our research is to examine the phase behaviour of naphthalene confined in mesoporous silicas with spherical pore geometries and compare the results to those of the cylindrical-pored system.

To characterize our silica materials we utilize nitrogen adsorption porosimetry, which is capable of assessing a very wide range of pore sizes. We examine the phase transitions of confined naphthalene and its derivatives using differential scanning calorimetry as the primary experimental method. This technique quickly identifies thermal effects over a large temperature range, allowing us to easily determine relevant temperatures and characteristic caloric values of naphthalene in varying degrees of confinement.

1.6 Characterization Methods

1.6.1 Nitrogen Adsorption Porosimetry

Adsorption can be thought of as the enrichment of one or more components at an interface and in gas adsorption it is the gas/solid interface that is considered. The solid is termed the *adsorbent* and the gas, which has the capacity to be adsorbed, is termed the *adsorptive*. Once in the adsorbed state, the fluid is called the *adsorbate*.[63]

There exist two types of adsorption: chemical and physical. The former is also referred to as irreversible adsorption or chemisorption. It is characterized by large

interaction potentials and involves true chemical bonding between the adsorptive and the surface of the adsorbent. Compared to physical adsorption, chemisorbed molecules are more localized to the surface due to the formation of a chemical bond and presents potential problems in surface area analysis in that the spacing between adsorbed molecules depends on the adsorbent surface structures as well as the size of the adsorbate itself.[64]

Since chemical bonding is involved, chemisorption is often found to occur at temperatures above the critical temperature of the adsorbate,[65] and as chemical bonding necessarily entails a chemical reaction, an activation energy is involved in this process. The nature of chemisorption also restricts it to a single layer, at most, of the adsorbate on the adsorbent.

Physical adsorption, also termed reversible adsorption or physisorption, is a general phenomenon occurring whenever an adsorptive is brought in contact with the surface of the adsorbent. It refers to the adhering of gas molecules to a surface at a pressure below the vapor pressure through interactions much weaker than ionic or covalent interactions.[64] Because the adsorption process is reversible, we will refer to the experiment itself (adsorption plus desorption event) as *sorption* to avoid confusion.

Fluids in contact with a planar surface form a multilayer adsorbed film where the thickness of the film can increase without limit. Within pores, however, the film thickness cannot grow unlimited because the film stability depends on the attractive fluid-wall interactions, surface tension, and curvature of the liquid-vapor interface. At a critical thickness, the attraction between fluid molecules in mesopores will give rise to capillary condensation (pore filling). This refers to the phenomenon in which a gas condenses into a liquid-like phase in pores at a pressure p less than the saturation pressure p_0 of the bulk fluid.[65] A characteristic feature associated with capillary condensation is sorption hysteresis,[66] where the evaporation of the adsorbate occurs at a pressure lower than the condensation pressure.

A sorption isotherm is the measurement of the amount adsorbed versus relative adsorptive pressure p/p_0 at a constant temperature. The size and shape of the isotherm depends on the interplay between the strength of fluid-wall and fluid-fluid interactions as well as the effects of confined pore space on the state and thermodynamic stability of the confined fluid. It is therefore possible to determine the pore shape from the isotherm. There are six different classes of isotherms as shown in Figure 1.5 named Type I through VI. The materials prepared for our studies present Type IV isotherms, which are typical for mesoporous materials. This isotherm type is characterized by a high energy of adsorption and a hysteresis loop.[64] The lower branch represents the adsorption event (increasing p) while the upper branch depicts the desorption event (decreasing p). The inflection points at the base and the top of the loop indicate sudden pore filling and pore evaporation, respectively, where evaporation occurs at a lower pressure than filling thus giving rise to the hysteresis loop.

There are four types of hysteresis loops named H1 through 4 shown in Figure 1.6. Our spherical-pored materials give rise to H2 loops which are associated with interconnectivity of porous networks, where pore blocking effects may play a role during evaporation from a pore that only has access to the external gas phase through narrow constrictions. The desorption branch of the hysteresis loop is steeper than the adsorption branch because it reflects a percolation transition.[23] Our cylindrical pores give rise to H1 loops, which are associated with porous materials consisting of well-defined cylindrical-like pore channels.[65]

A number of methods exist which can be used to treat sorption data in order to extract information regarding porous materials such as pore size and distribution, volume, and surface area. The BET[67] and BJH[68] methods are commonly used but somewhat limited in accuracy, while the more accurate BdB method[69,70] is difficult to apply and therefore not widely used. We utilize a simplified version of this method

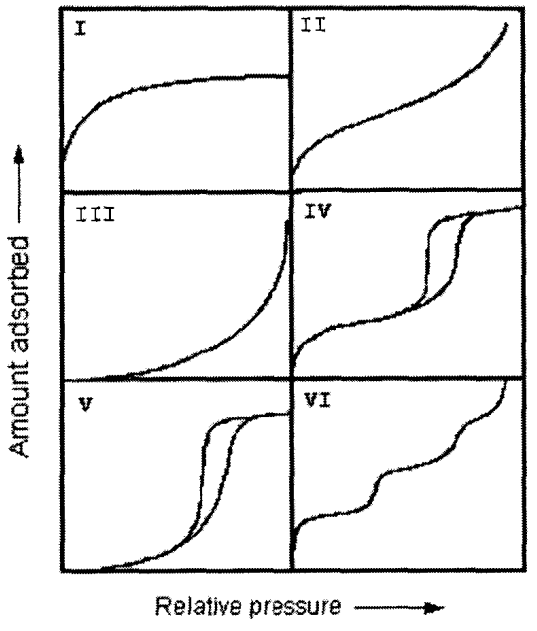

Figure 1.5. Classification of sorption isotherms.

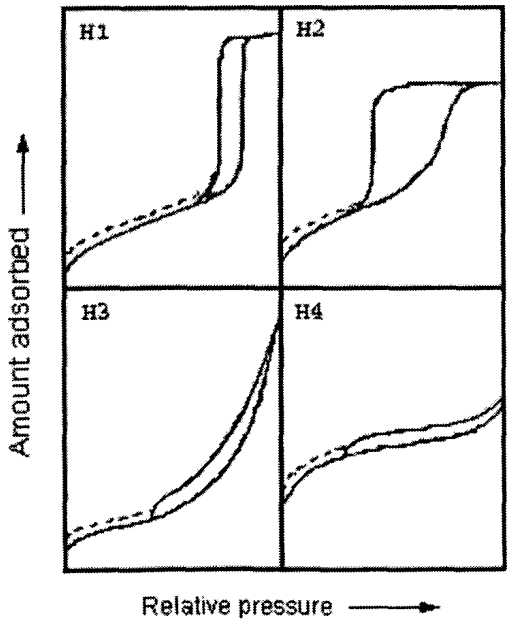

Figure 1.6. Classifications of hysteresis loops.

called BdB-FHH.[71] These methods will be addressed in Section 3.1.

1.6.2 Differential Scanning Calorimetry

The objective of calorimetry is to measure heat, which necessarily means heat must be exchanged. The exchanged heat tends to effect a temperature change in a body; this may then be used as a measure of the quantity of heat exchange. The process of heat exchange can be connected with a heat flow which leads to local temperature differences along its path; this can serve as a measure of the flowing heat.[72] Differential scanning calorimetry (DSC) is a thermal technique in which differences in heat flow into a substance and a reference are measured as a function of sample temperature while the two are subjected to a controlled temperature program. An attractive feature of DSC is that measurements can be obtained using sample quantities in the milligram range.

There exist two types of differential scanning calorimeters: the heat flux DSC and the power compensation DSC. Both use a *differential method of measurement* whereby the sample is compared with a quantity of the same kind of known value (reference sample), and the difference between the two values is measured.[73] The characteristic feature of all DSC measuring systems is the twin-type design and direct in-difference connection of the two measuring systems. The advantage of this is that disturbances to the system such as temperature fluctuations in the environment and measuring equipment affect both measuring systems in the same way and are compensated when the differential signal is formed. Furthermore, this signal can be strongly amplified as the high base signals of the individual measuring systems are also compensated when the difference between them is formed.[72]

The DSC machine can also be heated or cooled at the desired heating or cooling rate. This dynamic operational mode distinguishes it from classic calorimeters.[72]

Moreover, with most classic calorimeters, the measured signal is proportional to a heat; with DSC the measured signal is proportional to a heat flow rate Φ, which allows time dependencies of a transition to be observed on the basis of the $\Phi(t)$. The direct measurement of heat flow rates allows the DSC to solve values such as heat capacity and heats of reaction.

The output from a DSC experiment is a thermogram in which the heat flow or power, usually given in mW, is plotted against temperature. A representative thermogram is shown in Figure 1.7. Crystallization is an exothermic process so the peak, denoted T_c, rises above the baseline when the heat flow increases up the y-axis. The melting peak is denoted T_m and appears below the baseline because it is an endothermic event.

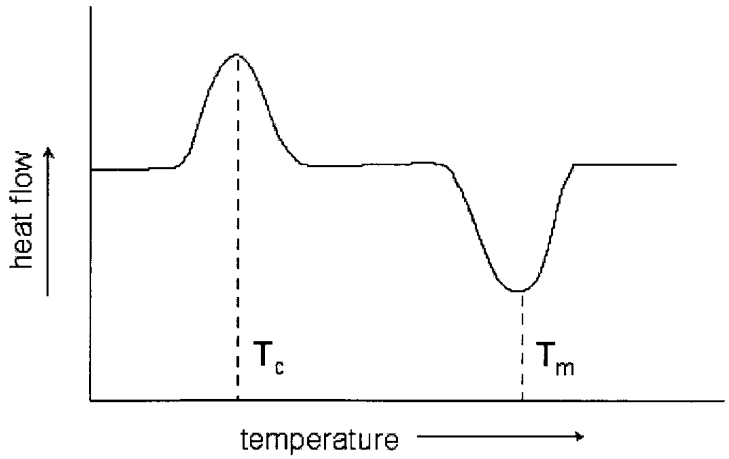

Figure 1.7. Representative thermogram depicting crystallization (T_c) and melting (T_m) events.

1.6.3 Raman Spectroscopy

When light is scattered from a particle, most photons undergo Rayleigh or elastic scattering; that is, they have the same energy and wavelength as the incident photons.

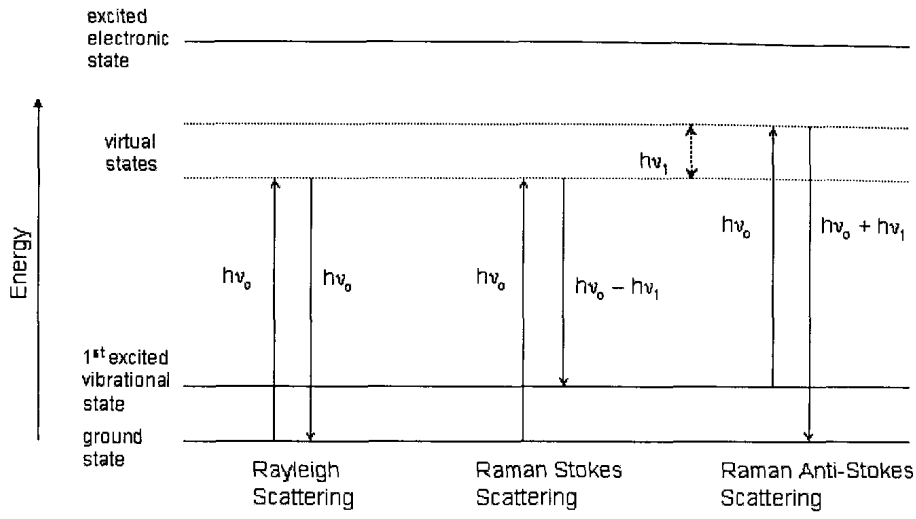

Figure 1.8. Origin of Rayleigh and Raman scattering

However, a small fraction of the scattered light ($\sim 1/10^6$ photons) is inelastically scattered by an excitation. These photons have a different frequency than that of the incident photons and this is referred to as Raman scattering. It occurs because the electron cloud can be perturbed by molecular vibrations; it is possible for the optical (incident light) and vibrational oscillations to interact to produce Raman scattering. Raman scattering is much weaker than the incident beam ($\sim 10^{-5}\nu_0$; ν_0= incident beam). Its frequency is equivalent to $\nu_0 \pm \nu_m$, where ν_m is the vibrational frequency of the molecule. Stokes scattering is generated when a molecule is excited from the ground state to a virtual energy state and then relaxes into a vibrational excited state ($\nu_0 + \nu_m$). If the molecule was already in an elevated vibrational energy state, anti-Stokes scattering is generated as the molecule relaxes back to the ground state ($\nu_0 - \nu_m$). Rayleigh and Raman scattering are shown in Figure 1.8.

Raman spectra are acquired by irradiating a sample with a powerful laser source, and the scattered radiation is measured using a spectrometer. The oscillating electric field of the incoming light induces a polarization in the sample molecule, and this

short-lived distortion of the electron cloud is indicated as the virtual state in Figure 1.8. In the acquired spectra, the difference in energy between the incident and scattered photons is represented by the Raman shift in wavenumbers (cm^{-1}):

$$\triangle\nu = \frac{1}{\lambda_{incident}} - \frac{1}{\lambda_{scattered}} \tag{1.11}$$

Raman spectroscopy is useful for aqueous samples as water is Raman-inactive, and also for samples which must be contained in glass or quartz cells. As silicates are weak Raman scatterers, this type of spectroscopy is appropriate for the study of aromatics confined in mesoporous silicas.

1.6.4 Powder X-ray Diffraction

X-ray diffraction is the most widely used and least ambiguous method for the precise determination of the positions of atoms in molecules and crystalline solids.[74] X-rays interact with electrons; when an X-ray beam strikes a material it is scattered in various directions by the electron clouds of the atoms. If the wavelength of the X-rays is comparable to the separation between atoms, interference can occur. Interference maxima and minima will result if the scattering centers are in an ordered array, such as atoms in a crystalline solid.

X-rays interact with planes of atoms in the three-dimensional lattices of the crystal structure. The lattices show the translational symmetry of the structure, and each plane is a representative member of a parallel set of equally spaced planes. The planes are described by labels called Miller indices, denoted h, k, and l, and can take values of positive or negative integers or zero. The Miller indices are given by the reciprocals of the fractional intercepts h,k,l along the unit cell directions a,b,c, respectively. The separation between the planes is the d-spacing, denoted d_{hkl}.

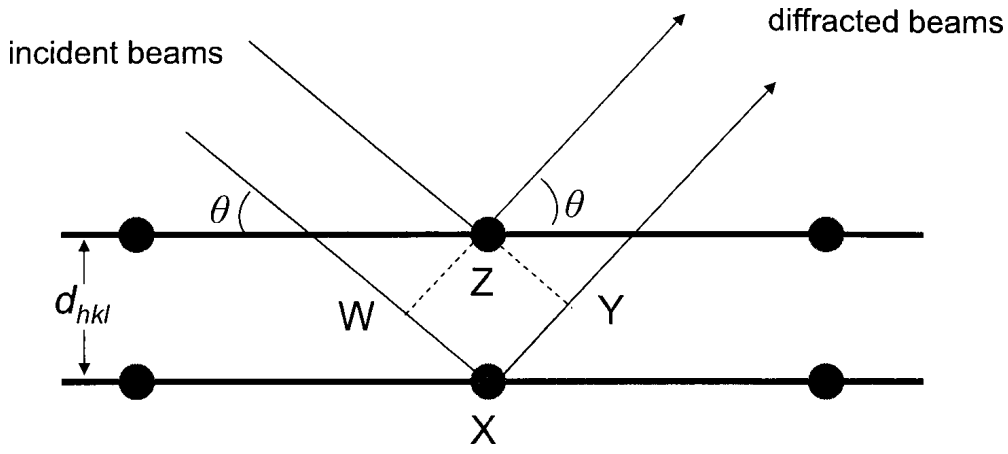

Figure 1.9. Reflection of X-rays from two parallel planes of atoms.

Figure 1.9 shows the scattering of X-rays from a set of planes. The scattering of the X-ray beam will provide useful data if the scattered beam from the points X and Z produce diffracted beams which are in phase. For this to occur, it is necessary that the extra distance traveled by X-ray photon from W to X to Y is an integral number of wavelengths. It is clear that this path difference depends on the d-spacing and the angle of incidence θ of the beam, and this is described by the Bragg equation:

$$Path\ difference = WX + XY = 2d_{hkl}sin\theta = n\lambda \tag{1.12}$$

where n is an integer representing the order of the diffraction maximum, typically treated as 1. The X-ray diffraction pattern displays the intensity of diffraction maxima as a function of the detector angle 2θ.

References

[1] Chang, R. *General Chemistry: The Essential Concepts, 4th Edition*; McGraw Hill, New York, 2006.

[2] Noggle, J. H. *Physical Chemistry, 3rd Edition*; Harper Collins Publishers Inc., New York, 1996.

[3] Yortsos, Y. C.; Stubos, A. K. *Curr. Opin. Colloid In.* **2001**, *6*, 208–216.

[4] Booth, H. F.; Strange, J. H. *Mol. Phys.* **1999**, *15*, 5403–5409.

[5] Smirnov, P.; Yamaguchi, T.; Kittaka, S.; Kuroda, Y. *J. Phys. Chem. B* **2000**, *104*, 5498–5504.

[6] Mu, R.; Zue, Y.; Henderson, D. O.; Frazier, D. O. *Phys. Rev. B* **1996**, *53*, 6041–6047.

[7] Morishige, K.; K., K. *J. Chem. Phys.* **2000**, *112*, 11023–11029.

[8] Jackson, C. L.; McKenna, G. B. *J. Chem. Phys.* **1990**, *93*, 9002–9011.

[9] Christenson, H. K. *J. Phys.: Condens. Matter* **2001**, *13*, R95–R133.

[10] Pileni, M. P. *J. Chem. Phys. B* **2001**, *105*, 3358–3371.

[11] Meziane, A.; Grolier, J.-P. E.; Baba, M.; Nedelec, J. M. *Faraday Discuss.* **2007**, *136*, 384–394.

[12] Gibbs, J. *Collected Works*; Yale University Press: New Haven, CT, 1928.

[13] Thomson, S. W. *Philos. Mag.* **1871**, *42*, 448.

[14] Faivre, C.; Bellet, D.; Dolino, G. *Eur. Phys. J. B* **1999**, *7*, 19–36.

[15] Petrov, O.; Furó, I. *Phys. Rev. E* **2006**, *73*, 011608–1 – 7.

[16] Jackson, C. L.; McKenna, G. B. *Chem. Mater.* **1996**, *8*, 2128–2137.

[17] Dosseh, G.; Xia, Y.; Alba-Simionesco, C. *J. Phys. Chem. B* **2003**, *107*, 6445–6453.

[18] Beck, J. S.; Vartuli, J. C.; Roth, W. J.; Leonowicz, M. E.; Kresge, C. T.; D.Schmitt, K.; Chu, C. T.-W.; Olson, D. H.; Sheppard, E. W.; McCullen, S. B.; Higgins, J. B.; Schlenker, J. L. *J. Am. Chem. Soc.* **1992**, *114*, 10834 – 10843.

[19] Kresge, C. T.; Leonowicz, M. E.; Roth, W. J.; Vartuli, J. C.; Beck, J. S. *Nature* **1992**, *359*, 710–712.

[20] Sousa, A.; Sousa, E. M. B. *J. Non-Cryst. Solids* **2006**, *352*, 3451–3456.

[21] Klimova, T.; Esquivel, A.; Reyes, J.; Rubio, M.; Bokhimi, X.; Aracil, J. *Microporous Mesoporous Mater.* **2006**, *93*, 331–343.

[22] Katiyar, A.; Yadav, S.; Smirniotis, P. G.; Pinto, N. G. *J. Chromatogr. A* **2006**, *1122*, 13–20.

[23] Lettow, J. S.; Han, Y. J.; Schmidt-Winkel, P.; Yang, P.; Zhao, D.; Stucky, G. D.; Ying, J. Y. *Langmuir* **2000**, *16*, 8291–8295.

[24] Zhao, D.; Feng, J.; Huo, Q.; Melosh, N.; Fredrickson, G. H.; Chmelka, B. F.; Stucky, G. D. *Science* **1998**, *279*, 548–552.

[25] Kleitz, F.; Kim, T.-W.; Ryoo, R. *Bull. Korean Chem. Soc.* **2005**, *26*, 1653–1668.
[26] Ravikovitch, P. I.; Neimark, A. V. *J. Phys. Chem. B* **2001**, *105*, 6817–6823.
[27] Imperor-Clerc, M.; Davidson, P.; Davidson, A. *J. Am. Chem. Soc.* **2000**, *122*, 11925–11933.
[28] Zhao, D.; andd J. Feng, Q. H.; Chmelka, B. F.; Stucky, G. D. *J. Am. Chem. Soc.* **1998**, *120*, 6024–6036.
[29] Soler-Illia, G. J. A. A.; Sanchez, C.; Lebeau, B.; Patarin, J. *Chem. Rev.* **2002**, *102*, 4093–4138.
[30] Soler-Illia, G. J. A. A.; Sanchez, C.; Lebeau, B.; Patarin, J. *Current Opinion Coll. Inter. Sci.* **2003**, *8*, 109–126.
[31] Chu, B.; Zhou, Z. *Nonionic Surfactants: Polyoxyalkylene Block Copolymers*; Marcel Dekker: New York, 1987; Vol. 60.
[32] Sjöblom, J.; Stenius, P.; Danielsson, I. *Nonionic Surfactants: Physical Chemistry*; Marcel Dekker: New York, 1987; Vol. 23.
[33] Meziani, A.; Tourand, D.; Zradba, A.; Pulvin, S.; Pezron, I.; Clausse, M.; Kunz, W. *J. Phys. Chem. B* **1997**, *101*, 3620–3625.
[34] Schmolka, I. R. *Polymers for Controlled Drug Delivery*; CRC Press, 1991.
[35] Mortensen, K.; Brown, W. *Macromolecules* **1993**, *26*, 4128–4135.
[36] Mortensen, K.; Brown, W.; Norden, B. *Phys. Rev. Lett.* **1992**, *68*, 2340–2343.
[37] Ishoy, T.; Mortensen, K. *Langmuir* **2005**, *21*, 1766–1775.
[38] Cohn, D.; Lando, G.; Sosnik, A.; Garty, S.; Levi, A. *Biomaterials* **2005**, *27*, 1718–1727.
[39] Mortensen, K. *Europhys. Lett.* **1992**, *19*, year.
[40] Zhao, D.; Huo, Q.; Chmelka, J. F. B. F.; Stucky, G. D. *J. Am. Chem. Soc.* **1998**, *120*, 6024–6036.
[41] Mortensen, K.; Pedersen, J. S. *Am. Chem. Soc.* **1993**, *26*, 805–812.
[42] Schmidt-Winkel, P.; Lukens, W. W., Jr; Zhao, D.; Yang, P.; Chmelka, B. F.; Stucky, G. D. *J. Am. Chem. Soc.* **1999**, *121*, 254–255.
[43] Han, Y.; Lee, S. S.; Ying, J. Y. *Chem. Mater.* **2007**, *19*, 2292–2298.
[44] Schmidt-Winkel, P.; Lukens, W. W.; Yang, P.; Margolese, D. I.; Lettow, J. S.; Ying, J. Y.; Stucky, G. D. *Chem. Mater.* **2000**, *12*, 686–696.
[45] Ottaviani, M. F.; Moscatelli, A.; Desplantier-Giscard, D.; Renzo, F. D.; Kooyman, P. J.; Alonso, B.; Galarneau, A. *J. Phys. Chem. B* **2004**, *108*, 12123–12129.
[46] Ying, J. Y.; Mehnert, C. P.; Wong, M. S. *Angew. Chem., Int. Ed.* **1999**, *38*, 56–77.
[47] Patarin, J.; Lebeau, B.; Zana, R. *Curr. Opin. Colloid Interface Sci.* **2002**, *7*, 107–115.
[48] Zapilko, C.; Liang, Y.; Anwander, R. *Chem. Mater.* **2007**, *19*, 3171–3176.
[49] Gobin, O. C.; Wan, Y.; Zhao, D.; Kleitz, F.; Kaliaguine, S. *J. Phys. Chem. C* **2007**, *11*, 3053–3058.
[50] Kleitz, F.; T.-W. Kim, T.-W.; Ryoo, R. *Langmuir* **2006**, *22*, 440–445.
[51] Morineau, D.; Dosseh, G.; Alba-Simionesco, C.; Llewellyn, P. *Philos. Mag. B*

1999, *79*, 1847–1855.
[52] Kiyosawa, K. *J. Sol. Chem.* **2005**, *34*, 1–7.
[53] Xia, Y.; Dosseh, G.; Morineau, D.; Alba-Simionesco, C. *J. Phys. Chem. B* **2006**, *110*, 19735–19744.
[54] Alcoutlabi, M.; McKenna, G. B. *J. Phys.: Condens. Matter* **2005**, *17*, R461–R524.
[55] Alba-Simionesco, C.; Coasne, B.; Dosseh, G.; Dudziak, G.; Gubbins, K. E.; Radhakrishnan, R.; Sliwinska-Bartkowiak, M. *J. Phys.: Condens. Matter* **2006**, *18*, R15–R68.
[56] Anandan, S.; Okazaki, M. *Micropor. Mesopor. Mat.* **2005**, *87*, 77–92.
[57] Zhou, Y.; Stell, G. *Mol. Phys.* **1989**, *66*, 791–796.
[58] Macpherson, A. K.; Carignan, Y. P.; Vladimiroff, T. *J. Chem. Phys.* **1987**, *86*, 4228–4232.
[59] Evans, R. *J. Phys.: Condens. Matter* **1990**, *2*, 8989–9007.
[60] Rowlinson, J. S. *J. Chem. Soc. Faraday Trans. 2* **1986**, *82*, 1801–1815.
[61] Zhou, Y.; Stell, G. *Mol. Phys.* **1989**, *66*, 767–789.
[62] Macpherson, A. K.; Carignan, Y. P.; Vladimiroff, T. *J. Chem. Phys.* **1987**, *87*, 1768–1770.
[63] Sing, K. S. W.; Everett, D. H.; Haul, R. A. W.; Moscou, L.; Pierotti, R. A.; Rouquerol, J.; Siemieniewska, T. *Pure Appl. Chem.* **1985**, *57*, 603–619.
[64] Condon, J. B. *Surface Area and Porosity Determinations by Physisorption: Measurements and Theory*; Elsevier B. V., 2006.
[65] Lowell, S.; Shields, J. E.; Thomas, M. A.; Thommes, M. *Characterization of Porous Solids and Powders: Surface Area, Pore Size and Density*; Kluwer Academic Publishers, 2004.
[66] Thommes, M.; Köhn, R.; Fröba, M. *Appl. Surf. Sci.* **2002**, *196*, 239–249.
[67] Brunauer, S.; Emmett, P. H.; Teller, E. *J. Am. Chem. Soc.* **1938**, *60*, 309–319.
[68] Barrett, E. P.; Joyner, L. G.; Halenda, P. P. *J. Am. Chem. Soc.* **1951**, *73*, 373–380.
[69] Broekhoff, J. C. P.; de Boer, J. H. *J. Catal.* **1967**, *9*, 8–14.
[70] Broekhoff, J. C. P.; de Boer, J. H. *J. Catal.* **1967**, *9*, 15–27.
[71] Lukens, W. W., Jr; Schmidt-Winkel, P.; Zhao, D.; Feng, J.; Stucky, G. D. *Langmuir* **1999**, *15*, 5403–5409.
[72] Höhne, G.; Hemminger, W.; Flammersheim, H.-J. *Differential Scanning Calorimetry. An Introduction for Practitioners*; Springer, 1996.
[73] Brown, M. E. *Introduction to Thermal Analysis: Techniques and Applications*; Kluwer Academic Publishers, Boston, 2001.
[74] Dann, S. E. *Reactions and Characterization of Solids*; Wiley-Interscience, 2002.

Chapter 2

Experimental Details

2.1 Commercial Solvents and Reagents Used

The reagents PEO-PPO-PEO triblock copolymers P123 ($EO_{20}PO_{70}EO_{20}$) and F127 ($EO_{98}PO_{67}EO_{98}$), 1,3,5-trimethylbenzene (TMB, Mesitylene), cetyltrimethylammonium bromide (CTAB), 1-butanol, tetraethyl orthosilicate (TEOS), naphthalene (scintillation grade, 99.8%), 2-methylnaphthalene (97%), and 2-methoxynaphthalene (99%) were purchased from Aldrich and used as received without any further purification. 2-chloronaphthalene (98.0%) was purchased and used as received from TCI America. Hydrochloric acid was purchased from ACP, and Aerosil®200 was purchased from Degussa. All solvents were purchased and used as received from Caledon and Commercial Alcohols Incorporated.

2.2 Synthesis of Cylindrical Mesopores

2.2.1 SBA-15

The syntheses of SBA-15 materials were carried out according to Zhao[1] and Lettow.[2] In a typical synthesis, 2.0 g (0.4 mmol) PEO-PPO-PEO triblock copolymer P123 was first dissolved in 75 mL of 1.6 M HCl. 4.25 g (21 mmol) of TEOS was added drop-wise as the silica source. This mixture was stirred for 24 h and maintained at 35-40 °C.

Following this, the reaction mixture was transferred to a teflon-lined autoclave and aged for 24 h at 100 °C. After cooling to room temperature, the solids were collected by filtration on a Buchner funnel and dried in air for at least 24 h, and the resulting powder was calcined at 500 °C for 6 h to produce the mesoporous silica material. To expand the pore size, 0.23 mL TMB (TMB:P123 mass ratio 0.1) was added and stirred for 1 h prior to the addition of TEOS.

2.2.2 MCM-41

MCM-41 was prepared as described by Beck *et al.*,[3] except using half of the quantities. 20 mL H_2O and 6.7 mL of N-brand (sodium silicate, 28% silica) were combined with 0.6 g H_2SO_4 at room temperature and stirred for 10 min. Meanwhile, the template solution was prepared by stirring 8.4 g CTAB into 25.1 mL H_2O. This was then added to the silicate solution and stirred for 30 min. 10 mL of H_2O was added to the solution before transferring to a teflon-lined autoclave and aged at 100 °C for 144 h. After cooling to room temperature, the solids were recovered by vacuum filtration, washed with water, and dried in air at room temperature. This was then calcined for 6 h at 540 °C.

2.3 Synthesis of Spherical Mesopores

2.3.1 Mesocellular Foams

The syntheses of mesocellular foams (MCF) were carried out as prescribed by Zhao[1] and Lettow.[2] In a typical synthesis, 2.0 g (0.4 mmol) PEO-PPO-PEO triblock copolymer P123 was first dissolved in 75 mL of 1.6 M HCl. 1.38 mL TMB (TMB:P123 mass ratio 0.6) was added and stirred for 1 h, and then 4.25 g (21 mmol) of TEOS was added drop-wise as the silica source. This mixture was stirred for 24 h and maintained

at 35-40 °C. Following this, the reaction mixture was transferred to a teflon-lined autoclave and aged for 24 h at 100 °C. The solids were collected by filtration and dried in air for at least 24 h, and the resulting powder was calcined at 500 °C for 6 h to produce the mesoporous silica material.

2.3.2 Micelle-Templated Silicas

Micelle-templated silicas (MTS) were synthesized according to Ottaviani *et al.*[4] The following components were added under stirring in the following sequence: distilled H_2O, molar ratio 20; CTAB, molar ratio 0.1; NaOH, molar ratio 0.25; TMB, molar ratio 1.3, 2.0, or 5.0; SiO_2, molar ratio 1.

Following each addition, the mixture was allowed to equilibrate by stirring for 1 min. The final mixture was stirred for 30 min at room temperature and transferred to an autoclave to heat for 5 h at 70 °C. The materials were then filtered, washed with distilled water, and dried at 115 °C. Lastly, the MTS were calcined for 8 h at 550 °C to eliminate organic matter.

2.3.3 SBA-16

SBA-16 materials were prepared according to Kleitz.[5] The molar composition of the reaction mixture was varied in the range of 0.0035 F127/ xTEOS/ yBuOH/ 0.91 HCl/ 117 H_2O, with $x \simeq 0.5$-3 and $y \simeq 0$-3.

In a typical synthesis, 5.0 g (0.4 mmol) PEO-PPO-PEO triblock copolymer F127 was dissolved in 240 g distilled water and 10.5 g hydrochloric acid (35 wt %). After complete dissolution, 17.0 g of butanol was added at once at 45 °C and stirred for 1 h. 20.9 g of TEOS was then added. This synthesis was carried out in a closed flask and then transferred to a polypropylene bottle, where the mixture was aged at 100 °C for 24 h under static conditions. The white precipitate was filtered hot and

dried at 100 °C for 24 h. To remove the organic template, the materials were briefly washed with EtOH/HCl and calcined at 550 °C for 6 h.

2.4 Characterization of Mesopores

The template-free mesoporous silica materials were characterized by nitrogen adsorption analysis using the Micromeritics ASAP2020 analyzer at 77 K. Before acquiring the adsorption-desorption isotherms, the samples were degassed at 200 °C for 8 h. The Micromeritics software uses the Brumauer-Emmett-Teller (BET) method to calculate specific surface areas, and the Barrett-Joyner-Halanda (BJH) method to calculate pore volumes. However, these methods were found to underestimate both values; instead the Broekhoff-de Boer-Frenkel-Halsey-Hill (BdB-FHH) method was used to calculate the pore size distributions and pore volumes.[6] For spherical pores, the adsorption and desorption branches of the isotherms were used to derive the pore and window diameters, respectively.

Transmission Electron Microscopy (TEM) micrographs of the spherical mesopores were recorded using a Philips CM10 Transmission Electron Microscope (LaB_6 filament, 100 kV, 0.2 nm resolution); several were acquired by Dr. Harald Rösner at the Institut für Nanotechnologie in Germany on a FEI Tecnai F20 ST microscope.

2.5 Method of Loading Aromatics into Mesopores

In a typical loading, a carefully weighed sample of the silica material was degassed in a glass tube, either on the Micromeritics ASAP2020 using the degas method or on a vacuum line at 400 °C for 2 h. The sample was re-weighed after degassing and the total pore volume was obtained to calculate the correct mass of organic required. Samples for DSC experiments were prepared directly in the Al crucibles and the pores

were typically overloaded by 60%. For Raman spectroscopic studies, organics were added to samples inside glass tubes which were then quickly sealed by flame. In all cases, the loaded samples were allowed to equilibrate just below the boiling point of the organic for several hours and then cooled slowly to room temperature.

2.6 Measurements of Confined Organics

2.6.1 Differential Scanning Calorimetry Measurements

DSC measurements were performed using either a Mettler Toledo DSC822^e and STAR^e software, or a TA Instruments DSC Q20 equipped with the Liquid Nitrogen Cooling Accessory and Universal Analysis 2000 software. All samples were overloaded in order to detect both the bulk and confined transition temperatures and thus obtain precise determinations of temperature depression. All scans were carried out at heating rates of 10 °C/min after a 10 min isothermal stage at starting temperature. It was found that changing the rate from 5 to 10 to 20 °C/min did not affect the position or breadth of peaks in the thermogram. Calibration was performed using indium metal.

2.6.2 Raman Spectroscopic Measurements

Raman spectra were recorded on a Bruker RFS 100/S FT-Raman Spectrometer equipped with Nd^{3+}/YAG laser operating at 1064.1 nm and a liquid nitrogen-cooled Ge detector. The laser power was 120 mW at the sample, and the resolution was 2 cm^{-1}. Low-temperature measurements were carried out using a Bruker Eurotherm 800 series temperature control unit, which is capable of temperature regulation within $\pm$ 1 K.

2.6.3 Powder X-Ray Diffraction Measurements

Powder XRD patterns were recorded on a Rigaku diffractometer using Co Kα radiation (λ = 1.7902 Å). Samples were scanned from $5° \leq 2\theta \leq 65°$ at a scan rate of 10°/min with a step-size of 0.02°.

References

[1] Zhao, D.; Feng, J.; Huo, Q.; Melosh, N.; Fredrickson, G. H.; Chmelka, B. F.; Stucky, G. D. *Science* **1998**, *279*, 548–552.

[2] Lettow, J. S.; Han, Y. J.; Schmidt-Winkel, P.; Yang, P.; Zhao, D.; Stucky, G. D.; Ying, J. Y. *Langmuir* **2000**, *16*, 8291–8295.

[3] Beck, J. S.; Vartuli, J. C.; Roth, W. J.; Leonowicz, M. E.; Kresge, C. T.; D.Schmitt, K.; Chu, C. T.-W.; Olson, D. H.; Sheppard, E. W.; McCullen, S. B.; Higgins, J. B.; Schlenker, J. L. *J. Am. Chem. Soc.* **1992**, *114*, 10834 – 10843.

[4] Ottaviani, M. F.; Moscatelli, A.; Desplantier-Giscard, D.; Renzo, F. D.; Kooyman, P. J.; Alonso, B.; Galarneau, A. *J. Phys. Chem. B* **2004**, *108*, 12123–12129.

[5] Kleitz, F.; T.-W. Kim, T.-W.; Ryoo, R. *Langmuir* **2006**, *22*, 440–445.

[6] Lukens, W. W., Jr; Schmidt-Winkel, P.; Zhao, D.; Feng, J.; Stucky, G. D. *Langmuir* **1999**, *15*, 5403–5409.

Chapter 3

Characterization of Mesoporous Silica Hosts

3.1 Introduction

For our studies we chose to work with a range of pore sizes of cylindrical geometry, namely SBA-15 and MCM-41, as well as a range of spherical pores, namely MCF, MTS, and SBA-16 materials. The main focus of our current work is with regards to the cylindrical pore system. However, we would like to make a comparison between the two geometries and, as such, verification of the geometry of each host material is crucial. While there are several techniques which can be used to characterize porous materials such as transmission electron microscopy (TEM), small angle X-ray diffraction, and nitrogen adsorption porosimetry, we chose to employ mainly porosimetry due to limited or lack of availability of the other methods. TEM imaging is used as a secondary characterization technique to support our results from porosimetry.

With regards to nitrogen adsorption porosimetry there exist a number of calculation methods which can be applied to isotherm data in order to extract information. The simplest method for determining the diameter of a mesopore is the $4V/A$ method (where V is the volume and A the surface area of the pore), which can accurately measure well-defined cylindrical pores such as MCM-41.[1] In the presence of small pores,

especially micropores, however, its accuracy is limited in that A is determined by the BET method. There will be a large increase in the surface area with only a small increase in pore volume, resulting in an underestimated diameter. Furthermore, textural mesoporosity due to large mesopores formed between particles will significantly increase the pore volume without greatly increasing the surface area, resulting in an increased apparent diameter of the primary mesopore.[1] The $4V/A$ method cannot therefore be applied to SBA-15 or MCF materials due to microporosity and textural porosity.

For pores which are not well-defined and non-cylindrical, the most well known alternative is the BJH method.[1] Unfortunately, pore sizes are underestimated as it neglects the effect of curvature of the pore walls on the thickness of the adsorbed gas layer. The more widely applicable BdB method is outlined by Broekhoff and de Boer.[2,3] While this method is more accurate than the BJH method, its application finds difficulty due to the rigorous calculations involved. A modified version of this method, described by Stucky *et al.*,[1] simplifies calculations such that the equations to be solved do not involve derivatives. From the adsorption branch of the isotherm, the pore size can be analytically determined using Equation (3.1) and the square root of Equation (3.2). From the desorption branch, the pore size can be solved numerically by solving Equations (3.1) and (3.3) simultaneously:[1]

$$\ln \frac{p_0}{p} - \frac{\alpha}{t^3} = \frac{f\gamma V_m}{RT(r-t)} \tag{3.1}$$

$$\frac{3\alpha}{t^4} = \frac{f\gamma V_m}{RT(r-t)^2} \tag{3.2}$$

$$\ln \frac{p_0}{p} - \frac{\alpha}{rt^2} = \frac{2f\gamma V_m}{RT(r-t)} \tag{3.3}$$

where p/p_0 is the relative pressure, f is a factor determined by the Laplace curvature of the meniscus ($f = 1$ and 2 for a cylindrical and hemispherical meniscus, respectively), γ and V_m the surface tension and molar volume, respectively, of the adsorbed gas, r the pore diameter and t the statistical thickness of the adsorbed gas layer described by some adsorption isotherm. α is an empirical constant from Hill's approximation determined by the adsorbent (pore surface) and the adsorbate (adsorbed gas). Its value is $-5(3.54)^3$; this is the usual value used for determining the statistical thickness of the adsorbed nitrogen layer (3.54 Åis the thickness of a monolayer of N_2 at 77K, and 5 is determined empirically).[4,5] R and T have their usual meanings.

Besides its superior accuracy and ease of application, another useful feature of the BdB-FHH method is the ability to differentiate between different mesopore structures. For these reasons, we have chosen to use this method for the treatment of our isotherm data in order to characterize our porous host materials.

3.2 Application of the BdB-FHH Model

As described above, the procedure for SBA-15 synthesis at high TMB/P123 mass ratios actually renders MCF. To be able to discriminate between them, we prepared and characterized several samples using various TMB/P123 ratios. The graph in Figure 3.1 shows the change in our pore diameters with increasing ratio. Below a ratio of 0.2 SBA-15 is formed. Between 0.2 and 0.3 the material is in the transition region, where it is neither SBA-15 nor MCF; above this ratio MCF is produced. The TEM images we acquired depict the contrasting pore morphologies at 0.0, 0.3, and 0.8 TMB/P123 mass ratios. The images of the materials prepared at 0.0 and 0.8 mass ratios (Figures 3.1 (a) and (c)) were kindly acquired by Dr. Harald Rösner at the Institut für Nanotechnologie in Germany. The materials corresponding to the

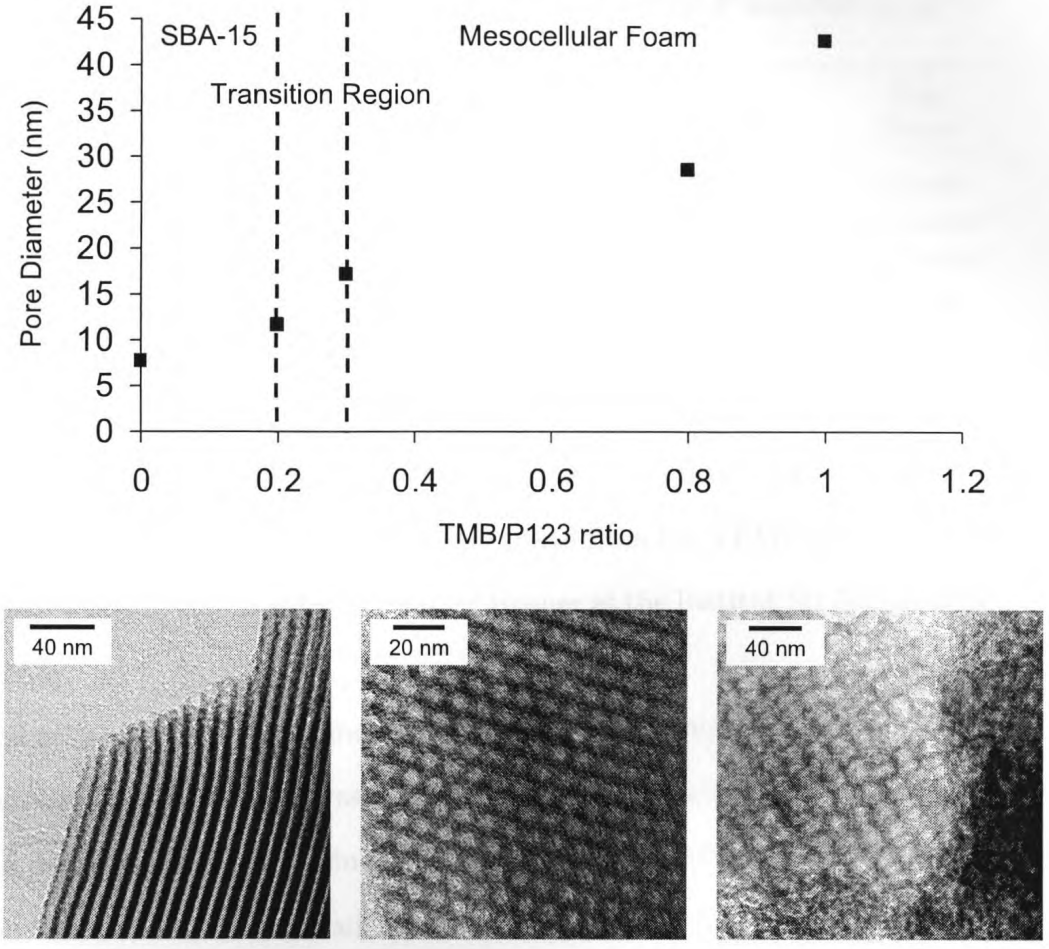

Figure 3.1. Change in pore diameter with varying TMB/P123 mass ratios and the progression of the morphological transition from SBA-15 to MCF. The TEM micrographs show SBA-15 (a), "transition" material (b), and MCF (c) corresponding to ratios of 0.0, 0.3, and 0.8, respectively.

graph in Figure 3.1 were characterized by the BdB-FHH method, and a summary of their synthesis conditions and properties is given in Table 3.1.

For mesoporous materials that exhibit hysteresis in their sorption isotherms, the BdB-FHH cylindrical model will produce identical values for the pore diameter if the pores are cylindrical. In this way, such results indicate that the pore structure is almost certainly cylindrical.[1] As shown in Figure 3.2, the values of the pore diameter of our sample A1 determined from the adsorption and desorption branches using

Table 3.1. Summary and comparison of SBA-15 and MCF materials using the BdB-FHH method

Sample	TMB/P123 mass ratio	$D_{BdB-FHH}$ (ads) (nm)	$D_{BdB-FHH}$ (des) (nm)	Type	Pore Shape
A1	0	7.7	7.1	SBA-15	cylinder
D7	0.2	11.5	4.6, 5.8	transition	"ink-bottle"
F2	0.3	17.2	7.3, 8.6	transition	"ink-bottle"
S1	0.8	28.5	9.5	MCF	sphere
A4	1.0	42.8	9.6	MCF	sphere

the cylindrical model are in good agreement with each other. They are also in good agreement with the pore size of 7.5 nm determined from the TEM image in Figure 3.3. This image was also acquired by Dr. Harald Rösner at the Institut für Nanotechnologie in Germany.

Spherical pores are described as "ink bottles" in which the spherical "bottles" are interconnected by smaller "necks." If the pore sizes determined from the adsorption and desorption branches using the cylindrical model differ substantially, the pores must be "ink-bottles" and the adsorption branch needs to be re-evaluated according to the spherical model in order to determine the body diameter. Applying the model to the adsorption branch, the pore size of MCF S1 is shown in Figure 3.4 to have a value of 28.5 nm. The initial application of the cylindrical model gives a value of 9.5 nm for the diameter for the windows or "necks."

The transition-type materials listed in Table 3.1 follow neither BdB-FHH models. Applying the cylindrical model yields different pore diameter values; it is clear that these materials are not cylindrical. However, as is evident in Figure 3.5, the desorption branch of F2 shows two pore size distributions meaning that there are two significant window sizes present in addition to the 17.2 nm pore body found from spherical adsorption. As mentioned above, pore walls buckle at the same periodicity as the pore diameter during the transition from SBA-15 to MCF such that spheres

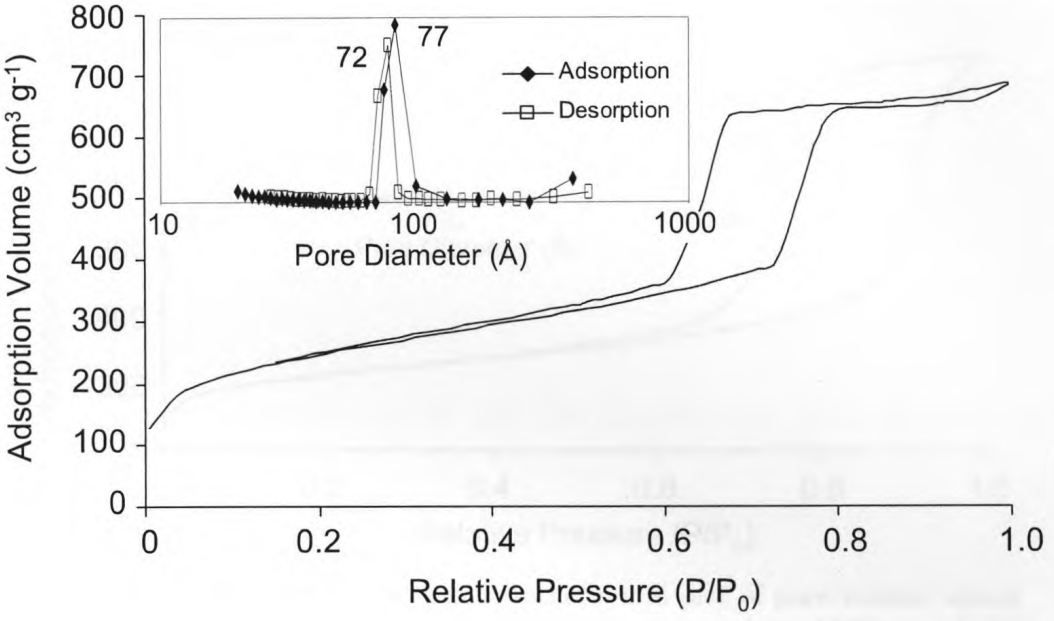

Figure 3.2. Nitrogen adsorption isotherm and plot of pore volume versus pore size determined by the BdB-FHH method (inset) for SBA-15 A1 with cylindrical pores 7.5 nm in diameter.

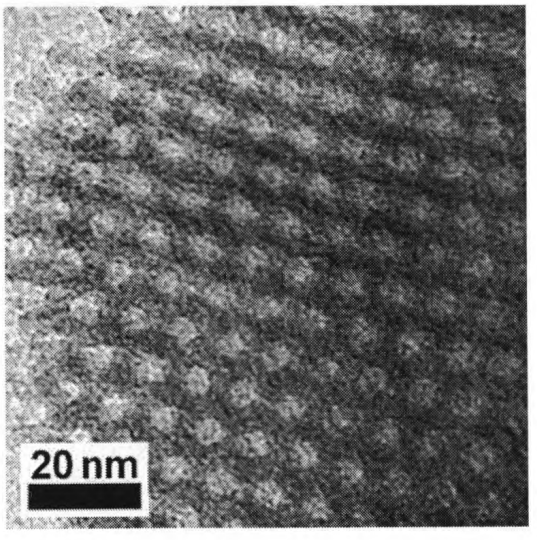

Figure 3.3. Transmission electron micrograph of SBA-15 sample A1 with cylindrical pores 7.5 nm in diameter.

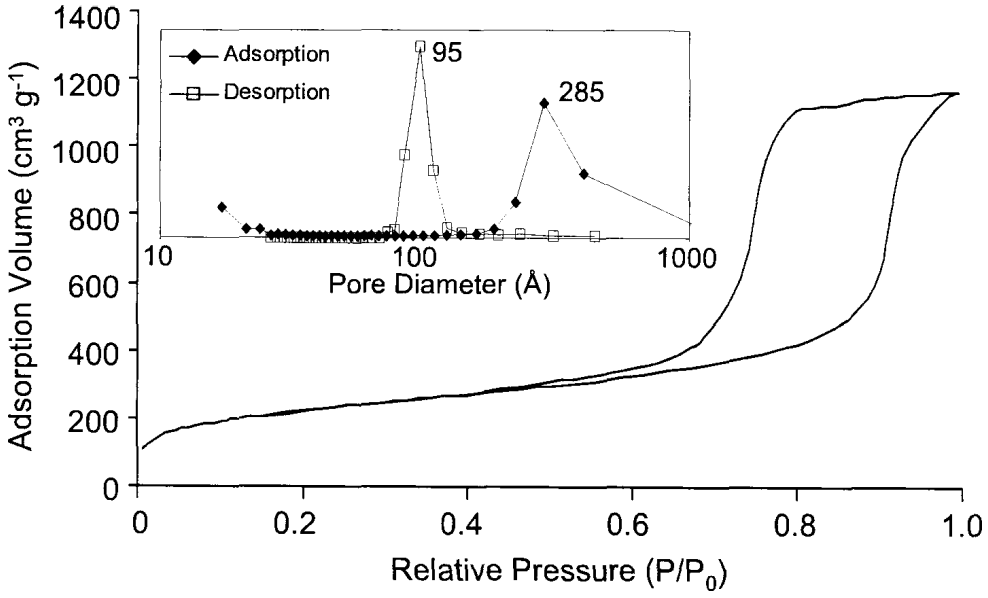

Figure 3.4. Nitrogen adsorption isotherm and plot of pore volume versus pore size determined by the BdB-FHH method (inset) for MCF sample S1 with spherical pores 28.5 nm and interconnecting windows 9.5 nm in diameter.

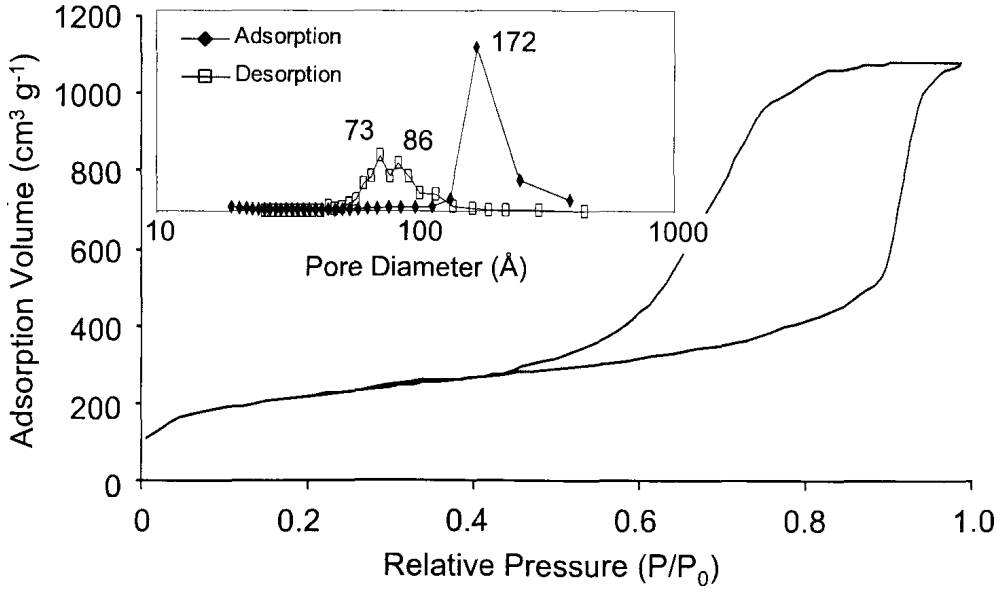

Figure 3.5. Nitrogen adsorption isotherm and plot of pore volume versus pore size determined by the BdB-FHH method (inset) for transition-type material F2 with "ink-bottle" pores 17.2 nm and interconnecting windows 7.3 and 8.6 nm in diameter.

are formed at the end of the transition. Although the transition materials are indeed "ink-bottle" shaped, the bodies are not yet spherical and we propose that the two size distributions from the desorption branch are a result of two different "neck" sizes. Though "ink-bottle" pores are not necessarily spherical, capillary condensation does occur via a hemispherical meniscus and so the spherical model is generally the most appropriate.[1]

3.3 Characterization of Cylindrical Mesopores

In order to obtain a broad range of cylindrical mesopore diameters for our study, SBA-15 and MCM-41 materials were synthesized. While SBA-15 provides the upper range of diameters, MCM-41 allows access to smaller pore sizes. Table 3.2 provides a summary of the properties of the cylindrical mesopores selected for our studies; adsorption values are taken as the true pore sizes. The nitrogen adsorption-desorption isotherms of these pores are shown in Figure 3.6. Samples C1 -3 are SBA-15 materials, characterized by the H2 hysteresis loops[6] seen in the diagram. The H1 hysteresis loop seen in the isotherm for C4 is typical of MCM-41 materials. When the BdB-FHH cylindrical model was applied to these samples, the adsorption and desorption branches for each yielded PSDs of comparable values (Figure 3.7), indicating that the pores were indeed of cylindrical geometry. Evaluation of these samples using the spherical model was therefore unnecessary.[1] A powder XRD pattern of sample C4 (MCM-41) was obtained and shown in Figure 3.8. The (100) reflection[7] is labeled and occurs at $2\theta = 3.44°$, giving a lattice spacing of $d = 29.8$ nm. The pore sizes of the other samples in both the spherical and cylindrical systems were too large to obtain powder patterns for on the present equipment.

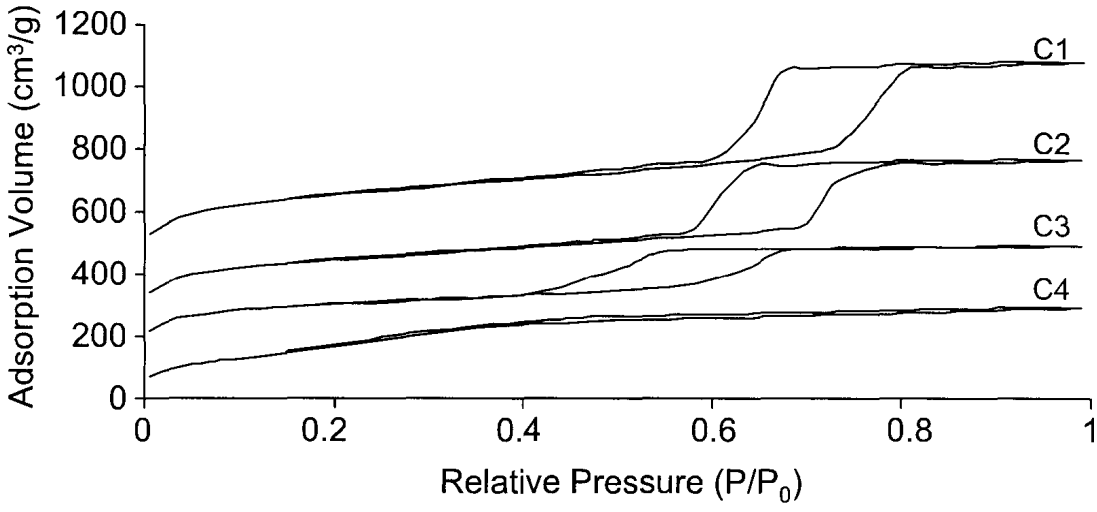

Figure 3.6. Nitrogen adsorption-desorption isotherms of cylindrical mesopores. C1, C2, and C3 are offset by 400, 210, and 100 cm^3g^{-1}, respectively.

Table 3.2. Summary of Cylindrical Mesopores

Sample	$D_{BdB-FHH}$ (ads) (nm)	$D_{BdB-FHH}$ (des) (nm)	Pore Volume (cm^3 g^{-1})	SSA (m^2 g^{-1})	Type
C1	8.0	7.3	1.03	674	SBA-15
C2	6.5	6.2	0.82	562	SBA-15
C3	5.5	4.8	0.51	419	SBA-15
C4	2.6	3.1	0.54	695	MCM-41

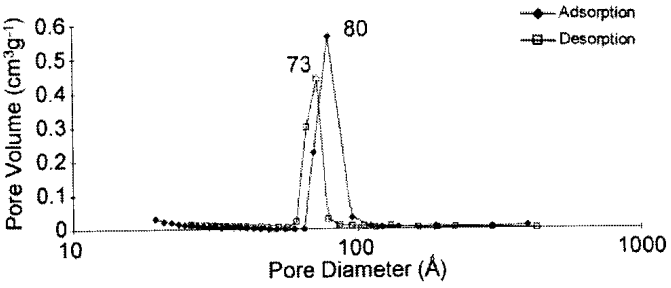

(a)

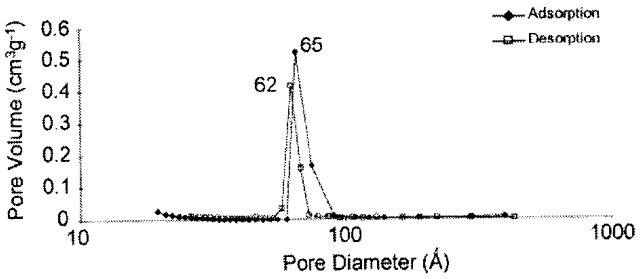

(b)

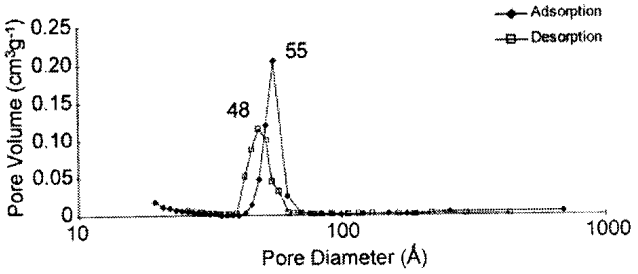

(c)

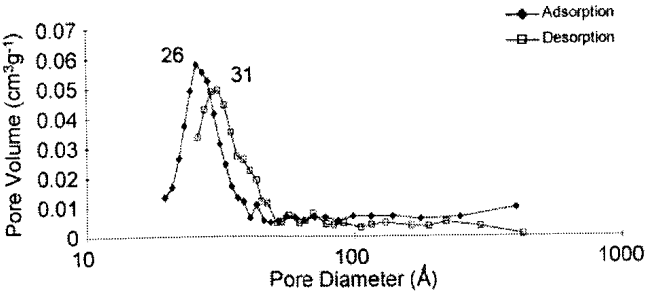

(d)

Figure 3.7. Pore size distributions of cylindrical pores C1 (a), C2 (b), C3 (c), and C4 (d) based on the adsorption and desorption branches of corresponding isotherms.

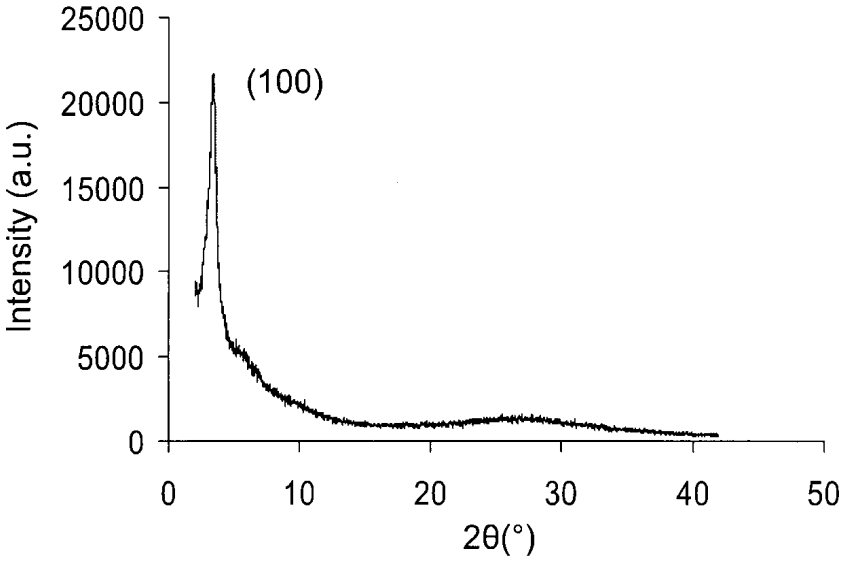

Figure 3.8. Powder XRD pattern of MCM-41 sample C4.

3.4 Characterization of Spherical Mesopores

In order to obtain a broad range of spherical mesopore diameters for our study, SBA-16 and MTS materials were synthesized in addition to the MCFs. While MCFs are $\geq$20 nm, SBA-16 and MTS form smaller pores. We were able to synthesize SBA-16 with pore diameters 4.3 to 9.0 nm, as well as MTS with diameters $\geq$ 10.9 nm.[8] Table 3.3 summarizes the properties of the spherical mesopores selected for our studies. The nitrogen adsorption-desorption isotherms and pore size distributions, calculated from the adsorption branches by the BdB-FHH method, are shown in Figures 3.9 and 3.10, respectively, indicating the range of pore sizes studied.

For each sample the isotherm desorption branch yielded a pore size different from that of the adsorption branch when the cylindrical model was applied, confirming that none of the materials are cylindrical-pored. Re-evaluation of the adsorption branches via the spherical model provided the correct pore diameters. From the

SBA-15 to MCF transition study above, we know that only non-spherical "ink-bottle" pores give rise to more than one pore size from the desorption branch (see Figure 3.5). The desorption branches of our set of spherical-pore samples indicate the presence of only one window diameter for each, confirming that the pores are indeed spherical. We could not obtain an accurate window diameter for the smallest pore, S4, due to meniscus instability; however the distribution plot does indicate only one peak, confirming spherical pore morphology. The PSD given by the desorption branch is not shown.

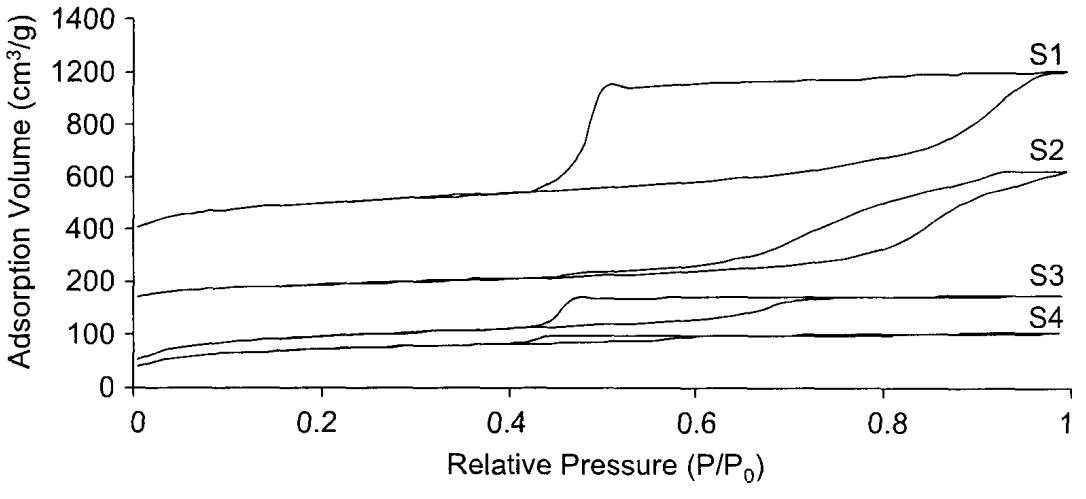

Figure 3.9. Nitrogen adsorption-desorption isotherms of spherical mesopores. S1 and S2 are offset by 500 and 300 cm^3g^{-1}, respectively.

Table 3.3. Summary of Spherical Mesopores

Sample	$D_{BdB-FHH}$ (ads) (nm)	$D_{BdB-FHH}$ (des) (nm)	Pore Volume ($cm^3\ g^{-1}$)	SSA ($m^2\ g^{-1}$)	Type
S1	28.5	9.5	1.14	813	MCF
S2	18.3	8.6	0.87	413	MTS
S3	9.0	4.6	0.58	780	SBA-16
S4	6.6	N/A	0.34	559	SBA-16

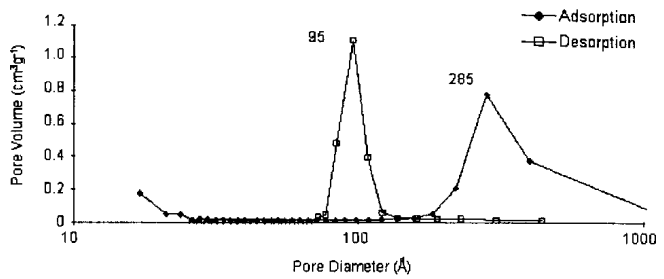

(a)

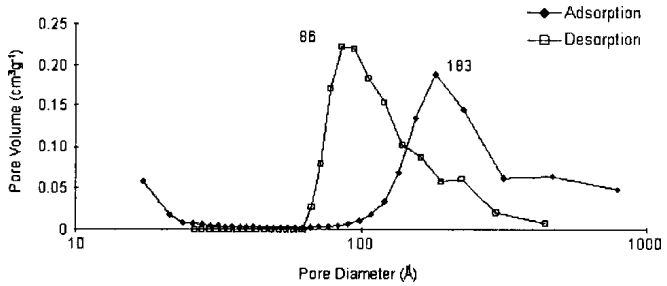

(b)

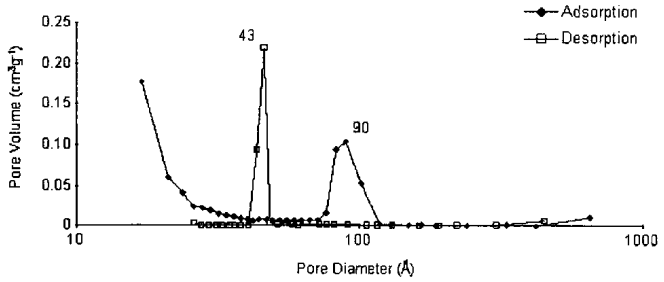

(c)

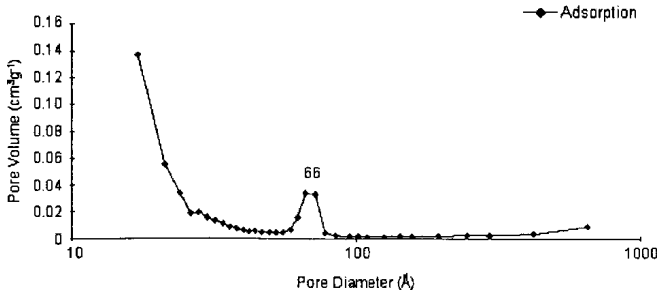

(d)

Figure 3.10. Pore size distributions of spherical pores S1 (a), S2 (b), and S3 (c) based on the adsorption and desorption branches of corresponding isotherms, and S4 (d) based on the adsorption branch of the isotherm.

3.5 Conclusions

Knowing that varying the TMB/P123 ratio of the same synthesis procedure would yield SBA-15, MCF, and "transition" type mesoporous materials, we were able to prepare a system for comparison of pore morphology. Using the Broekhoff-de-Boer Frankel-Halsey-Hill method, we can accurately differentiate between cylindrical and spherical geometries based on the pore size distributions calculated from adsorption and desorption isotherm branches. Our results are comparable to work done by Lukens *et al.*[1] Using the PSDs we were also able to determine values for the pore diameters. TEM images provide further evidence of both pore morphology and dimension, and our findings agree with those by Lettow *et al.*[9]

After verifying the accuracy of the BdB-FHH method for determination of pore morphology and size, we were able to apply this to the different pore samples synthesized for our confinement studies. In order to access a range of diameters for both cylindrical and spherical pores, we synthesized numerous MCM-41, SBA-15, MCF, MTS, and SBA-16 mesoporous silicates. Although there exist less complicated methods for accurate pore size analysis of MCM-41, we chose to use the BdB-FHH method for all types of materials in order to determine pore sizes in both an accurate and consistent manner. From these samples we selected a series of cylindrical and spherical pores to study. The cylindrical system ranges in pore diameter from 2.6 to 8.0 nm, and the spherical system from 6.6 to 28.5 nm.

References

[1] Lukens, W. W., Jr; Schmidt-Winkel, P.; Zhao, D.; Feng, J.; Stucky, G. D. *Langmuir* **1999**, *15*, 5403–5409.

[2] Broekhoff, J. C. P.; de Boer, J. H. *J. Catal.* **1967**, *9*, 8–14.

[3] Broekhoff, J. C. P.; de Boer, J. H. *J. Catal.* **1967**, *9*, 15–27.

[4] Galarneau, A.; Desplantier, D.; Dutartre, R.; DiRenzo, F. *Microporous Mesoporous Mater.* **1999**, *27*, 297–308.

[5] Halsey, G. *J. Chem. Phys.* **1948**, *16*, 931–937.

[6] Lowell, S.; Shields, J. E.; Thomas, M. A.; Thommes, M. *Characterization of Porous Solids and Powders: Surface Area, Pore Size and Density*; Kluwer Academic Publishers, 2004.

[7] Beck, J. S.; Vartuli, J. C.; Roth, W. J.; Leonowicz, M. E.; Kresge, C. T.; D.Schmitt, K.; Chu, C. T.-W.; Olson, D. H.; Sheppard, E. W.; McCullen, S. B.; Higgins, J. B.; Schlenker, J. L. *J. Am. Chem. Soc.* **1992**, *114*, 10834 – 10843.

[8] Ottaviani, M. F.; Moscatelli, A.; Desplantier-Giscard, D.; Renzo, F. D.; Kooyman, P. J.; Alonso, B.; Galarneau, A. *J. Phys. Chem. B* **2004**, *108*, 12123–12129.

[9] Lettow, J. S.; Han, Y. J.; Schmidt-Winkel, P.; Yang, P.; Zhao, D.; Stucky, G. D.; Ying, J. Y. *Langmuir* **2000**, *16*, 8291–8295.

Chapter 4

Confinement Effects on the Phase Transitions of Naphthalene

4.1 Introduction

Polycyclic aromatic hydrocarbons (PAHs) are major recalcitrant hydrophobic compounds, usually produced by industrial activities, disposal of processing wastes, and incomplete combustion of organic materials.[1] The PAH family include phenanthrene and anthracene, as well as the chemically-related benzene and naphthalene molecules. They are often found in soils, coals, and tar deposits. As many PAHs are known or suspected to be carcinogenic, mutagenic, and teratogenic to humans,[2] the decontamination of PAH-polluted sites is of substantial importance. Due to the low aqueous solubility and strong sorption properties of PAHs, the extent and rate of their biodegradation are restricted by limited bioavailability, so that contaminated sites are not easily treated by biological means.[1]

Aromatic compounds in diesel are considered contaminants, and they significantly lower the cetane number of fuel as well as increase undesirable emissions.[3,4] As such, there has been considerable effort worldwide in the reduction of aromatics. However, hydrodearomatization and desulfurization of diesel are still challenging tasks because diesel contains bulky aromatic and sulfur-containing compounds.[5,6] Zeolite-Y

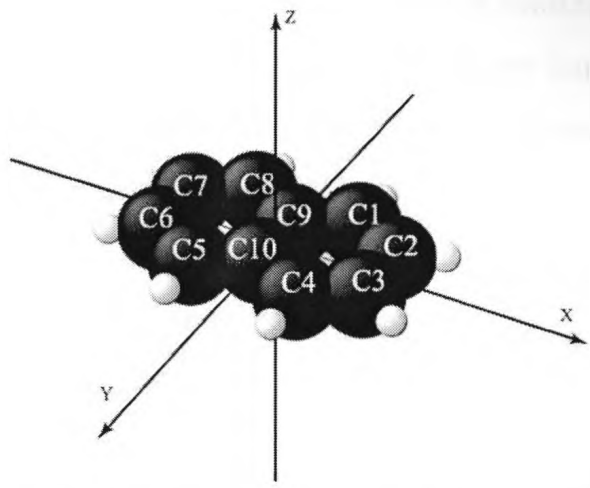

Figure 4.1. Molecular geometry of naphthalene.[9]

containing palladium/platinum catalysts in its micropores has often been used to reduce aromatics by hydrogenation. However, a simulation by Meng *et al.*[7] of the molecular dimensions of some typical aromatic molecules found in diesel, specifically pyrene and naphthalene, has shown that their minimum cross-sectional diameters are much larger than the 0.74 nm opening of the zeolite-Y supercage. They proposed that, in order to achieve efficient aromatics reduction, it is necessary to use pores with diameters larger than 1.5 nm to host both the molecules and the hydrogenation active site. Furthermore, there is a large diffusion barrier for large aromatics to access the metal catalysts in the zeolite-Y supercages, but this diffusion limitation vanishes largely when meso- or macropores are used.[8] To this effect, the understanding of the behaviour of aromatics such as pyrene and naphthalene within confined environments is critical to the advancement of such applications.

In this work, we are interested in studying the phase behaviour of naphthalene ($C_{10}H_8$) confined in mesoporous silicas. Due to its aromaticity, the so-called π-π stacking interactions are quite important to intermolecular interactions, leading to decreased solubility in common organic solvents compared to saturated systems.[10]

The topic of hydrophobic hydration has become one of considerable interest in the last half-century[11,12] because such hydrophobic effects are important in stabilizing biological structures, and they also determine the environmental fate of PAHs and other aromatic contaminants. Naphthalene is an important bicyclic aromatic species and its molar solubility in water at room temperature is approximately two orders of magnitude lower than that of benzene.[9] Due to aromaticity, a small partial negative charge is placed on the carbon atoms of benzene (periphery hydrogens carry partial positive charges), which favours a π-type hydrogen bond with water molecules. However, *ab initio* studies[13] have shown that the two carbons making up the fused-ring region of $C_{10}H_8$ (C_9 and C_{10} in standard nomenclature, see Figure 4.1) exhibit partial positive charges. The ability to form hydrogen bonds with water is therefore constrained due to a reduction in the negative charge density on its fused-ring structure.[9]

At room temperature, pure $C_{10}H_8$ exists in the solid phase. Crystalline naphthalene belongs to the monoclinic system and space group $P2_1/c$ with two molecules per unit cell,[14] as shown in Figure 4.2. It has a rigid lattice structure and shows no plastic crystalline phase.[15] The maximum span, along the diagonal, of the naphthalene molecule is ~6.9 Å; looking in the plane of the rings the height is estimated to be ~2.6 Å or less. The enthalpy of fusion of $C_{10}H_8$ is 148.31 J g^{-1}, and the melting and boiling points are 80.26 and 217.90 °C, respectively.[16]

Disorder induced by broad pore-size distributions of host mesoporous silicas renders the interpretation of results difficult. For this reason, we chose to work with host materials of well-defined geometries, specifically spherical and cylindrical pore shapes, which also exhibit narrow pore-size distributions. Furthermore, the synthesis of these materials can be reproducibly tailored to yield desired pore sizes. Synthesis conditions of the host materials as well as descriptions regarding the method of loading $C_{10}H_8$ into the pores for the following studies are described in Chapter 2.

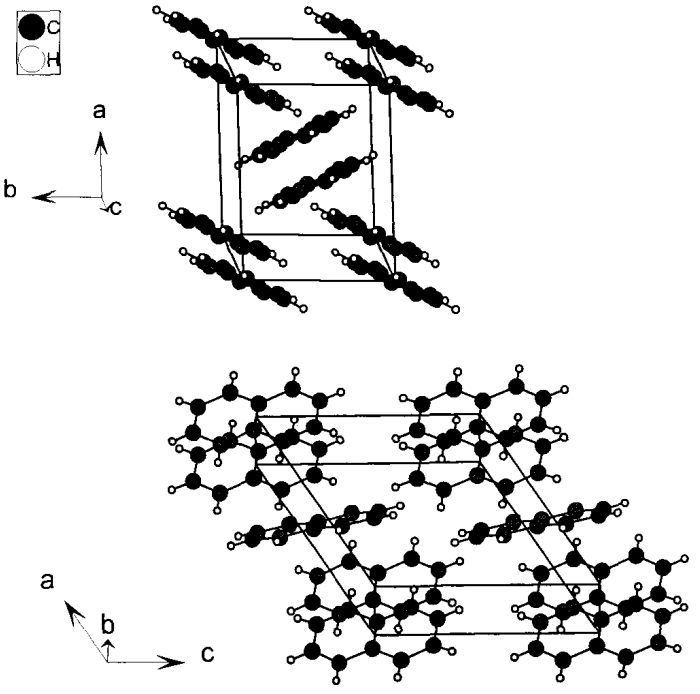

Figure 4.2. Two views depicting the monoclinic crystal structure of naphthalene.

4.2 DSC Studies in Spherical Pores

To ensure that we could accurately measure the transition temperatures and enthalpy of confined naphthalene, we first acquired the DSC thermogram of pure naphthalene. Figure 4.3 presents the thermogram for pure $C_{10}H_8$ upon heating and then cooling.

The onset temperature of melting was found to be 79.36 °C and in good accordance with the literature value.[16] Crystallization, however, occurred below this temperature at 66.05 °C. This expected thermal hysteresis is due to the small delay in the heterogeneous freezing nucleation of the pure liquid;[17] the melting temperature is then identified with the true transition temperature and taken as the reference transition temperature T_0. The measured enthalpy values ΔH_{sl} upon heating and cooling were found to be 147.18 J g^{-1} and 145.80 J g^{-1}, respectively, and in agreement with

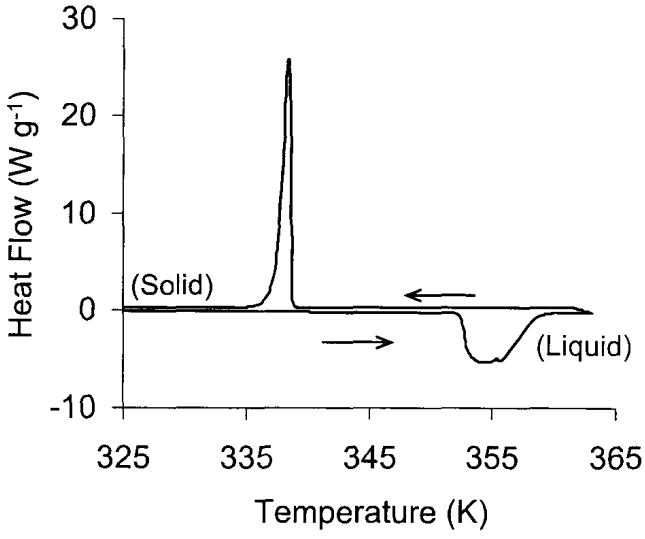

Figure 4.3. DSC curve of pure napthalene upon heating and cooling.

the literature value of 148.31 J g^{-1}.[16] Note that the complete freezing event usually takes place over a broader temperature range due to crystal rearrangement, so the tail end of the peak extends such that differentiation from the baseline is difficult.[18] It follows that the integrated peak area usually gives rise to a smaller enthalpic value than that given by the melting peak. The enthalpy calculated from the melting curve is therefore more accurate.

It is well known that materials confined in silica-based materials exhibit a transition temperature depression ΔT.[19] As previously stated, the general form of the Gibbs-Thomson equation is typically used to interpret these measurements:[17,20,21]

$$\frac{\Delta T}{T_0} = -2\frac{\gamma_{sl}}{r_p}\frac{\nu_s}{\Delta H_{sl}} \tag{4.1}$$

where T_0 is the bulk transition temperature, γ_{sl} the solid-liquid surface tension, ν_s the molar volume of the solid phase, r_p the pore radius, and ΔH_{sl} the latent heat of

Table 4.1. DSC values of the transition temperatures, transition temperature shifts (ΔT), and hysteresis values of $C_{10}H_8$ confined in spherical pores

Sample	r_p (nm)	t (nm)	T_0 (K)	T_m (K)	T_f (K)	ΔT_m (K)	ΔT_f (K)	Hysteresis
bulk	-	-	-	352.51	339.20	-	-	16.68
S1	14.3	2.4	352.55	338.94	334.92	13.61	17.63	4.02
S2	9.2	1.1†	351.41	331.93	316.02	19.48	35.39	15.91
S3	4.5	1.3	352.30	303.30	213.67	49.00	138.63	89.63
S4	3.3	0.9	351.77	286.66	200.57	65.11	151.20	86.09
S5	2.2	0.2	353.19	279.49	207.11	73.70	146.08	72.38

† Extrapolated from experimental data.

the solid-liquid transition. Note that Equation (4.1) is the same as Equation (1.9) in Chapter 1, and is shown here again for convenience.

The volume of each spherical mesoporous sample was calculated from nitrogen sorption data and the correct mass of $C_{10}H_8$ was introduced to achieve approximately a 60% overload. In this way we were able to obtain the DSC melting and freezing curves of both the bulk and confined organic for comparison as shown in Figure 4.4. The peaks corresponding to phase transitions of the confined $C_{10}H_8$ are denoted by arrows, and it can be seen that both melting and freezing transition temperatures decrease with pore diameter. A summary of these values can be found in Table 4.1. Also note that for the bulk transitions, the tangent to the peak represents the beginning of the transition process and determines the transition temperature; the FWHM (full width at half maximum) is small and due to kinetic effects only. In other words, the transition is first-order and does not occur instantaneously. In the confined phases there is a broadening of the transition peak which cannot be simply attributed to kinetics and so the transition temperature is taken at the maximum of the peak.[17,22]

It is evident from Figure 4.4 that there is a depression in both the confined melting and freezing transitions of $C_{10}H_8$ relative to those of the bulk transitions.

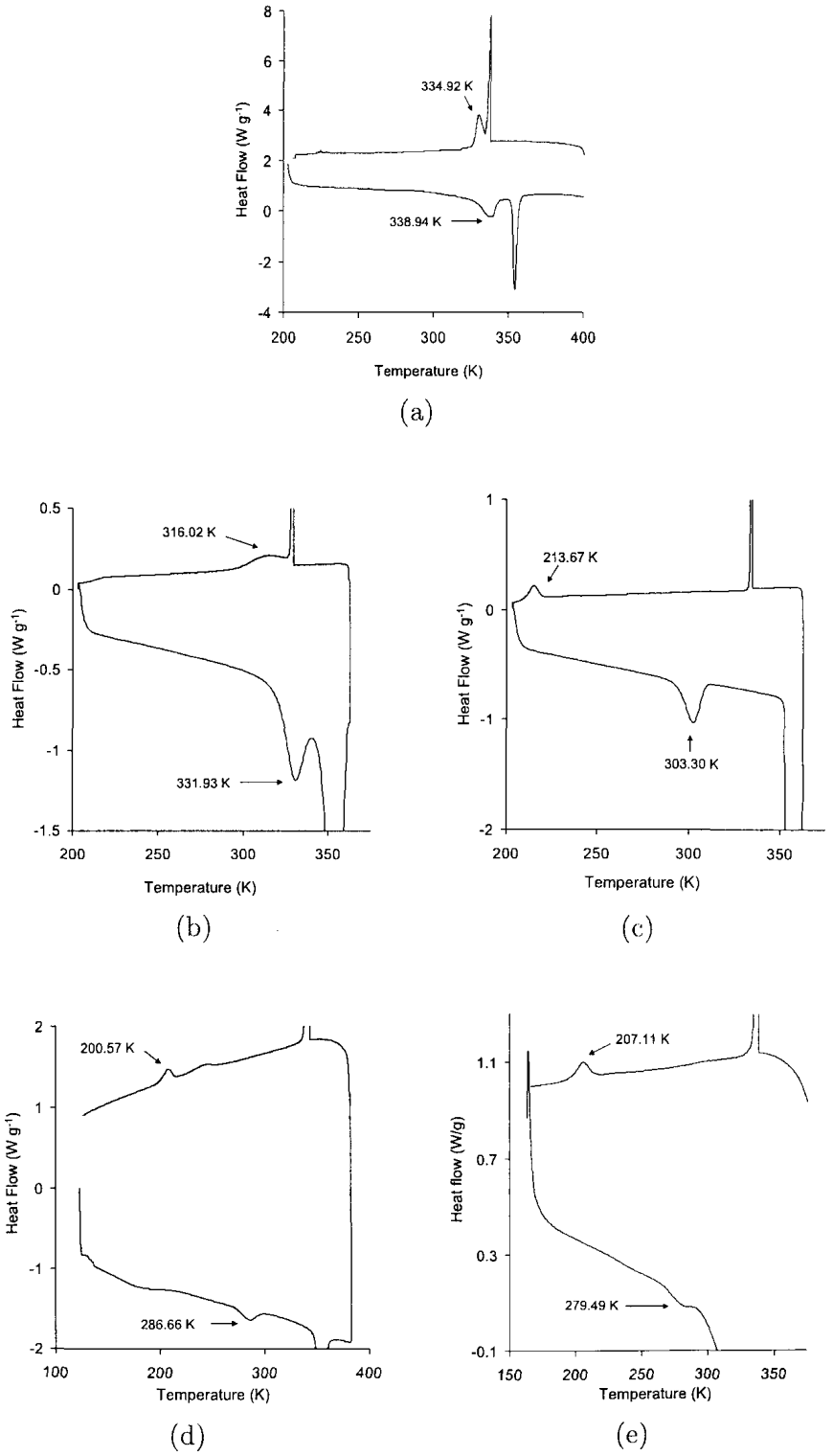

Figure 4.4. DSC thermograms of bulk $C_{10}H_8$ and $C_{10}H_8$ confined in spherical pores (a)S1, (b)S2, (c)S3, d)S4, and e)S5. Confined phase transitions are indicated by arrows and the transition temperatures are given.

Furthermore, this depression increases as the pore sizes become smaller. Evans *et al.*[23] used a simple pore model to explain the freezing temperature shift of confined liquids using Equation (4.2) where γ_{ws} and γ_{wl} are the wall-solid and wall-liquid surface tensions, ν_l is the molar volume of the liquid phase and ΔH_{sl} is the bulk latent heat of melting. For sufficiently large pores (> 6 nm diameter), the shift in freezing temperature ΔT_f can be related to the pore width D on the basis of the Gibbs-Thomson equation that is obtained by equating the free energies of the confined liquid and solid.

$$\Delta T_f = T_{f,pore} - T_{f,bulk} = -2\frac{(\gamma_{ws} - \gamma_{wl})\nu_l}{D\Delta H_{sl}} \tag{4.2}$$

The sign of the shift in freezing temperature is given by the difference of the surface tensions $\gamma_{ws} - \gamma_{wl}$; thus the equation predicts that the freezing temperature will, as in our case, decrease compared with the bulk value if the pore wall prefers the liquid phase to the solid phase. Conversely, if the solid phase is preferred then there will be an increase in the freezing temperature.[23] As we observe a decrease in the freezing temperature of confined $C_{10}H_8$ in the present work, this suggests that our silica-surface pore walls prefer the liquid phase of naphthalene over the solid. However, because Equation (4.2) uses derivations of macroscopic concepts such as surface tensions (which implies an interface separating two bulk-like phases) and does not account for the strong inhomogeneity of the confined phase, it fails for smaller pores.[24]

According to the Gibbs-Thomson equation the shift of the transition temperature of a confined liquid is inversely proportional to the pore radius. Among the assumptions made in the Gibbs-Thomson relationship are that the values of γ_{sl}, ΔH_{sl}, and ν_s are independent of crystal size. Furthermore, considerations that have not been incorporated into this equation are the confined fluid-fluid and fluid-wall

interactions,[25] but it has been found that the strength of the fluid-fluid interaction relative to the fluid-wall interaction plays an important role in determining the sign of the shift of the freezing point.[26] Nevertheless, many previous studies have largely confirmed the melting point depression expressed from the Gibbs-Thomson equation for nanoparticles as well as materials in confinement, where deviations are observed only for the smallest pore sizes.[27] Because it does reasonably describe many general systems, and because numerical values for the parameters involved are relatively simple to determine experimentally and from the literature, the Gibbs-Thomson equation is quite often used to describe the relationship between melting point depression and pore radius.[19,25,27]

In plotting ΔT_m as a function of r_p^{-1} as prescribed by the Gibbs-Thomson equation (Figure 4.5) our results do show a reasonably linear trend. However, this trend line does not pass through the origin (0,0). At $r^{-1} = 0$, $r = \infty$ and the pore size is infinitely large (*ie.* corresponds with unconfined bulk naphthalene), and it is expected that there is no transition temperature depression. It has been previously noted[28–31] that a so-called "contact layer" exists on the pore walls when a material is introduced to the pore interior. This layer remains in the liquid state below the melting temperature of the substance, and many authors have reported experimental evidence of such layer for numerous substances. For example, using ^{1}H NMR spectroscopy, Booth and Strange[31] examined the melting of cyclohexane in porous silica. They found that the confined melting temperature was below the bulk, and in the confined solid phase there were two distinct components of the transverse relaxation time. The long phase was attributed to the contact layer and their findings agree with the Raman studies by Shao *et al.*[32] A non-freezing layer has also been evidenced by ^{13}C nuclear spin-spin relaxation studies on confined benzene.[33] DSC and dielectric relaxation spectroscopy,[30] neutron scattering,[34] and and molecular simulations[35] have also been used to observe contact layer behaviour for a number of

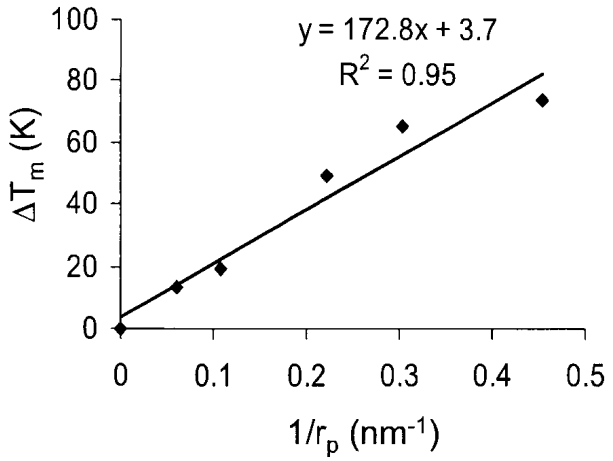

Figure 4.5. ΔT_m plotted as a function of r_p^{-1} for spherical pores.

substances such as water, benzene, nitrobenzene, and methane. The presence of such a non-freezing layer thereby reduces the effective pore radius in the application of the Gibbs-Thomson equation such that $r = r_p - t$, where r_p is the radius of the pore and t is the thickness of the contact layer. As a result, Equation (4.1) should be rewritten as:[36]

$$\frac{\Delta T}{T_0} = -2\frac{\gamma_{sl}}{(r_p - t)}\frac{\nu_s}{\Delta H_{sl}} \tag{4.3}$$

We have verified the existence of this non-freezing contact layer using Raman spectroscopic studies and DSC, discussed in Section 4.5. We therefore used this modified Gibbs-Thomson equation to treat our data as it allows for the evaluation of ΔT with respect to the effective pore radius r_p. The value of t can be determined by the traditional calibration procedure using materials of various pore sizes, where the transition temperature depression is related to the pore radius through a value of t. From experimental data, t can be determined by calculating the limit of the pore radius as ΔT_f approaches ∞ (no confined freezing).[37] However, there is an

underlying assumption that t does not vary with pore size.[36] Instead, we determined t according to a previously reported procedure[36,38] which does not assume that t is constant. For this procedure, sequentially various amounts of organic are added to or removed from the sample while DSC thermograms are obtained in between. In the method where the organic is progressively removed, the authors allow the inert gas to flush the DSC sample pan throughout the entire experiment. However, we have found that more accurate results can be obtained by flushing the pan for several minutes only in between DSC scans, as evaporation during scans decreases the mass of the sample. In our experience, this constant evaporation results in a skewed baseline. Briefly, a known mass of sample is placed in a DSC pan with an excess of $C_{10}H_8$. Several holes are drilled in the crucible lid and the $C_{10}H_8$ is progressively evaporated at 80°C by N_2 gas flushing between thermal cycles. We were able to calculate the amount of $C_{10}H_8$ remaining after each flush by weighing the pan; from there we were able to obtain semi-quantitative information about $C_{10}H_8$ (both free and confined) undergoing solid-liquid transition. Figure 4.6 presents some typical DSC curves recorded upon evaporating the $C_{10}H_8$ by flushing. The labels b and c denote the bulk and confined transition peaks, respectively. It can be seen that as flushing time increases, peak b decreases and eventually cannot be observed. Following this, peak c also decreases until no transition can be observed.

A plot of the heats corresponding to peaks b and c as a function of the quantity of naphthalene is shown in Figure 4.7. The point at which H_c differs from zero corresponds to the mass of the contact layer m_t. In the portion where H_c remains constant the pores are completely filled and we can measure $H_{c\ max}$. (From the graph, the mass required to fill the pores is 2.2 mg which agrees with the 2.4 mg calculated from N_2 sorption.) Here the enthalpy corresponds to the mass of the $C_{10}H_8$ present m_{vp} minus the mass participating in the contact layer, namely $m = m_{vp} - m_t$. We can then deduce the enthalpy of melting per gram for confined $C_{10}H_8$ ($\Delta H_c = 101$ J g^{-1}).

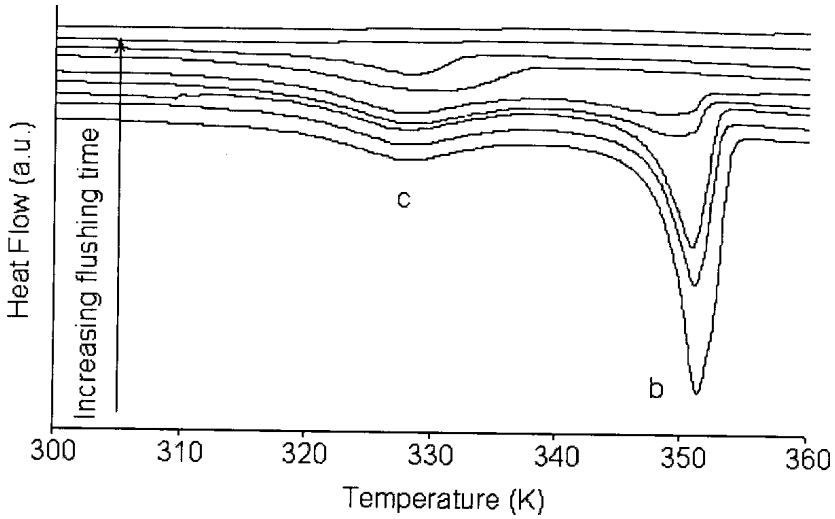

Figure 4.6. Thermograms recorded for various flushing times for sample S2 filled with $C_{10}H_8$.

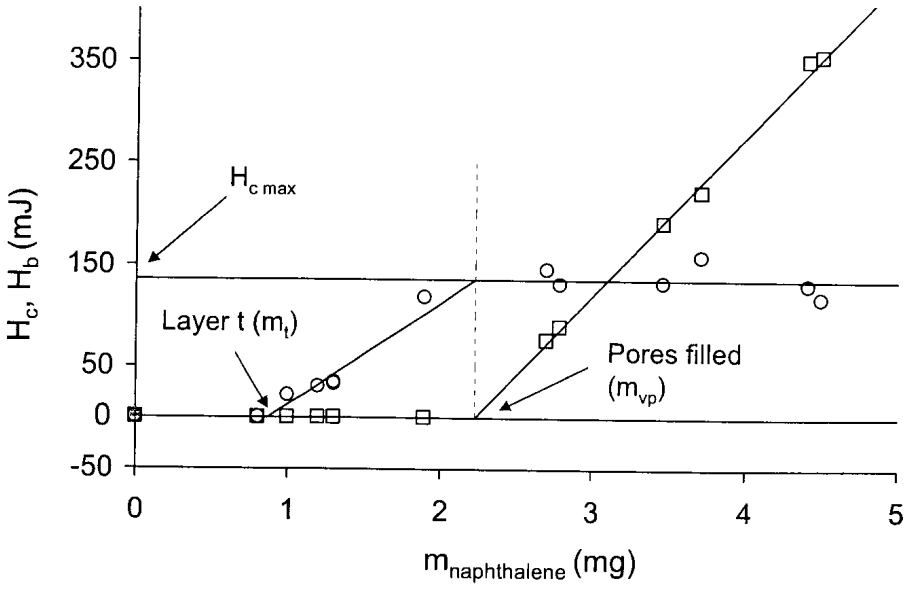

Figure 4.7. Evolution of H_c (○) and H_b (□) as a function of the mass of naphthalene present in sample S2.

Using the mass of the contact layer m_t determined from the plot, we were able to calculate the thickness of the layer according to:[36]

$$t = \frac{m_t}{\rho(SSA)(m_{SiO_2})} \tag{4.4}$$

where SSA is the specific surface area of the silica sample given in Table 3.3. Knowing the pore radius r_p and t for S2 we calculated the surface tension $\gamma_{sl} = 27.6$ mJ m^{-2} from Equation (4.3). There are a number of γ_{sl} values for naphthalene that can be found in the literature. Jackson and McKenna[39] found values of 8.2 and 6.1 mJ m^{-2} from experimental data, and they report a value of 31.7 mJ m^{-2} from empirical calculations based on previous work by Turnbull[40] and Dunning.[41] Jones[42] reported a value of 61±11 mJ m^{-2}. Our value is generally comparable to the empirical value within the large variability of such measurements reported in the literature. As such, we chose to use our γ_{sl} value for our calculations. Furthermore, use of the lower and higher reported values presents unreasonable results (*ie.* negative values of t). Jackson and McKenna[39] suggested one reason for such great variation in the reported values of γ_{sl} for $C_{10}H_8$ may be that there are changes in the crystallographic form when $C_{10}H_8$ crystallizes in confined geometry. However, we have found that this is not the case and our results are discussed in Section 4.6.

If the value of t is constant for varying pore sizes, then t will be 75% of the pore radius for the second-smallest pore S4, and twice as large as the radius of the smallest pore S5. This is clearly unreasonable, and we conclude that for our system, t does indeed vary with pore size. Putting our calculated value for γ_{sl} back into Equation (4.3) we determined the thickness t of the contact layer in each pore size. It was found that t generally decreases with pore size. This trend agrees with results reported by Meziane *et al.*[36] for carbon tetrachloride confined in mesoporous silica gels. Our results are presented in Table 4.1 and a plot of t as a function of r is shown

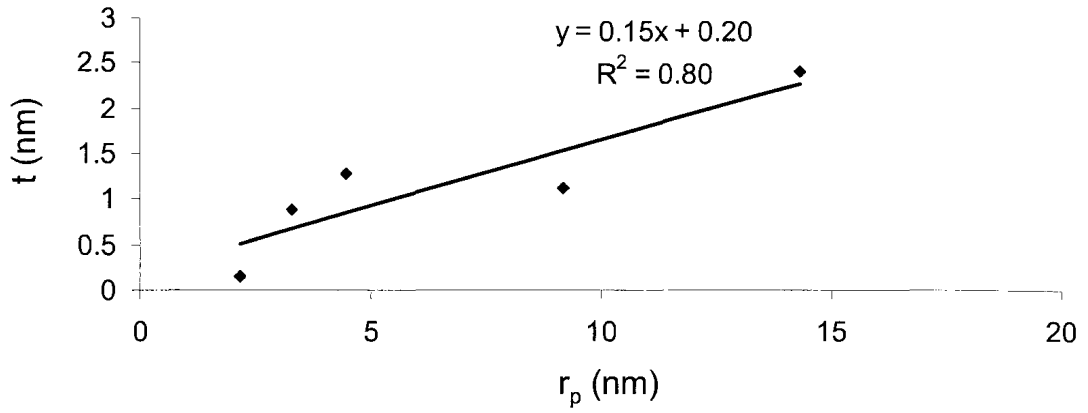

Figure 4.8. t plotted as a function of r_p for $C_{10}H_8$ in spherical pores.

in Figure 4.8.

From the evaporation experiment results we were also able to deduce the porous volume V_p according to:[36]

$$V_p = \frac{m_{vp}}{\rho m_{SiO_2}} \tag{4.5}$$

where ρ is the solid density of of naphthalene. We extrapolated the value 0.832 g mol^{-1} at 80°C from previous work by Gryzll *et al.*[43] The value found for V_p is comparable to that obtained by N_2 sorption (V_{N_2}). These results are summarized in Table 4.2 for comparison.

It is clear from the DSC thermograms in Figure 4.4 that the breadths of confined transitions broaden as pore size decreases, suggesting a progressive layer-by-layer melting in confinement where the outer portions of the confined material melt first and those in the centre melt last.[39,44] In the case of freezing, the liquid outside the pore freezes first and freezing inside the pores occurs through the slow penetration of a freezing front. This penetration is delayed in the smallest pore apertures, broadening

the confined transition peak.[17]

Table 4.2. Thickness t, porous volumes and transition enthalpies measured by DSC and N_2 sorption for sample S2

Sample	t (nm)	V_p ($cm^3\ g^{-1}$)	V_{N_2} ($cm^3\ g^{-1}$)	ΔH ($J\ g^{-1}$)
S2	1.1	0.85	0.87	101

4.3 DSC Studies in Cylindrical Pores

Using the same method of pore loading for spherical pores, we loaded our cylindrical pores with naphthalene such that the DSC thermograms provide information regarding the phase transitions of both the bulk and confined $C_{10}H_8$. Thermograms are shown in Figure 4.9. Results following the Gibbs-Thomson equation are shown in Figure 4.10, where ΔT_m is plotted against the inverse of the pore radius without taking into account the thickness t of the contact layer. Again, the trend is reasonably linear and in this case $\Delta T_m = 0$ when $r^{-1} = 0$. However, as we have determined that the contact layer does indeed exist in Section 4.5, the calculation of ΔH will be underestimated if this layer is not accounted for. We therefore performed the evaporation experiment in order to determine t. It should be noted that Meziane *et al.*[36] employed high volume DSC pans so that the quantities of solvent used in their studies were much greater than that used in ours. The most sophisticated balance we had access to was an analytical balance, accurate to a milligram, and we realize that the error in our masses could contribute quite significantly to our results. As such, we performed the experiment three times using three samples of C1 (8.0 nm diameter) and $C_{10}H_8$ to ensure that our method is reasonably accurate.

Some typical DSC thermograms recorded upon evaporation of $C_{10}H_8$ from Trial

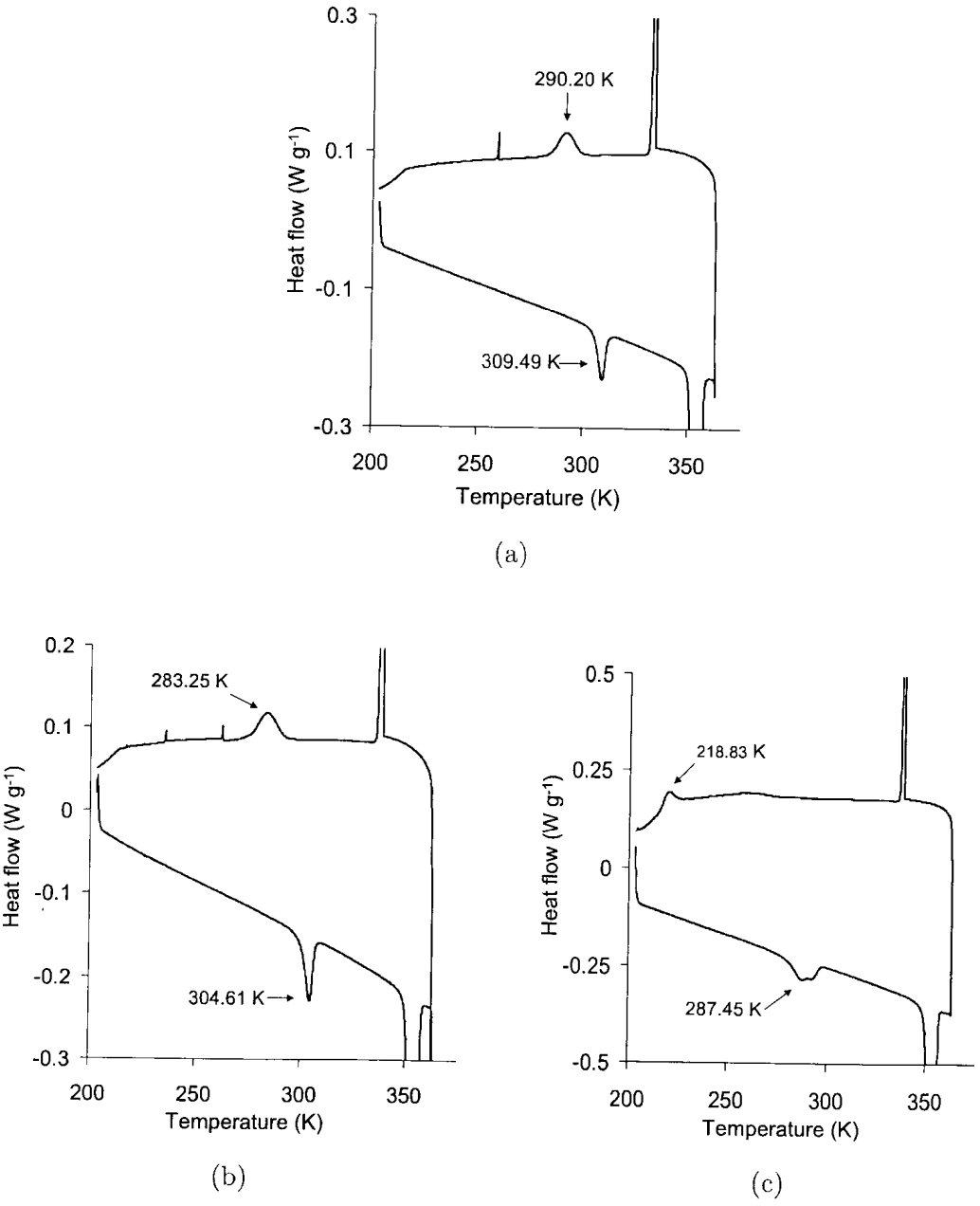

Figure 4.9. DSC thermograms of bulk $C_{10}H_8$ and $C_{10}H_8$ confined in cylindrical pores (a)C1, (b)C2, and (c)C3. Confined phase transitions are indicated by arrows and the transition temperatures are given.

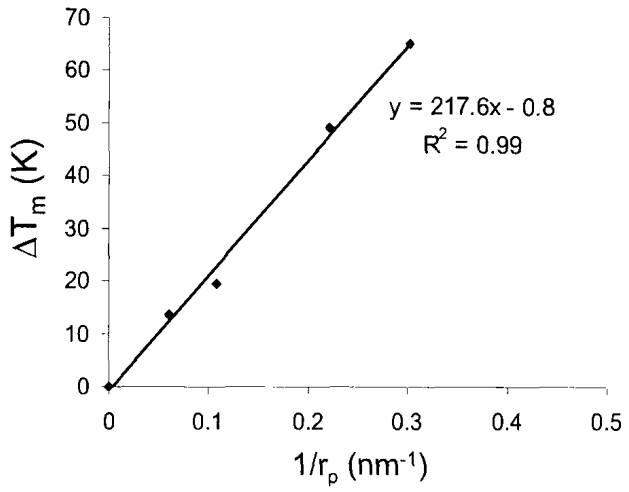

Figure 4.10. ΔT_m plotted as a function of r_p^{-1} for $C_{10}H_8$ in cylindrical pores.

1 are presented in Figure 4.12; labels b and c denote the bulk and confined transition peaks, respectively. For each of Trials 1 - 3, the plots of the heats corresponding to peaks b and c as functions of the quantity of naphthalene present are shown in Figure 4.11. Results from the three sets are reasonably consistent and the calculated volumes V_p correspond well with the pore volume V_{N_2} determined by nitrogen adsorption porosimetry. We therefore report the averages of each as the true values for pore C1; results are shown in Table 4.3 and these numbers are used in the calculations of t for the other pores in this system. Although our results are semi-quantitative, we are able to determine the trends of the systems under study.

Table 4.3. Mass and thickness t, porous volumes and transition enthalpies measured by DSC and N_2 sorption for sample C1 in three separate trials

Trial	mass (mg)	t (nm)	V_p ($cm^3\ g^{-1}$)	V_{N_2} ($cm^3\ g^{-1}$)	ΔH ($J\ g^{-1}$)
1	0.45	0.7	0.90	1.03	101
2	0.26	0.6	1.07	1.03	76
3	0.41	0.5	0.90	1.03	91
avg	-	0.6	0.96	1.03	89

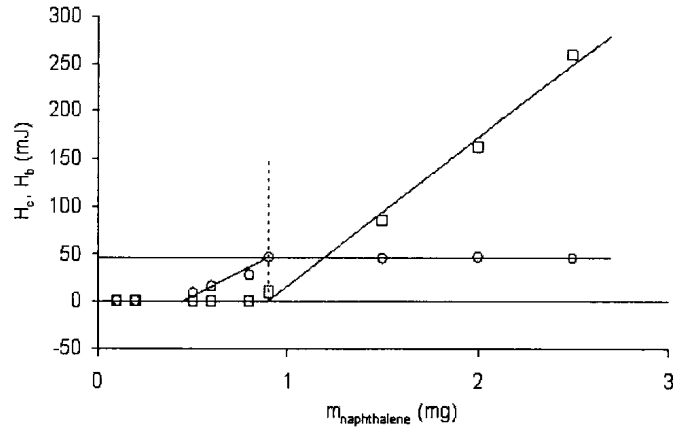

(a)

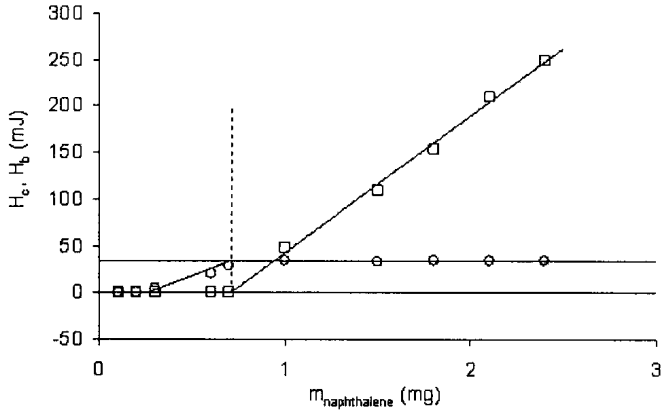

(b)

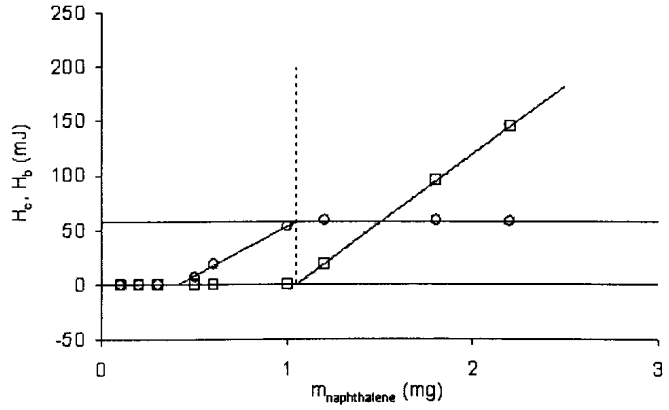

(c)

Figure 4.11. Evolution of H_c (○) and H_b (□) as a function of the mass of naphthalene present in sample C1 for (a) Trial 1, (b) Trial 2, and (c) Trial 3.

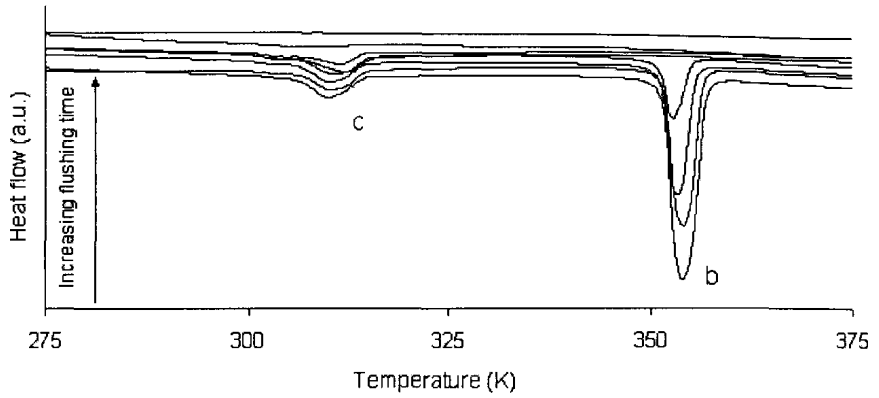

Figure 4.12. Thermograms recorded for various flushing times for sample C1 filled with $C_{10}H_8$.

As in the previous section, we calculated the value of the surface tension γ_{sl} using Equation (4.3). For $C_{10}H_8$ in cylindrical pores we find that it has a value of 19.0 mJ m^{-2}. We note a small discrepancy between the γ_{sl} values found for naphthalene in our spherical pores (27.6 mJ m^{-2}) and our cylindrical pores. Although both numbers are within the range of those values reported in the literature (see above), the value calculated from the cylindrical system is 70% lower than the value calculated from the spherical system. According to Jackson and McKenna[39] a possible reason for this is a reduced value of the solid density ρ, and thus increased value of the molar volume ν_s, resulting from poor packing in confinement which causes a lower value of γ_{sl}.

Nevertheless, we chose to use our calculated value of $\gamma_{sl} = 19.0$ mJ m^{-2} in the treatment of our cylindrical system as this value provides the most reasonable results for t. Putting this value back into Equation (4.3) we can calculate t for the other pores in this system. Again, we find that there is a decrease in t with decreasing pore size. The trend is shown in Figure 4.13.

Plotting ΔT_m as a function of $r_p - t$ as shown in Figure 4.14, we expected to see a confined melting transition in the smallest pore C4 (radius 1.3 nm) in the

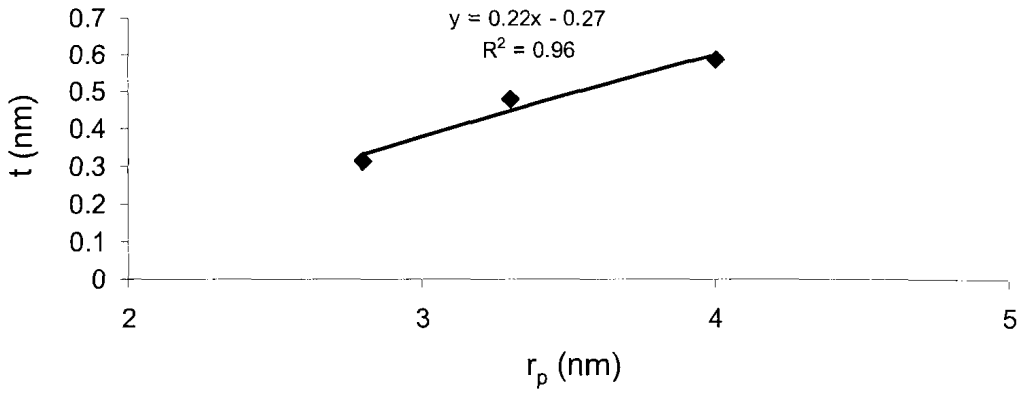

Figure 4.13. t plotted as a function of r_p for $C_{10}H_8$ in cylindrical pores.

vicinity of 230 K; however, the DSC thermogram showed only the bulk transition peak. Since 230 K is well above the lowest temperature we could attain on the instrument used, we ruled out the notion that the phase transition was perhaps too far depressed to be seen. It is known that as a particle becomes smaller, there is a larger percentage of its atoms residing at the surface where they have more freedom to move. At some point the particle will be practically all surface, decreasing the likelihood of a transition into the solid phase.[45] This argument is in agreement with experiments by Dosseh *et al.*[22] Their results showed that for simple molecules with van der Waals type interactions, such as benzene and carbon tetrachloride, the minimum pore size required for crystallization is roughly 10 molecular sizes. In a computational simulation by Song *et al.*, the critical diameter of $C_{10}H_8$ (*ie.* the minimum diameter it can pass through without distortion) was found to be 7.19 Å. Not accounting for the contact layer, the core of our pore C4 has a diameter of 2.6 nm, which is only equivalent to about 4 molecular diameters. We therefore propose that the core of the pore is not sufficiently large to host enough naphthalene molecules for crystallization to occur. On the other hand, crystallization did occur in our smallest spherical pore S5 which has a diameter of 4.4 nm, or approximately 6 molecular

diameters. However, crystallization in confinement also depends on other factors such as the stability of the crystal, pore topology, and pore geometry.[22] It therefore appears that for $C_{10}H_8$, the minimum pore diameter required for crystallization is somewhere between 4 and 6 molecular diameters. To support this claim, we found that the calculated enthalpy for the bulk transition peak in the DSC curve of $C_{10}H_8$ in pore C4 gave a much higher value than what the expected value should be. This confirms that there must be some mass existing inside the pores which does not undergo phase transition. The results for the other cylindrical pores are tabulated in Table 4.4.

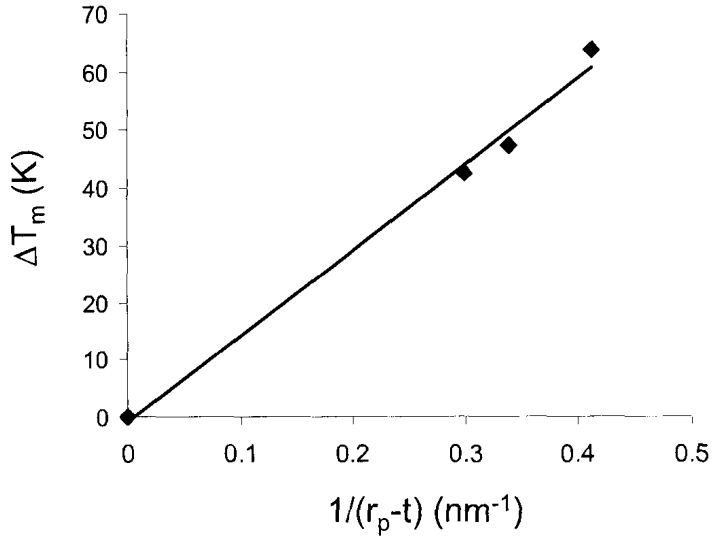

Figure 4.14. ΔT_m plotted as a function of $(r-t)$ for $C_{10}H_8$ in cylindrical pores.

4.4 Comparison of Cylindrical and Spherical Pores

The DSC thermograms indicate a thermal hysteresis of the confined $C_{10}H_8$ which increases with decreasing pore radius, summarized in Tables 4.1 and 4.4 for both spherical and cylindrical pores, respectively. As noted above, the hysteresis seen in

Table 4.4. DSC values of the transition temperatures, transition temperature shifts (ΔT), and hysteresis values of $C_{10}H_8$ confined in cylindrical pores

Sample	r_p (nm)	t (nm)	T_0 (K)	T_m (K)	T_f (K)	ΔT_m (K)	ΔT_f (K)	Hysteresis
bulk	∞	-	-	352.51	339.20	-	-	16.68
C1	4.0	0.59[†]	351.99	309.49	290.35	42.50	61.64	19.14
C2	3.3	0.48	352.01	304.61	283.25	47.40	68.76	21.36
C3	2.8	0.32	351.18	287.45	218.452	63.73	132.35	69.03

[†] Extrapolated from experimental data.

the bulk phase is typical and is due an uncontrollable delay in nucleation on cooling. Because the transition mechanisms of a confined liquid are different from those of the bulk, the physical cause of such feature differs. Materials confined in small pores exhibit transition temperature depressions due to their high acquired surface area to volume (S/V) ratios; the presence of this surface introduces excess energy for the solid phase and shifts the solid-liquid equilibrium toward the liquid state. Petrov and Furó[21] attribute this hysteresis to pore curvature-induced metastability of the solid phase which is, thereby, an intrinsic property of the system defined by the pore morphology and interfacial interactions.

Consider a situation illustrated in Figure 4.15 in which an arbitrary pore is filled by a liquid. The Helmholtz free energy F is dependent on the thickness of the liquid layer ℓ, which increases with melting and decreases with freezing, and the temperature T. At low temperatures $F(\ell, T)$ has two local minima where the minimum at $\ell = r$ corresponds to a pore filled by liquid, while the minimum at $\ell = t$ corresponds to a pore filled by solid except for the non-freezing film of width t. The energy barrier between the minima reflects the competition between volume and surface contributions to F. In increasing the temperature, the solid-liquid equilibrium point T_2 is reached where the two corresponding minima of F are equally deep. However, melting cannot occur at this temperature because growing the liquid phase from the nonfreezing film at the pore wall would advance the liquid-solid front along increasing ℓ. Because this

is a free-energy penalty, melting will not start until T_3, where thermal fluctuations are sufficient to overcome the energy barrier. This temperature is therefore associated with the melting point of the pore solid; ie $T_m = T_3$. Upon cooling from T_4 where the pore is filled with liquid, freezing will occur at the equilibrium point $T_f = T_2$ if there is excess solid which exists outside the pore, as in our case. The area between T_2 and T_3 is metastable, and it is this region which provides the hysteresis.[21]

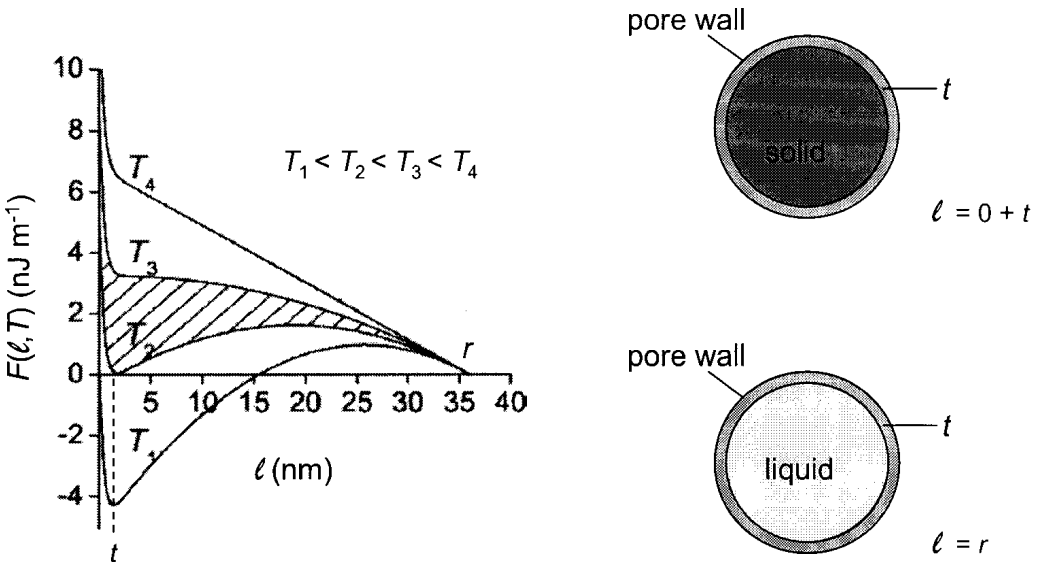

Figure 4.15. The Helmholtz free energy of an arbitrary solvent as a function of l and T. The metastable region providing the hysteresis is hatched. Figure modified from Petrov *et al.*[21] A schematic of an arbitrary pore is shown on the right. The case where $l = 0 + t$ corresponds with a pore full of solid except for the contact layer denoted by t, and the case where $l = r$ corresponds with a pore full of liquid.

If T_f and T_m are defined as above, they can be expressed using conditions for the extrema and inflection point of $F(\ell, T)$, respectively: $F = 0$ and $(\partial F/\partial \ell) = 0$ at $T = T_f$, and $(\partial F/\partial \ell) = 0$ and $(\partial^2 F/\partial \ell^2) = 0$ at $T = T_m$. Solving the functions for ΔT_f and ΔT_m allows for the relation of ΔT_m and ΔT_f:[21]

$$\Delta T_m = \Delta T_f \frac{2\kappa V}{S} \tag{4.6}$$

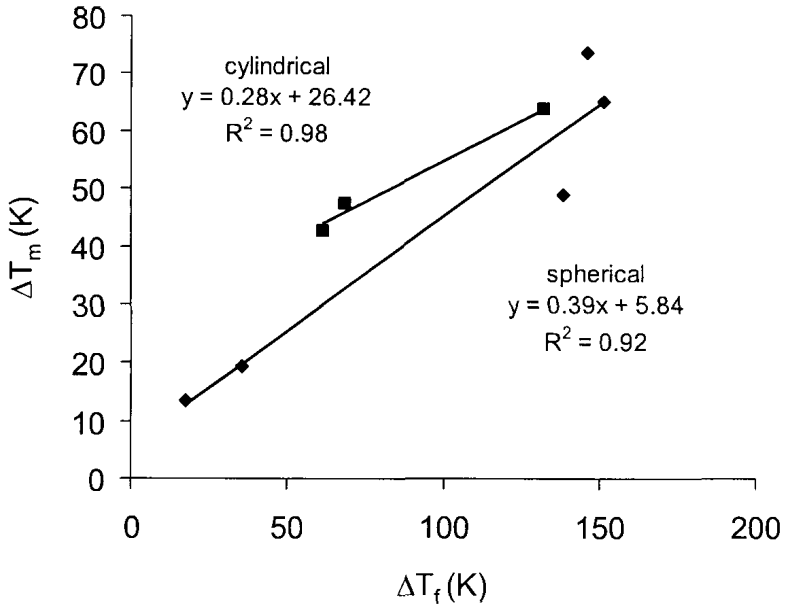

Figure 4.16. ΔT_m versus ΔT_f for naphthalene confined in spherical and cylindrical pores.

where κ is the integral mean curvature of the pore surface.

It turns out that for any pore $2\kappa < (S/V)$ ($2\kappa V/S = 2/3$ for a spherical pore and $2\kappa V/S = 1/2$ for a cylindrical pore), freeze-melt hysteresis always occurs with $\Delta T_m < \Delta T_f$.

Using values given in this model for ideal pores, we can calculate that $\Delta T_m = \frac{2}{3}\Delta T_f$ for a spherical pore and $\Delta T_m = \frac{1}{2}\Delta T_f$ for a cylindrical one. This implies that in plotting ΔT_m as a function of ΔT_f for both geometries, we should find that the slope of the linear relationship for the spherical system should be 1.3 times greater than that of the cylindrical systems; the calculations leading up to this point rely on the assumptions that the solid-liquid interface inside the pore is equidistant to the pore wall and that the pore sizes are much greater than t. Plotting our results in Figure 4.16 we find that the slope of this relationship for our spherical pores is 1.4 times greater than of our cylindrical ones. Nonetheless, the trend from our data is consistent with that of the model.

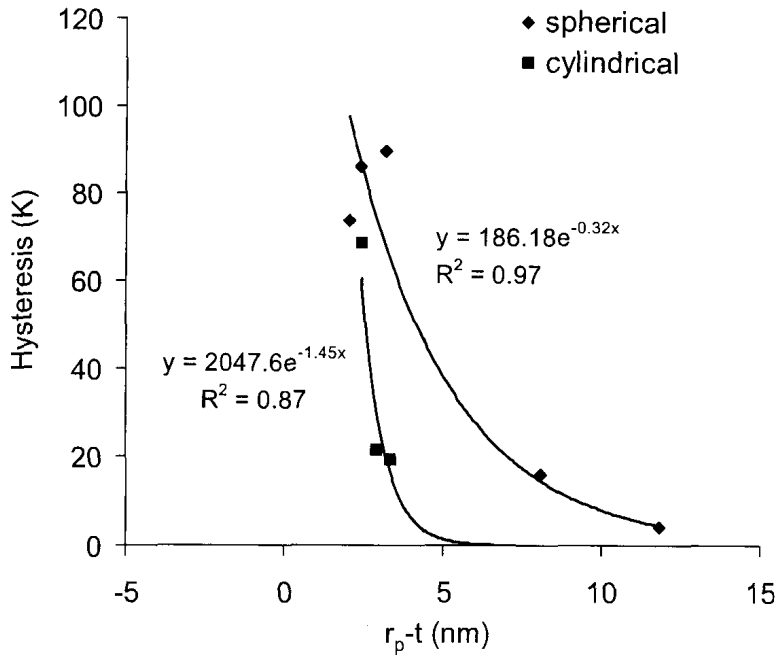

Figure 4.17. Hysteresis plotted as a function of effective pore radius $r_p - t$ for the spherical and cylindrical pore systems.

To further describe the relationship between the cylindrical and spherical pore systems, we determined the ratio of the change in the freeze-melt hysteresis of $C_{10}H_8$ in the spherical system versus the cylindrical system. Figure 4.17 shows a plot of hysteresis values as a function of effective pore radius $r_p - t$ for both cylindrical and spherical pores. Data from the spherical pores clearly indicates that with increasing effective pore radii, the hysteresis value approaches zero. It is unreasonable for hysteresis to take negative values because that would imply that ΔT_f is less than ΔT_m, but as explained in the hysteresis model (Figure 4.15) this is not possible. Thus, it appears that with increasing pore size hysteresis approaches, but does not reach, zero. As hysteresis exists even in the bulk (*ie.* no confinement), this trend is intuitively reasonable. Because the cylindrical pores used in this study were relatively small, we do not see this approach to zero in the data. However, it is clear that

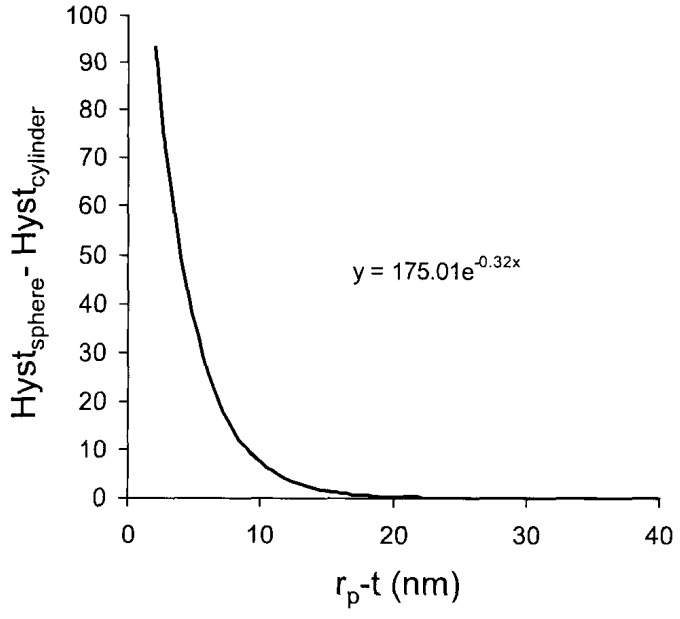

Figure 4.18. Difference in hysteresis values $Hyst_{sph} - Hyst_{cyl}$ as a function of effective pore radius $r_p - t$.

hysteresis cannot decrease linearly with increasing pore size as it would eventually take on negative values. We suggest that with larger cylindrical pore radii, hysteresis would also approach zero as with the spherical pores.

Using the equations of the exponential fits for each pore shape shown in Figure 4.17, we were able to calculate the hysteresis values for a range of effective pore sizes $r_p - t$. The difference in hysteresis values of spherical versus cylindrical pores $Hyst_{sph} - Hyst_{cyl}$ as a function of $r_p - t$ could then be plotted as shown in Figure 4.18. In this way, we were able to relate the differences in hysteresis for spherical and cylindrical pores of comparable pore radii. It is clear that the change in hysteresis increases much faster with increasing spherical pore size compared to that of the cylindrical system. From the equation of the trend line we found that at approximately $r_p - t = 26$ nm, the difference in hysteresis values for the two geometries is 0.0. Thus, it appears that as pore size increases beyond 26 nm, hysteresis becomes independent of pore geometry.

4.5 Raman Spectroscopic Studies

From the above heat plots from the evaporation experiment in spherical pore S2 we were able to determine the presence of a contact layer which does not participate in the phase transition. However, the mass of the contact layer is very small and so it may be questionable whether the phase transition was simply undetectable. To verify the nature of this layer we obtained the Raman spectra of $C_{10}H_8$ participating in only the contact layer and compared it to that of $C_{10}H_8$ filling the entire pore. To ascertain the sample containing $C_{10}H_8$ in the contact layer only was correctly prepared (*ie.* no $C_{10}H_8$ exists outside the layer), a portion of the sample was used to obtain a DSC thermogram. Figure 4.20 indicates that all $C_{10}H_8$ present is within the contact layer as no thermal event has occurred. The Raman experiments were performed using sample S2 at room temperature, which is well below the melting point of naphthalene confined in this pore size. If the contact layer does participate in the phase transition we can expect both spectra to indicate the solid phase, but if the contact layer remains adsorbed on the pore wall we expect the spectra to differ. The results are presented in Figure 4.19. For comparison, the spectra of pure solid naphthalene (PS) and liquid naphthalene (dissolved in CCl_4) (CL) are also shown.

Table 4.5 summarizes the changes in several Raman bands which are sensitive to phase transition in naphthalene. The low-frequency shift of the C-H stretching mode v_9 indicates a liquid $\rightarrow$ solid transition in pure naphthalene. At room temperature the frequency of this band in the contact layer corresponds to that of the bulk liquid at about 3063 cm^{-1}, while the frequency when naphthalene is occupying the entire pore is in accordance with the pure solid at about 3055 cm^{-1}. In the pure liquid and contact layer spectra, a peak appears at approximately 3051 cm^{-1} which is not seen in either the pure solid or full pore spectra. According to Stenman,[46] the Raman

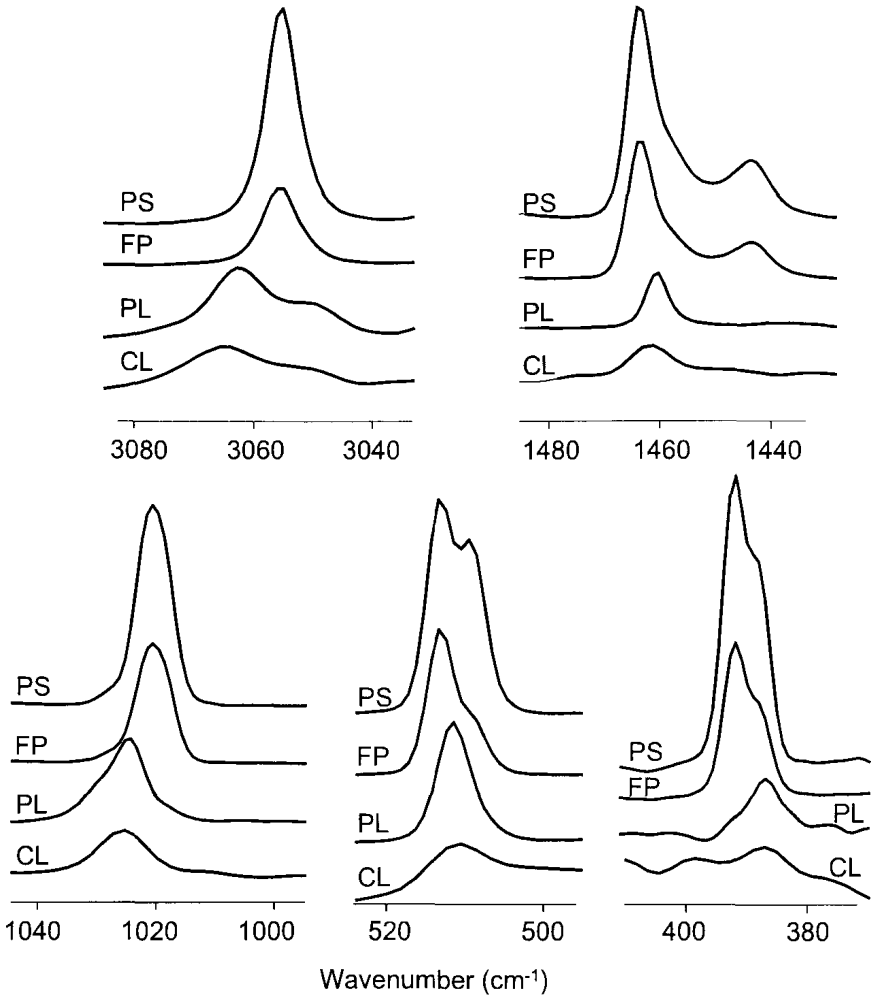

Figure 4.19. Raman spectra of pure solid naphthalene (PS), liquid naphthalene (PL), naphthalene confined in pores (80% loading) (FP), and naphthalene coating the pore walls (CL).

spectrum of solid $C_{10}H_8$ shows single peaks at 3051 and 3056 cm^{-1} with relative intensities of 4 and 27, respectively. The latter corresponds with the peak seen at 3055 cm^{-1} (mode v_9) in our solid spectra, but the peak at 3051 cm^{-1} (mode not assigned) is not observed due to its low relative intensity in the solid state.

Similarly, the β(CCH) in-plane bending vibration mode v_6 shows a low-frequency shift from 1463 cm^{-1} in the full pore to 1460 cm^{-1} in the contact layer. The ν(CC) C-C stretching mode v_3 at a frequency of 1021 cm^{-1} also displays a low-frequency

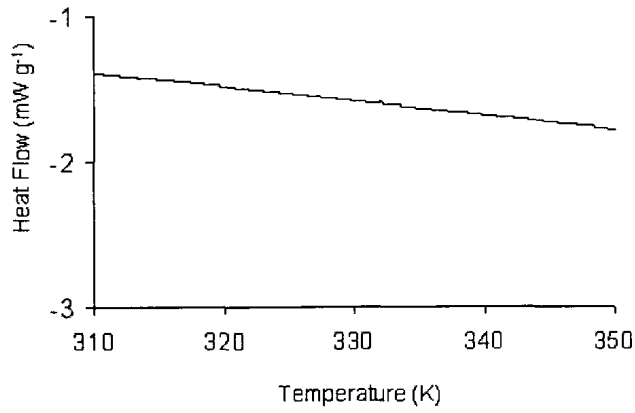

Figure 4.20. DSC thermogram of naphthalene existing as the contact layer in S2.

shift in the contact layer.

Band-splitting can be observed in the α(CCC) in-plane angle deformation mode v_1. The liquid and contact-layer bands at 511 cm^{-1} split into doublets at 509 and 513 cm^{-1} in the solid and full pore. Band splitting also occurs in the v_{13} mode, which represents the intramolecular non-planar torsional vibration of the carbon skeleton ϕ(CC). The frequency at 386 cm^{-1} in the contact layer splits into two frequencies at 388 and 392 cm^{-1} in the full pore.

Furthermore, the v_{21} fundamental C-H stretching mode is seen only in the spectra of the pure solid and the full pore. The intensity of this band decreases quite significantly in the pure liquid and contact layer spectra such that we cannot assign a frequency. These results are comparable to work done by Hanson and Gee[47] and Schnepp and McClure[48], where this band is observed in the pure crystal Raman spectrum, but not in that of the vapor.

From the Raman spectra we conclude that the contact layer does indeed exist as a non-freezing liquid adsorbed on the pore surface, verifying the results from our DSC studies.

Table 4.5. Raman assignments for selected $C_{10}H_8$ frequencies in cm^{-1} at RT

Pure Solid	Pure Liquid	Full Pore	Contact Layer	Mode[a]		Vibration
3055	3063	3056	3064	A_g	υ_9	C-H stretch
1464	1460	1464	1460		υ_6	β(CCH)in-plane H bending
1021	1025	1021	1026		υ_3	ν(CC)C-C stretching
514 509	511	513 509	512		υ_1	α(CCC) in-plane angle deformation
392 388	387	392 388	386	B_{2g}	υ_{13}	ϕ(CC) intramolecular non-planar torsional vibration
1444	-	1443	-	B_{3g}	υ_{21}	fundamental C-H stretch
-	3050	-	3051	-	-	-

[a]Assignments from literature.[47,49,50]

4.6 Powder XRD Studies

The possibility that growing a crystal inside a small pore may result in a crystal structure different from that of the bulk has been previously mentioned by Jackson and McKenna.[39] If this were the case, all of the thermodynamic parameters defined in the Gibbs-Thomson and modified Gibbs-Thomson equations would change. To this effect, powder X-ray diffraction patterns of naphthalene existing inside and outside of spherical pore S2 were obtained in order to determine whether or not confinement causes a change in the crystal structure. In a typical experiment for the former, the total pore volume of the mesoporous sample was calculated after degassing and the amount of $C_{10}H_8$ required to fill the pores was introduced. The sample tube was flame-sealed, heated at 135 °C for several hours, and then allowed to cool on the bench. To prepare a comparable sample in which $C_{10}H_8$ is outside of the pores, the amount of $C_{10}H_8$ required to fill the pores was ground into a powder and physically mixed with the mesopore sample prior to spectral acquisition. Heating was not

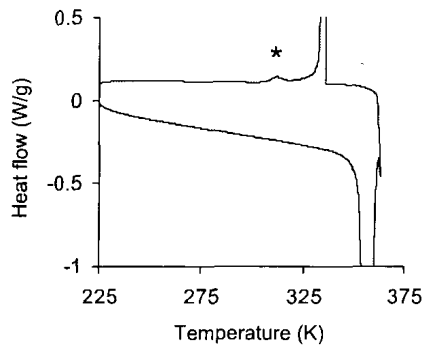

Figure 4.21. DSC thermogram of $C_{10}H_8$ existing outside pores. Confined freezing event (*) is due to heating cycle.

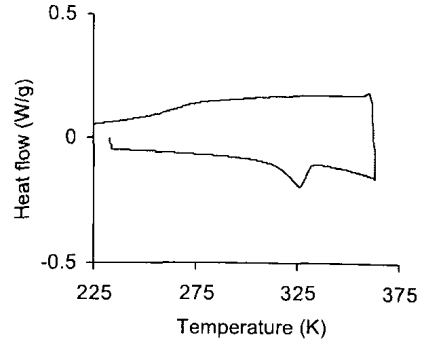

Figure 4.22. DSC thermogram of $C_{10}H_8$ existing only inside pores exhibiting the confined melting transition.

required.

To ensure the samples were correctly prepared we first acquired DSC thermograms. We expected that for the sample in which $C_{10}H_8$ exists outside the pores, the DSC curve will show no confined melting transition of the solid. For the sample in which $C_{10}H_8$ resides only inside the pores, we expected to see only the confined phase transitions. Figures 4.21 and 4.22 present typical DSC curves of these samples, where only the bulk transitions can be seen in Figure 4.21 and only the confined transition is seen in Figure 4.22. Note that the DSC curve corresponding to the sample containing $C_{10}H_8$ outside of the pores there is no confined melting transition, but a confined freezing event does take place as indicated by the asterisk (*). This occurs because during the heating cycle of the DSC experiment, liquid $C_{10}H_8$ can enter the pores, giving rise to a confined freezing transition upon subsequent cooling. For the DSC curve corresponding to the sample containing $C_{10}H_8$ inside the pores, the confined melting transition is quite obvious but the freezing transition appears to have broadened into the baseline.

Figure 4.23 illustrates the powder XRD patterns of $C_{10}H_8$ inside and outside of pore S2 at room temperature. We have already determined in Section 4.2 using

DSC that both bulk $C_{10}H_8$ and $C_{10}H_8$ inside pore S2 are solid at this temperature, so our experimental conditions are appropriate for crystal structure analysis. Our powder patterns were comparable to the pattern simulated based on work by Brock and Dunitz[14]; the assignments of the reflections shown in the figure were taken from their findings.

It is clear from Figure 4.23 that the overall powder powder patterns are the same, indicating that crystallization in the pore does not cause a change in the crystal structure. There is, however, a shift in the 2θ values to lower angles in the pattern for confined naphthalene. This implies a larger d-spacing in confinement, or lattice expansion. This expansion is the result of the interfacial energy and mutual surface tension attraction of the confined material.[51] In the first-order reflection (001), $2\theta = 14.72°$ for $C_{10}H_8$ outside the pore (bulk), but $14.34°$ for confined $C_{10}H_8$. This results in d_{001} values of 6.99 and 7.17 nm, respectively.

It is well known that compared to the bulk, there is a broadening in the full-width at half-height (FWHH) of XRD reflections of nanoparticles. This has been shown in a variety of nanomaterials such as silver, silica, diamond and transition metal complexes.[51–54] This line broadening is attributed to the lattice strain induced by stress due to the excess volume of grain boundaries of the nanoparticles and surface dislocations.[54–56] In comparing the FWHH values of our powder patterns, we have found that there is indeed line broadening in confined $C_{10}H_8$. The most significant broadening can be seen in the (200), $(21\bar{1})$, and (210) reflections. The FWHH of these lines are greater than their corresponding bulk lines by 0.10 to 0.18°. The broadening seen throughout the confined pattern further verifies that the shift in the 2θ values is a result of confinement. The specific FWHH values are indicated in Table 4.6.

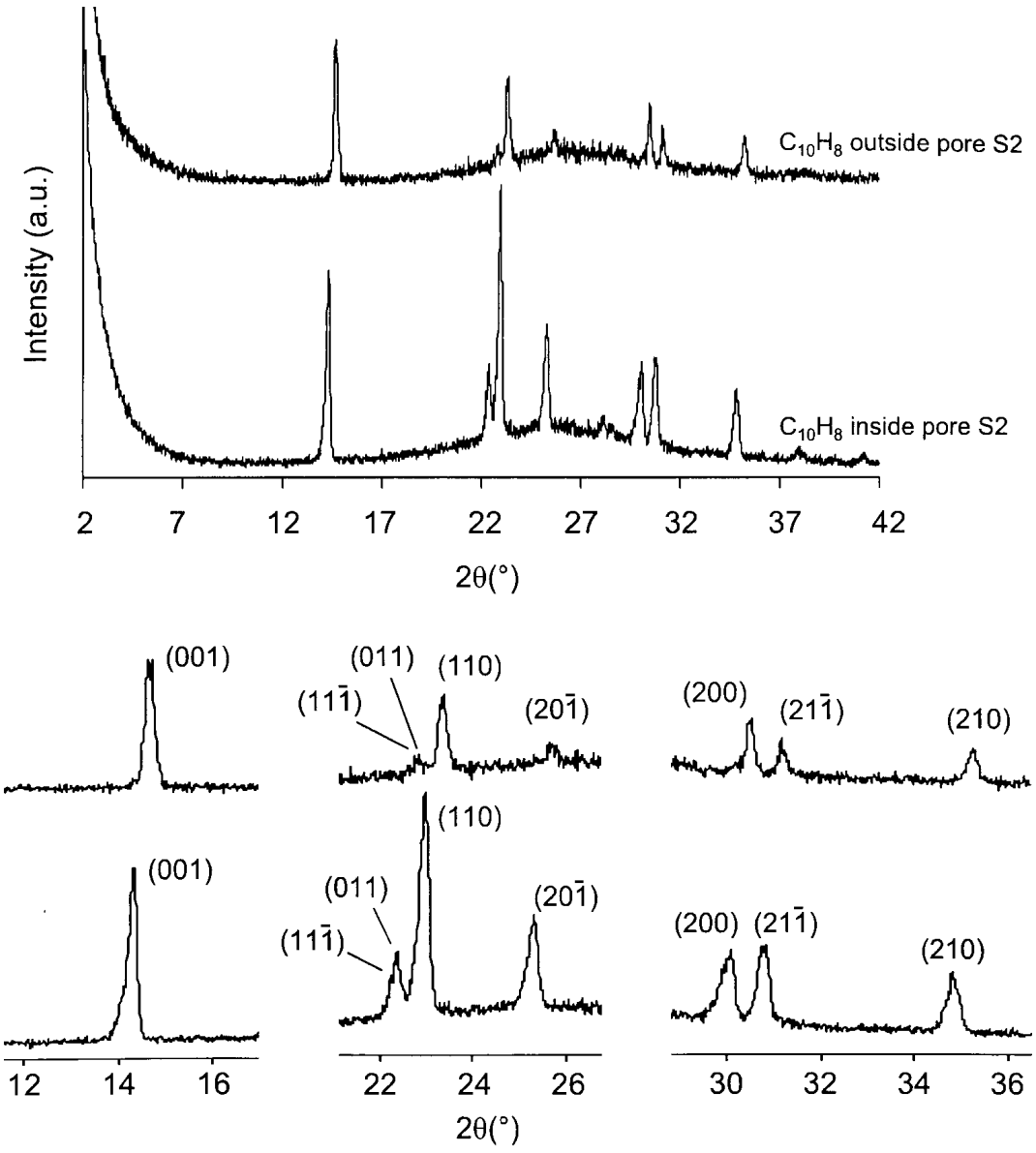

Figure 4.23. Powder XRD patterns of $C_{10}H_8$ existing outside and inside of pore S2. Reflections are expanded below.

Table 4.6. Comparison of FWHH values for reflections in bulk and confined $C_{10}H_8$ powder XRD patterns

Reflection	FWHH	
	Bulk	Confined
(001)	0.22	0.26
$(11\bar{1})(011)$	0.20	0.24
(110)	0.20	0.24
$(20\bar{1})$	0.22	0.28
(200)	0.16	0.34
$(21\bar{1})$	0.20	0.32
(210)	0.22	0.32

4.7 Conclusions

It is well known that materials in confinement undergo a shift in phase transition temperature. Using differential scanning calorimetry we have shown that confined naphthalene exhibits a phase transition temperature depression which is dependent on both pore size and geometry, where a greater degree of confinement results in greater depression. The Gibbs-Thomson implies that the melting temperature depression varies inversely with pore radius, while according to the modified Gibbs-Thomson equation it varies inversely with the effective pore radius. Although our results appear to agree quite reasonably with the Gibbs-Thomson equation, we chose to use the modified Gibbs-Thomson equation because it accounts for the thickness t of the non-freezing contact layer. For specific samples of particular pore sizes, we used DSC to experimentally deduce the amount of confined $C_{10}H_8$ which is actually participating in the phase transition. In this way we were able to verify that there is indeed some quantity of naphthalene inside the pores which does not undergo phase transition. We then calculated t for that pore size and, applying the modified Gibbs-Thomson

equation, we were able to determine t for the other pores in that particular system. Although t has sometimes been assumed constant, this assumption is unreasonable for our case and we have found that t generally decreases with decreasing pore size. Based on the heat of the transition in the DSC experiment we were then able to use this information to calculate the enthalpy ΔH of the confined transition.

The origin of hysteresis in confinement differs from that of the bulk and is related to the differences in pore geometry of the two systems, specifically the surface-to-volume ratios and curvatures.[21] For both the spherical and cylindrical pore systems, we have found that the freeze-melt hysteresis generally increases with decreasing pore size. That is, ΔT_f is greater than ΔT_m and increases more quickly with decreasing pore size. The increase in ΔT_f relative to ΔT_m is 1.6 times faster for spherical pores than cylindrical pores, and this trend is consistent with the literature.[21] In plotting our hysteresis data as a function of pore radius for both geometries we have found that the relationship cannot be linear, as this would imply that hysteresis becomes negative as pore size increases. We therefore propose that the change in hysteresis must be exponential, approaching zero for large pores. From the equations of these exponential relationships, we were able to calculate the hysteresis values for a range of spherical and cylindrical pores sizes. We have found that the difference in hysteresis values between spherical and cylindrical pores ($Hyst_{sph} - Hyst_{cyl}$) of comparable radii decreases exponentially with increasing effective pore radius until approximately 26 nm, where hysteresis appears to become independent of pore geometry.

Furthermore, we have also demonstrated on a molecular level using Raman spectroscopy that the contact layer is indeed non-freezing. The frequency shifts of modes v_3, v_6, and v_9 and the band splitting of modes v_1 and v_{13} seen in the liquid spectrum of CCl_4 mirror those observed in the contact layer. Similarly, both spectra show a dramatic decrease in intensity of the v_{21} peak into the baseline. These obvious differences from the solid spectrum are indicative of the liquid nature of the contact

layer.

Using powder X-ray diffraction we have shown that although there is no change in crystal structure of $C_{10}H_8$ in confinement, there is a lattice expansion. These conclusions were drawn due to the fact that bulk and confined $C_{10}H_8$ gave rise to the same powder pattern, but the reflections in the confined pattern were shifted to lower 2θ angles. The resulting lattice expansion from $d_{001} = 6.99$ nm in the bulk to 7.17 nm inside the pore occurs due to the interfacial energy and surface tension attraction in confinement. In comparing the spectra of bulk and confined $C_{10}H_8$ we have found that there is a global line broadening of up to 0.18° in the confined spectrum, further verifying that the shift in 2θ occurred as a result of confinement.

References

[1] Rodriguez, S.; Bishop, P. L. *J. Env. Eng.* **2008**, *7*, 505–512.
[2] Bleeker, E. A. J.; der Geest, H. G. V.; Klamer, H. J. C.; Voogt, P. D.; Wind, E.; Kraak, M. H. S. *Polycyclic Aromat. Compd.* **1999**, *13*, 191–203.
[3] Cooper, B. H.; Donnis, B. B. L. *Appl. Catal., A* **1996**, *137*, 203–223.
[4] Stanislaus, A.; Cooper, B. H. *Catal. Rev.-Sci. Eng.* **1994**, *36*, 75–123.
[5] Fujikawa, T.; Chiyoda, O.; Tsukagoshi, M.; Idei, K.; Takehara, S. *Catal. Today* **1998**, *45*, 307–312.
[6] Knudsen, K. G.; Cooper, B. H.; Topsøe, H. *Appl. Catal., A* **1999**, *189*, 205–215.
[7] Meng, X. C.; Wu, Y. X.; Li, Y. D. *J. Porous Mater.* **2006**, *13*, 365–371.
[8] Albertazzi, S.; Rodríguez-Castellón, E.; Livi, M.; Jiménez-López, A.; Vaccari, A. *J. Catal.* **2004**, *228*, 218–224.
[9] Svishchev, I. M.; Plugatyr, A.; Nahtigal, I. G. *J. Chem. Phys.* **2008**, *128*, 124514–1–124514–7.
[10] Grimme, S. *Angew. Chem. Int. Ed.* **2008**, *47*, 3430–3434.
[11] Pratt, L. R. *Annu. Rev. Phys. Chem.* **2002**, *53*, 409–436.
[12] Chandler, D. *Nature* **2005**, *437*, 640–647.
[13] Tsuzuki, S.; Honda, K.; Uchimaru, T.; Mikami, M. *J. Chem. Phys.* **2004**, *120*, 647–659.
[14] Brock, C. P.; Dunitz, J. D. *Acta Crystallogr., Sect.B: Struct. Crystallogr. Cryst. Chem.* **1982**, *38*, 2218–2228.
[15] Mitchell, J.; Strange, J. H. *Mol. Phys.* **2004**, *102*, 1997–2005.
[16] Lide, D. R. *Enthalpy of Fusion in CRC Handbook of Chemistry and Physics, 88th Edition*; CRC Press/Taylor and Francis, Boca Raton, FL, 2007.
[17] Faivre, C.; Bellet, D.; Dolino, G. *Eur. Phys. J. B* **1999**, *7*, 19–36.
[18] Hatakeyma, T.; Kasuga, H.; Tanaka, M.; Hatakeyama, H. *Thermochim. Acta* **2007**, *465*, 59–66.
[19] Alba-Simionesco, C.; Coasne, B.; Dosseh, G.; Dudziak, G.; Gubbins, K. E.; Radhakrishnan, R.; Sliwinska-Bartkowiak, M. *J. Phys.: Condens. Matter* **2006**, *18*, R15–R68.
[20] Gibbs, J. *Collected Works*; Yale University Press: New Haven, CT, 1928.
[21] Petrov, O.; Furó, I. *Phys. Rev. E* **2006**, *73*, 011608–1 – 7.
[22] Dosseh, G.; Xia, Y.; Alba-Simionesco, C. *J. Phys. Chem. B* **2003**, *107*, 6445–6453.
[23] Evans, R.; Marconi, U. M. B. *J. Chem. Phys.* **1987**, *86*, 7138–7148.
[24] Sliwinksa-Bartkowiak, M.; Gras, J.; Sikorski, R.; Radhakrishnan, R.; Gelb, L. D.; Gubbins, K. E. *Langmuir* **1999**, *15*, 6060–6069.

[25] Alcoutlabi, M.; McKenna, G. B. *J. Phys.: Condens. Matter* **2005**, *17*, R461–R524.
[26] Radhakrishnan, R.; Gubbins, K. E.; Sliwinska-Bartkowiak, M. *J. Chem. Phys.* **2000**, *112*, 11048–11057.
[27] Christenson, H. K. *J. Phys.: Condens. Matter* **2001**, *13*, R95–R133.
[28] Schreiber, A.; Ketelsen, I.; Findenegg, G. H. *Phys. Chem. Chem. Phys.* **2001**, *3*, 1185–1195.
[29] Morishige, K.; Nobuoka, K. *J. Chem. Phys.* **1997**, *107*, 6965–6969.
[30] Sliwinska-Bartkowiak, M.; Dudziak, G.; Sikorski, R.; Gras, R.; Radhakrishnan, R.; Gubbins, K. E. *J. Chem. Phys.* **2001**, *114*, 950–962.
[31] Booth, H. F.; Strange, J. H. *Mol. Phys.* **1999**, *15*, 5403–5409.
[32] Shao, Y.; Hoang, G.; Zerda, T. W. *J. Non-Cryst. Solids* **1995**, *182*, 309–314.
[33] Tang, X. P.; Wang, J. C.; Cary, L. W.; Kleinhammes, A.; Wu, Y. *J. Am. Chem. Soc.* **2005**, *127*, 9255–9259.
[34] Takahara, S.; Nakano, M.; Kittaka, S. *J. Phys. Chem. B* **1999**, *103*, 5814–5819.
[35] Miyahara, M.; Gubbins, K. E. *J. Chem. Phys.* **1997**, *106*, 2865–2880.
[36] Meziane, A.; Grolier, J.-P. E.; Baba, M.; Nedelec, J. M. *Faraday Discuss.* **2007**, *136*, 384–394.
[37] Billamboz, N.; Baba, M.; Grivet, M.; Nedelec, J. M. *J. Phys. Chem. B* **2004**, *108*, 12032–12037.
[38] Baba, M.; Nedelec, J. M.; Lacoste, J. *J. Phys. Chem. B* **2003**, *107*, 12884–12890.
[39] Jackson, C. L.; McKenna, G. B. *J. Chem. Phys.* **1990**, *93*, 9002–9011.
[40] Turnbull, D. *J. Appl. Phys.* **1950**, *21*, 1022–1028.
[41] Dunning, W. J. *Dunning, W. J.*
[42] Jones, D. R. H. *J. Mater. Sci.* **1974**, *9*, 1–17.
[43] Grzyll, L. R.; Ramos, C.; Black, D. D. *J. Chem. Eng. Data* **1996**, *41*, 446–450.
[44] Morineau, D.; Dosseh, G.; Alba-Simionesco, C.; Llewellyn, P. *Philos. Mag. B* **1999**, *79*, 1847–1855.
[45] Zu, Q.; Sharp, I. D.; Yuan, C. W.; Yi, D. O.; Liao, C. Y.; Glaeser, A. M.; Minor, A. M.; Beeman, J. W.; Ridgwa, M. C.; Kluth, P.; III, J. W. A.; Chrzan, E. D.; Haller, E. E. *Phys. Rev. Lett* **2006**, *97*, 155701–1–155701–4.
[46] Stenman, F. *J. Chem. Phys.* **1971**, *54*, 4217–4222.
[47] Hanson, D. M.; Gee, A. R. *J. Chem. Phys.* **1969**, *51*, 5052–5062.
[48] Schnepp, O.; MClure, D. S. *J. Chem. Phys* **1962**, *36*, 1375–1382.
[49] Dollish, F. R.; Fateley, W. G.; Bentley, F. F. *Characteristic Raman Frequencies*; John Wiley & Sons: New York, 1974.
[50] Michaelian, K. H.; Ziegler, S. M. *Appl. Spectrosc.* **1973**, *27*, 13–21.
[51] Wei, Z.; Xia, T.; Ma, J.; Feng, W.; Dai, J.; Wang, Q.; Yan, P. *Mat. Char.* **2007**, *58*, 1019–1024.
[52] Miao, J.; Hu, C.; Liu, H.; Xiong, Y. *Mater. Lett.* **2008**, *62*, 235–238.
[53] DiNunzio, P. E.; Martelli, S. *Aerosol. Sci. Technol.* **2006**, *40*, 724–734.
[54] Biju, V.; Sugathan, N.; Vrinda, V.; Salini, S. L. *J. Mater. Sci.* **2008**, *43*, 1175–

Chapter 5

Confinement Effects on the Phase Transition of Naphthalene Derivatives

5.1 Introduction

From our studies regarding naphthalene confined in cylindrical and spherical mesoporous silicas we have found that the phase transition temperature depression increases with decreasing pore size, and that the freeze-melt hysteresis increases more dramatically with decreasing pore size in a spherical pore geometry. However, it is also important to the understanding of confined phase behaviour to examine the effects of molecular properties, so to further our studies on confined naphthalene, we selected several naphthalene derivatives to examine. Specifically, we chose 2-methylnaphthalene (2-$C_{10}H_7CH_3$), 2-methoxynaphthalene (2-$C_{10}H_7OCH_3$), and 2-chloronaphthalene (2-$C_{10}H_7Cl$), shown in Figure 5.1.

The three derivatives are substituted at the same position on the parent $C_{10}H_8$ moiety, but the moieties differ in their electronic properties; for example the methoxy group is strongly electron donating, while the choloro group is electron withdrawing. These properties affect the aromatic π system of the naphthalene ring, thereby

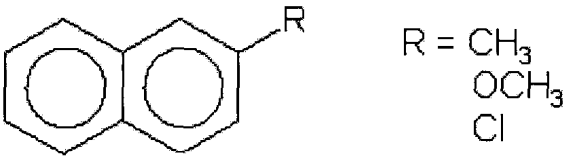

Figure 5.1. Naphthalene derivatives used in this study.

affecting the molecule's ability to interact with the pore surface through π-type hydrogen bonding.[1,2] Because an increase in interactions with the surface causes a greater melting point depression,[1] we expect that 2-$C_{10}H_7OCH_3$ will show the greatest depression, followed by 2-$C_{10}H_7CH_3$, $C_{10}H_8$, and 2-$C_{10}H_7Cl$. In examining and relating the properties with the trends of the behaviour of these derivatives in confinement, we hope to expand our studies on confined aromatic organics.

5.2 DSC Studies in Confinement

To ensure that we could accurately measure the transition temperatures and enthalpies of confined naphthalene derivatives, we first acquired the DSC thermograms of the pure compounds. Figures 5.2, 5.3, and 5.4 present the thermograms for pure 2-methylnaphthalene, 2-methoxynaphthalene, and 2-chloronaphthalene, respectively, upon heating and then cooling. The onset melting temperature for 2-$C_{10}H_7CH_3$ was found to be 307.80 K, which is in accordance with the literature value of 307.8 K,[3] and the freezing onset is 300.55 K. The enthalpy of fusion for melting and freezing were 82.85 and 83.66 J g^{-1}, respectively, and also in accordance with the literature value of 85.30 J g^{-1}.[3] According to Chanh *et al.*,[4] 2-methylnaphthalene undergoes a solid-state transition at 291 K upon melting (253 K upon freezing), but our thermograms

do not indicate such event for either pure 2-$C_{10}H_7CH_3$ or when it is introduced to a porous host material. Solid 2-$C_{10}H_7CH_3$ belongs to monoclinic space group $P2_1/c$;[4] however, we have been unable to find crystal structure data for this molecule.

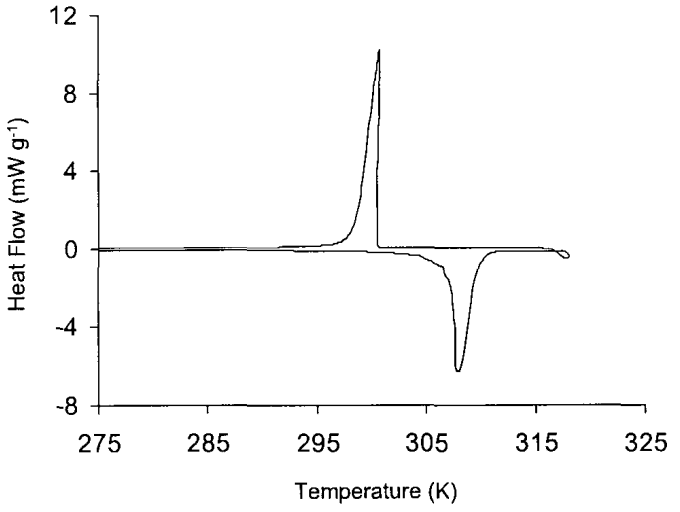

Figure 5.2. DSC curve of pure 2-methylnaphthalene upon heating and cooling.

The melting and freezing onsets of 2-$C_{10}H_7OCH_3$ were found to be 346.47 and 322.84 K, respectively. The melting onset is in good agreement with the literature value of 346.6 K.[3] The enthalpy of fusion for melting has a value of 152.60 J g^{-1} and that for freezing has a value of 139.30 J g^{-1}. To the best of our knowledge, there are no previous reports of ΔH in the literature for comparison. As such, we obtained several thermograms of pure 2-$C_{10}H_7OCH_3$ on two different instruments for comparison. The enthalpy values were consistent between the experiments and so we report 152.60 J g^{-1} as the bulk ΔH value. Crystalline 2-$C_{10}H_7OCH_3$ is monoclinic and belongs to space group $P2_1/c$ with $Z = 4$.[5] The crystal structure is shown in Figure 5.5.

The DSC thermogram of pure 2-$C_{10}H_7Cl$ provided a melting onset temperature

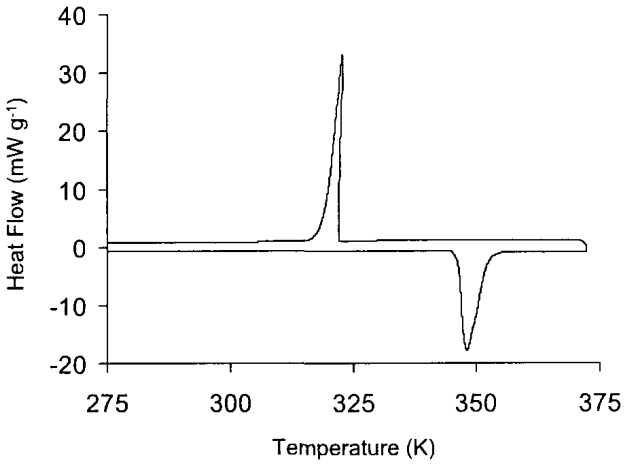

Figure 5.3. DSC curve of pure 2-methoxynaphthalene upon heating and cooling.

of 331.01 K, which agrees with the literature value of 331.15 K.[3] The freezing temperature onset was 326.33 K, and the enthalpies of fusion for melting and freezing were 85.21 and 83.03 J g^{-1}, in good accordance with the literature value of 86.0 J g^{-1}.[3] It has been shown that some 2(R)-substituted naphthalene compounds (R=F, Cl, Br) exhibit crystalline order-disorder transitions[6]. This type of transition corresponds with substructure phenomena in the direction of crystallographic axis c in the monoclinic cell system due to the re-orientational motions of the molecules from form II (semi-ordered) to form I (totally disordered) at higher temperature.[4,7] Form II belongs to space group $P2_1/c$ with $Z = 4$, whereas Form I, isostructural with naphthalene, belongs to space group $P2_1/a$ with $Z = 2$.[7,8] The crystal structure of Form II is shown in Figure 5.6. In the inset of Figure 5.4 the transition between these two forms is indicated by arrows; the solid-solid transition from form II to form I upon melting occurs at 314.95 K, comparable to findings by Chanh *et al.*,[4] and the transition from form I to form II upon freezing occurs at 297.57 K. This phase transi-

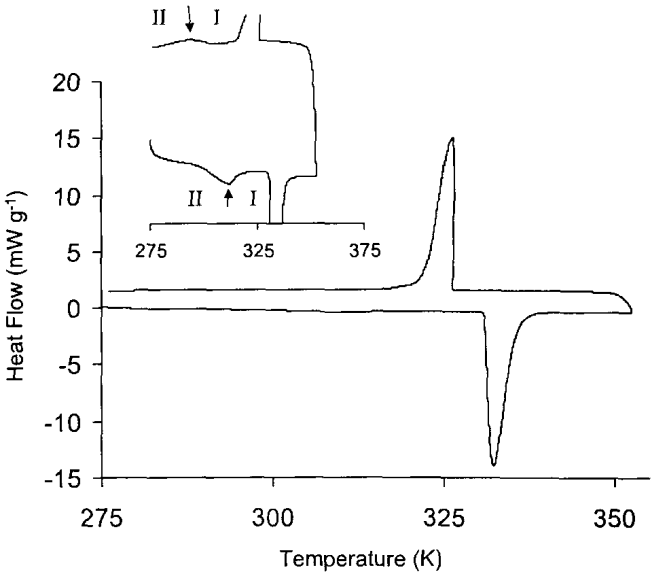

Figure 5.4. DSC curve of pure 2-chloronaphthalene upon heating and cooling.

tion has also been reported to occur over a large temperature range from 253 - 320 K during melting, but is seen in the DSC curve as a low, broad transition where only the peak maximum near the high temperature limit of the transition is visible.[8,9] In our thermograms, we were only able to see the peak maximum at high temperature as shown in the figure.

In comparing the ΔH values of the solid-liquid transitions for 2-$C_{10}H_7CH_3$, 2-$C_{10}H_7OCH_3$ and 2-$C_{10}H_7Cl$, it can be noted that the enthalpy of this transition is almost twice as great for 2-$C_{10}H_7OCH_3$ than the others. This is due to the fact that 2-$C_{10}H_7OCH_3$ does not undergo a solid-solid transition; thus when the liquid phase undergoes a phase change into the ordered solid, there is a great decrease in the entropy; *ie.* ΔS has a large absolute value. Conversely, because form I (high temperature) of solid 2-$C_{10}H_7Cl$ is highly disordered,[7] the entropy change associated with the phase change from the liquid form is relatively small. Specifically, in form I

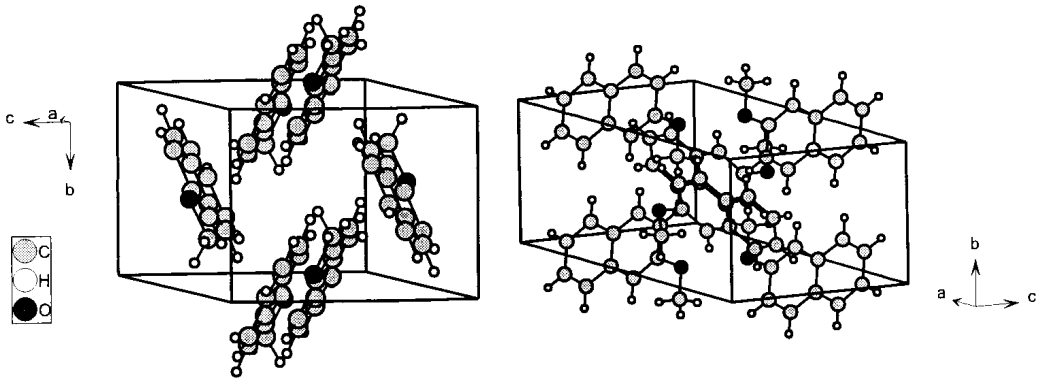

Figure 5.5. Two views depicting the monoclinic crystal structure of 2-$C_{10}H_7OCH_3$.

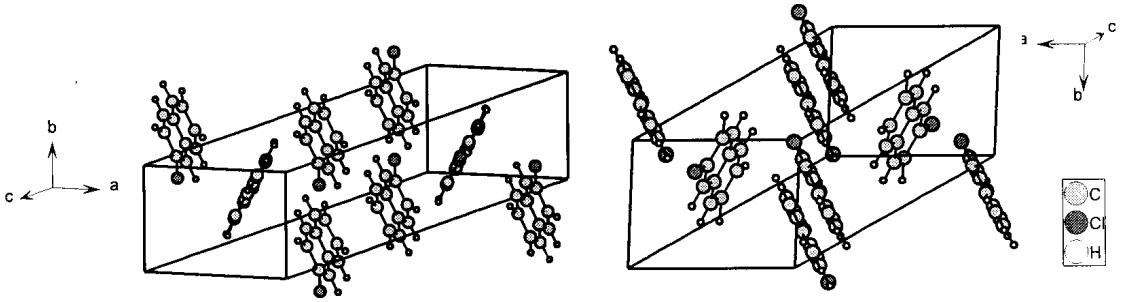

Figure 5.6. Two views depicting the monoclinic crystal structure of 2-$C_{10}H_7Cl$.

the occupancy factor of two of the four β (2-substituted) sites for chlorine is 0.33 while the other two are 0.17. In the semi-ordered form II crystal, one of the four molecular orientations is predominant (occupancy factors of 0.64, 0.11, 0.09, and 0.16).[8] Since $\Delta S = \Delta H/T$, where T is the temperature at which the process occurs, it follows that ΔH for the liquid to solid transition is comparably smaller for 2-$C_{10}H_7Cl$ than for 2-$C_{10}H_7OCH_3$ since 2-$C_{10}H_7OCH_3$ does not have a disordered solid form. Similarly, the high-temperature form of crystalline 2-$C_{10}H_7CH_3$ is also disordered, while the low-temperature form is semi-disordered.[4,7] The phase transition from the liquid to the disordered high-temperature solid also results in a relatively small change in entropy and, thus, enthalpy.

As in the case with naphthalene in Chapter 4, there is a freeze-melt hysteresis between the melting and freezing events of each of the three derivatives due to the small delay in the heterogeneous freezing nucleation of the pure liquid.[10] Again, the melting temperature is then identified with the true transition temperature and taken as the reference transition temperature T_0 in our studies.

The volume of each cylindrical mesoporous sample was calculated from nitrogen sorption data and the correct mass of 2-$C_{10}H_7CH_3$, 2-$C_{10}H_7OCH_3$, or 2-$C_{10}H_7Cl$ was introduced to achieve approximately 60% overload as with the studies for naphthalene. In this way we were able to obtain the DSC melting and freezing curves of both the bulk and confined organic for comparison. They can be seen in Figure 5.7, Figure 5.8, and Figure 5.9. The peaks corresponding to solid $\leftrightarrow$ liquid phase transitions of the confined $C_{10}H_8$ derivatives are denoted by arrows, and it can be seen that both melting and freezing transition temperatures decrease with pore diameter. Summaries of these values can be found in Table 5.1 for 2-$C_{10}H_7CH_3$, Table 5.2 for 2-$C_{10}H_7OCH_3$, and Table 5.3 for 2-$C_{10}H_7Cl$. Note that for the bulk transitions, the tangent to the peak represents the beginning of the transition process and determines the transition temperature, but in the confined phases the transition temperature is

Table 5.1. DSC values of the transition temperatures, transition temperature shifts (ΔT), and hysteresis values of 2-$C_{10}H_7CH_3$ confined in cylindrical pores

Sample	r_p (nm)	t (nm)	T_0 (K)	T_m (K)	T_f (K)	ΔT_m (K)	ΔT_f (K)	Hysteresis
bulk	-	-	-	307.80	300.55	-	-	7.25
C1	4.0	1.2†	305.86	272.46	252.16	33.41	53.70	20.29
C2	3.3	0.8	305.75	268.91	245.01	36.84	60.74	23.90
C3	2.8	0.7	305.23	260.82	228.33	44.41	76.90	32.49

† Extrapolated from experimental data.

taken at the maximum of the peak because of broadening.[10,11]

Upon closer inspection of the confined 2-$C_{10}H_7Cl$ DSC thermograms in Figure 5.9, it appears that there are two confined transition peaks for freezing. The two peaks are obvious for 2-$C_{10}H_7Cl$ in sample C2, and they occur at 253.97 and 270.69 K. The peak at lower temperature appears in the thermogram corresponding to C1 at 254.82 K, while the second peak appears at a higher temperature of 278.87 K. These two peaks are due to the confined solid-solid and liquid-to-solid transitions, respectively. The thermogram for the smallest pore C3 indicates two overlapping peaks at 247.90 and 250.37 K. The breadths of the confined liquid-solid transition peaks for C1 and C2 were approximately 18 and 20 K, respectively, while the total breadth of the overlapping peaks in C1 is almost 40 K. This further indicates that these are indeed two separate peaks, and not one broad peak. The asterisks (*) and triangles (∇) denote solid-solid transitions of the bulk and confined materials, respectively.

In plotting ΔT_m as a function of r_p^{-1} according to the Gibbs-Thomson equation we find again that our results do show a reasonably linear trend. The plots are shown in Figure 5.10. However, we have shown using DSC studies and Raman spectroscopy that a contact layer does exist for each of these systems. As such, we determined the thicknesses of the contact layer for each by overloading a sample and recording a

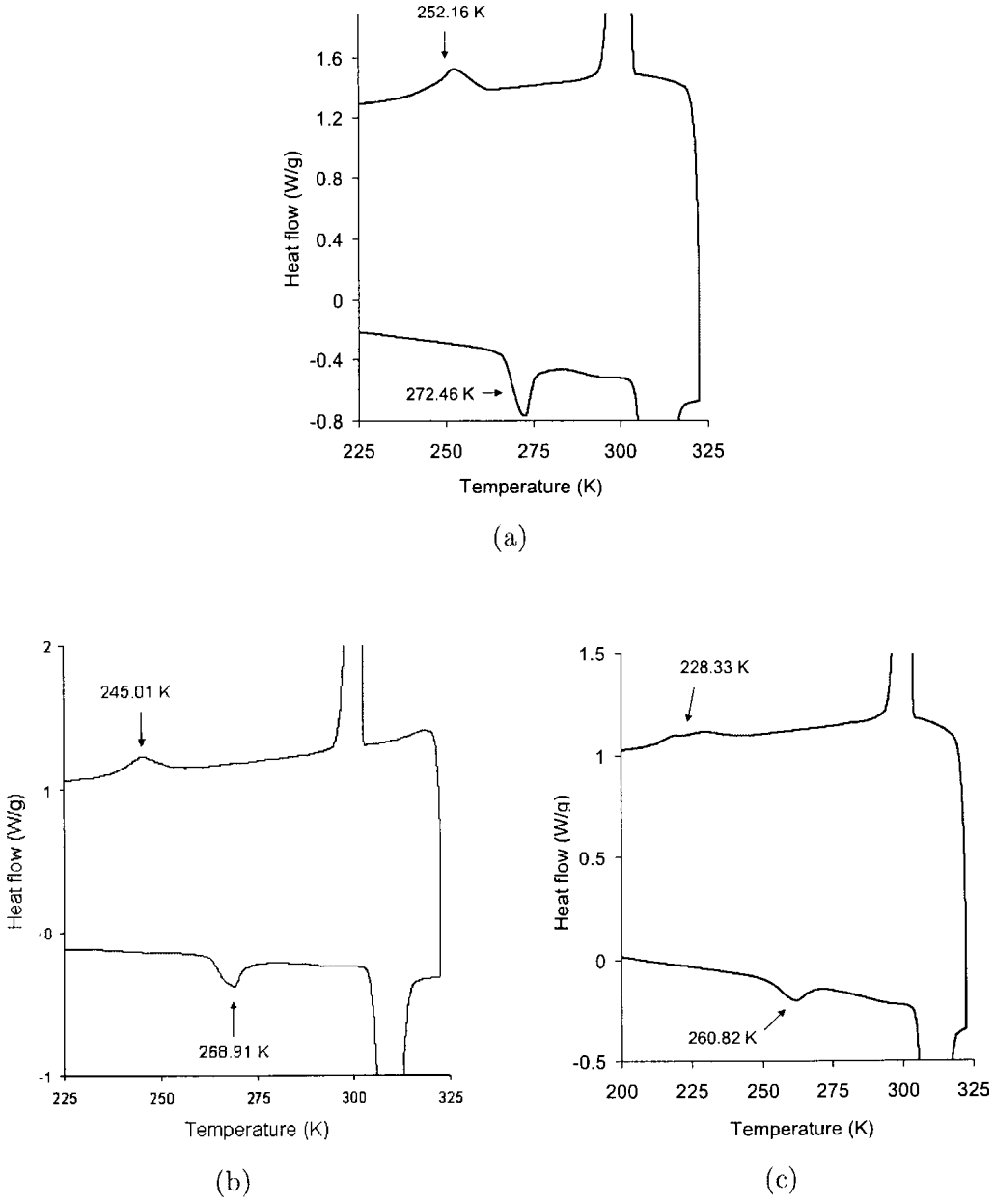

Figure 5.7. DSC thermograms of bulk 2-$C_{10}H_7CH_3$ and 2-$C_{10}H_7CH_3$ confined in cylindrical pores (a)C1, (b)C2, and (c)C3. Confined phase transitions are indicated by arrows and the transition temperatures are given.

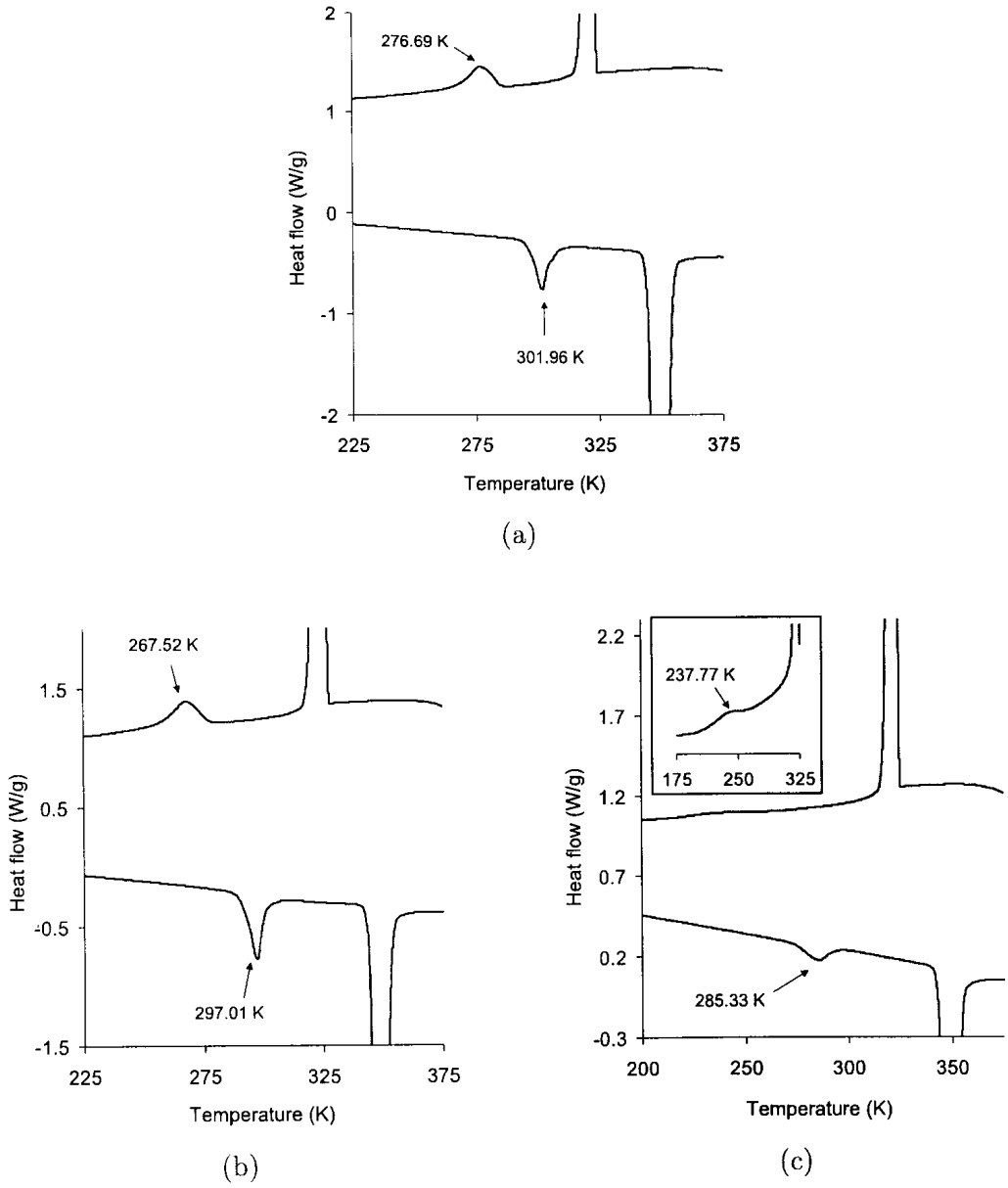

Figure 5.8. DSC thermograms of bulk 2-$C_{10}H_7OCH_3$ and 2-$C_{10}H_7OCH_3$ confined in cylindrical pores (a)C1, (b)C2, and (c)C3. Confined phase transitions are indicated by arrows and the transition temperatures are given.

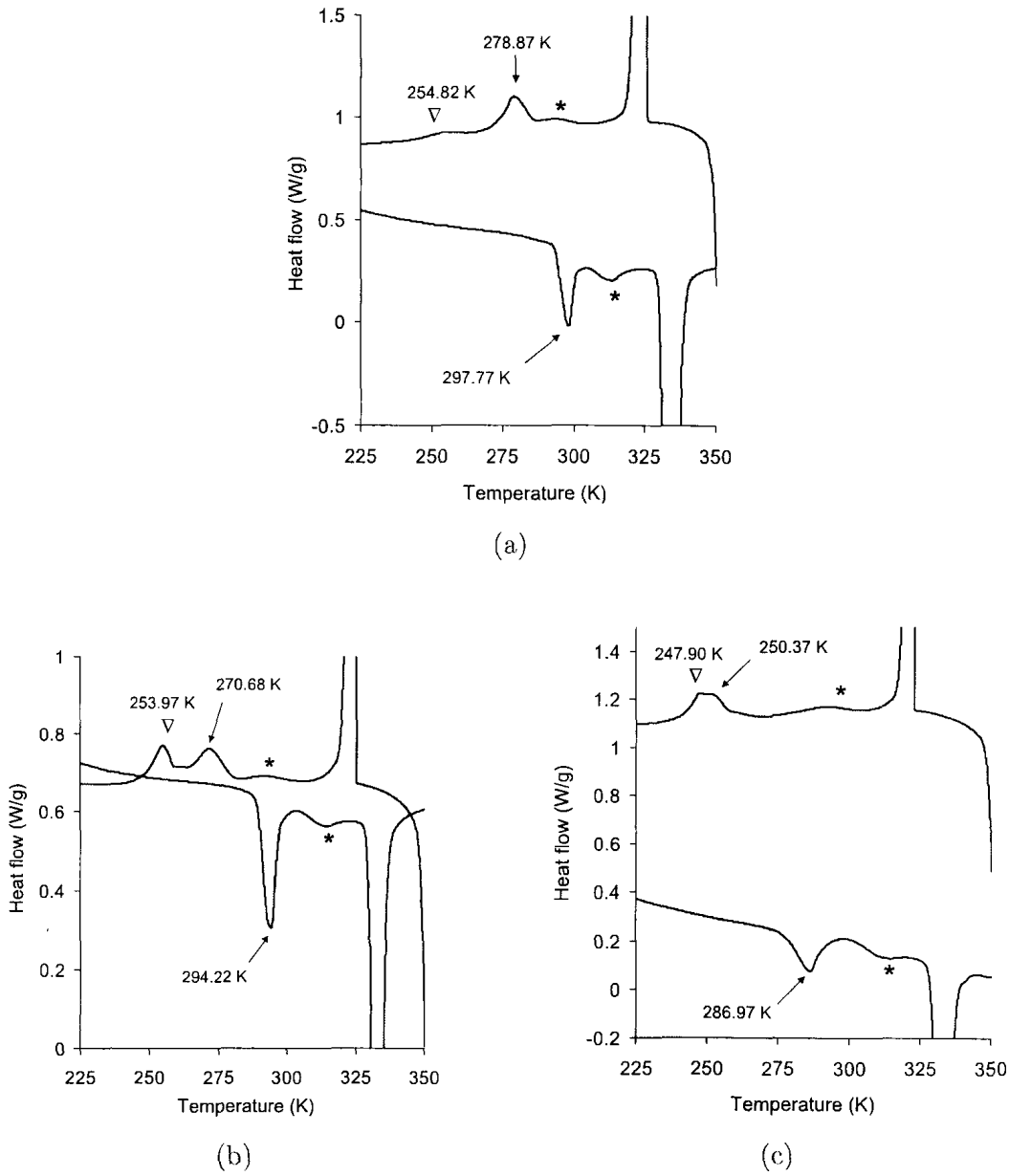

Figure 5.9. DSC thermograms of bulk 2-$C_{10}H_7Cl$ and 2-$C_{10}H_7Cl$ confined in cylindrical pores (a)C1, (b)C2, and (c)C3. Confined phase transitions are indicated by arrows and the transition temperatures are given. The asterisks (*) and triangles (∇) denote solid-solid transitions of the bulk and confined materials, respectively.

Table 5.2. DSC values of the transition temperatures, transition temperature shifts (ΔT), and hysteresis values of 2-$C_{10}H_7OCH_3$ confined in cylindrical pores

Sample	r_p (nm)	t (nm)	T_0 (K)	T_m (K)	T_f (K)	ΔT_m (K)	ΔT_f (K)	Hysteresis
bulk	-	-	-	346.47	322.84	-	-	23.63
C1	4.0	1.5†	344.61	301.96	276.69	42.65	67.92	25.27
C2	3.3	1.1	344.76	297.01	267.52	47.75	77.24	29.49
C3	2.8	1.0	344.50	285.33	237.77	59.17	106.73	47.56

† Extrapolated from experimental data.

Table 5.3. DSC values of the transition temperatures, transition temperature shifts (ΔT), and hysteresis values of 2-$C_{10}H_7Cl$ confined in cylindrical pores

Sample	r_p (nm)	t (nm)	T_0 (K)	T_m (K)	T_f (K)	ΔT_m (K)	ΔT_f (K)	Hysteresis
bulk	-	-	-	331.01	326.33	-	-	7.25
C1	4.0	2.1†	330.80	297.77	278.87	33.03	51.93	18.90
C2	3.3	1.5	330.12	294.22	270.68	35.90	59.44	23.54
C3	2.8	1.3	330.10	286.97	250.37	43.13	79.73	36.60

† Extrapolated from experimental data.

series of thermograms while evaporating from a DSC sample pan. The procedure is described in Section 4.2 and the results can then be applied to the modified Gibbs-Thomson relationship (Equation (4.3)).

Figure 5.11 shows a series of typical thermograms upon evaporation of 2-methylnaphthalene from sample C1. The bulk melting peak is denoted *b* and the confined peak is denoted *c*. Peak *b* gradually decreases as evaporation occurs until there is no bulk 2-$C_{10}H_7CH_3$ left in the sample pan, at which point *c* begins to decrease until there is no confined material left.

A plot of the heats corresponding to peaks *b* and *c* as a function of the quantity of 2-$C_{10}H_7CH_3$ is shown in Figure 5.12. The point at which H_c differs from zero corresponds to the mass of the contact layer m_t. In the portion where H_c remains constant the pores are completely filled and we can measure $H_{c\ max}$. From the plot,

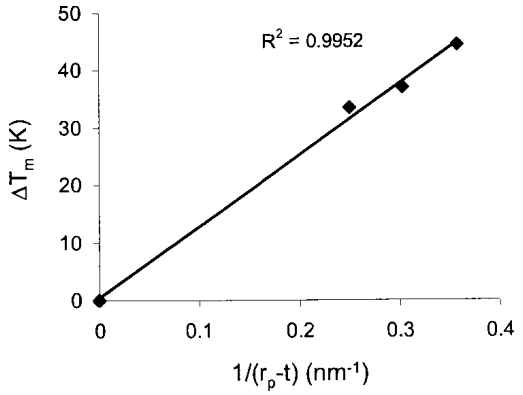

(a)

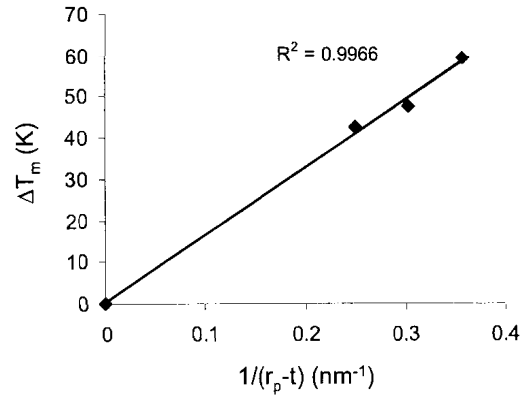

(b)

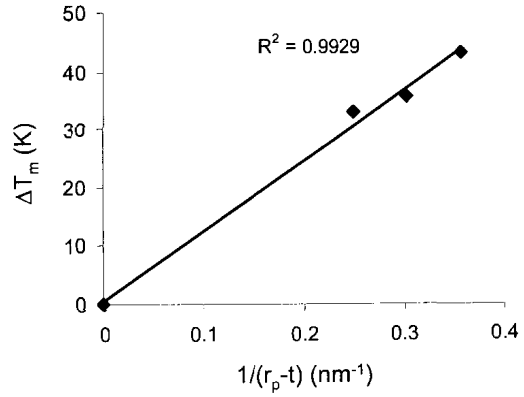

(c)

Figure 5.10. ΔT_m plotted as a function of r_p^{-1} for (a) 2-$C_{10}H_7CH_3$, (b) 2-$C_{10}H_7OCH_3$, and (c) 2-$C_{10}H_7Cl$.

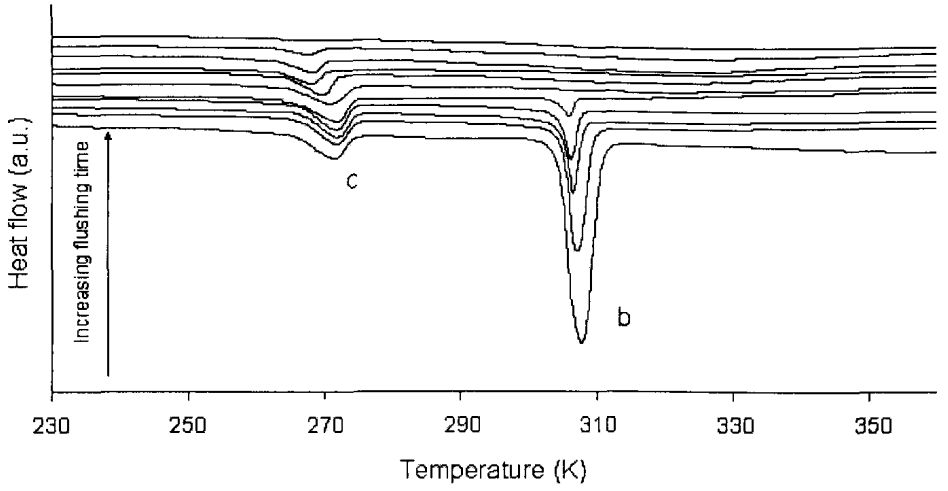

Figure 5.11. Thermograms recorded for various flushing times for sample C1 filled with 2-$C_{10}H_7CH_3$.

the mass required to fill the pores is 1.4 mg. At $H_{c\ max}$ the enthalpy corresponds to the mass of the 2-$C_{10}H_7CH_3$ present m_{vp} minus the mass participating in the contact layer, namely $m = m_{vp} - m_t$. We can then deduce the enthalpy of melting per gram for confined 2-$C_{10}H_7CH_3$ ($\Delta H_c = 31$ J g^{-1}).

Using the mass of the contact layer m_t determined from the plot, we were able to find the thickness t of the non-freezing 2-$C_{10}H_7CH_3$ layer in C1 according to:[12]

$$t = \frac{m_t}{\rho(SSA)(m_{SiO_2})} \tag{5.1}$$

where SSA is the specific surface area of the silica sample given in Table 3.3. Knowing the pore radius r_p and t for C1 we calculated the surface tension $\gamma_{sl} = 12.7$ mJ m^{-2} from Equation (4.3).

We were also able to deduce the porous volume V_p according to:[12]

$$V_p = \frac{m_{vp}}{\rho m_{SiO_2}} \tag{5.2}$$

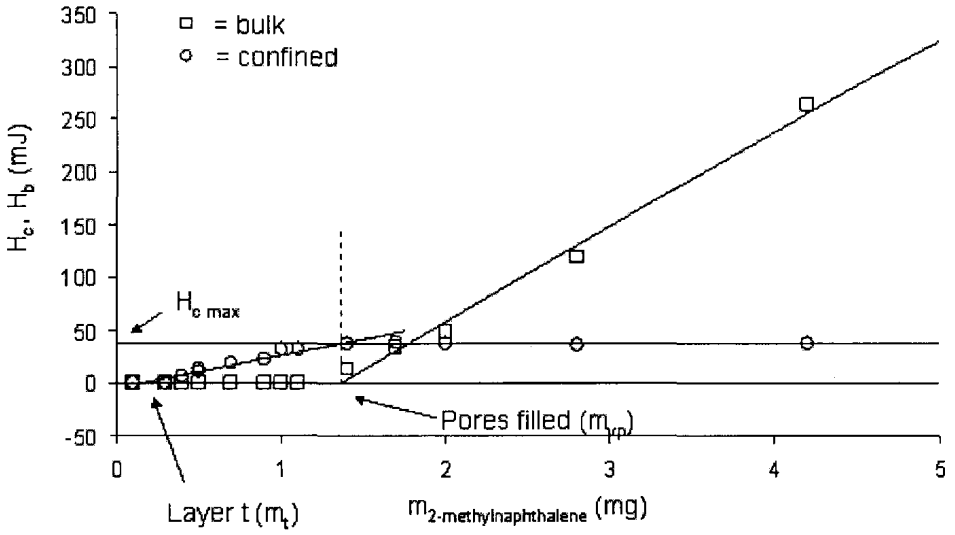

Figure 5.12. Evolution of H_c (○) and H_b (□) as a function of the mass of 2-$C_{10}H_7CH_3$ present in sample C1.

where $\rho = 1.0058$ g mL^{-1} is the solid density of of 2-$C_{10}H_7CH_3$.[3] The value found for V_p is comparable to that obtained by N_2 sorption (V_{N_2}). These results are shown in Table 5.4.

In the same way, we evaporated 2-$C_{10}H_7OCH_3$ and 2-$C_{10}H_7Cl$ from pore C1 and recorded series of thermograms, shown in Figures 5.13 and 5.15. Plots of the heats of the bulk b and confined c peaks as a function of the mass of the organic present are shown in Figures 5.14 and 5.16.

Performing the same series of calculations we were able to determine the thicknesses of the contact layer for each cylindrical pore, the enthalpy ΔH_c in confinement, and the porous volume V_p from the experiments. Results are shown in Table 5.4. The solid density ρ used in the calculations for 2-$C_{10}H_7OCH_3$ was 1.072 g mL^{-1};[3] that for 2-$C_{10}H_7Cl$ was calculated from crystal data parameters[13] to be 1.327 g mL^{-1}. For each system, ΔH_c is much smaller than the corresponding bulk value ΔH_{sl}.

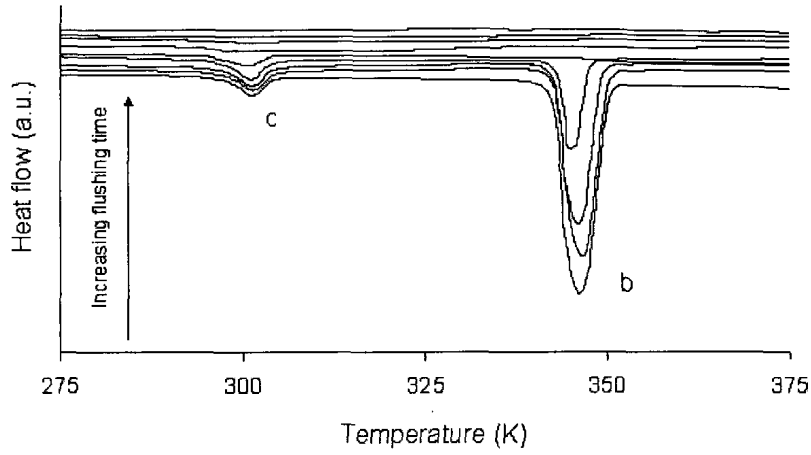

Figure 5.13. Thermograms recorded for various flushing times for sample C1 filled with 2-$C_{10}H_7OCH_3$.

Again, ΔH_c for 2-$C_{10}H_7OCH_3$ is approximately twice the values for 2-$C_{10}H_7CH_3$ and 2-$C_{10}H_7Cl$, maintaining the same general relationship displayed by their bulk values. This indicates that the disordered and semi-ordered solid forms of 2-$C_{10}H_7CH_3$ and 2-$C_{10}H_7Cl$ do exist even in confinement. Furthermore, confinement does not appear to induce a plastically crystalline phase in 2-$C_{10}H_7OCH_3$.

The pore volumes calculated from the experiments with 2-$C_{10}H_7CH_3$ and 2-$C_{10}H_7OCH_3$ are in good agreement with the volume V_{N_2} for C1 determined by nitrogen adsorption porosimetry. The value obtained from 2-$C_{10}H_7Cl$, however, differs from the nitrogen adsorption value. This is a result of the solid-solid transition seen in 2-$C_{10}H_7Cl$. In the DSC thermograms, this peak overlaps with that of the confined solid-liquid transition under study. As such, the heat corresponding to the confined peak is overestimated when there is bulk 2-$C_{10}H_7Cl$ present. The mass of the contact layer, and hence thickness, are also overestimated as a result.

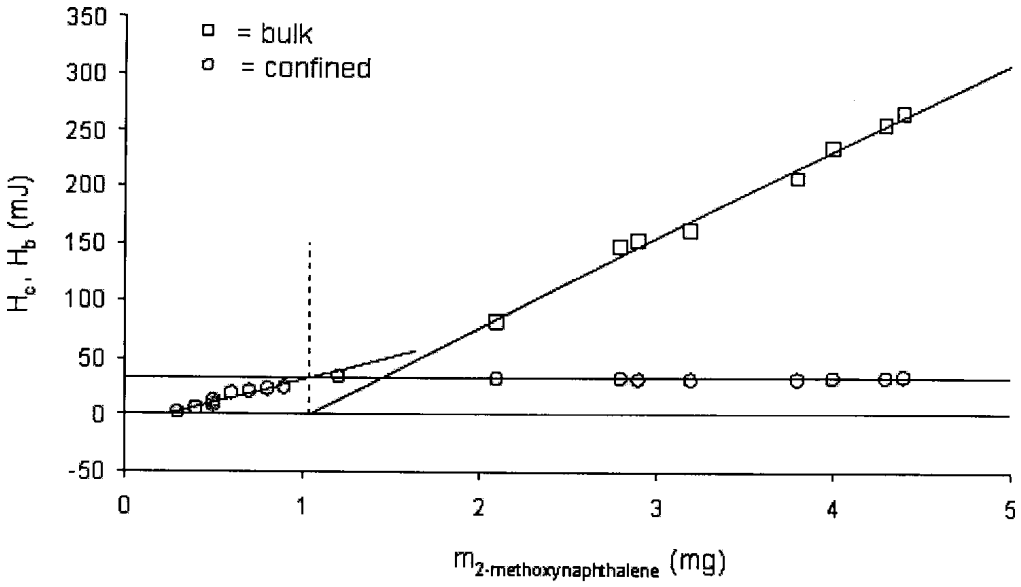

Figure 5.14. Evolution of H_c (O) and H_b (□) as a function of the mass of 2-$C_{10}H_7OCH_3$ present in sample C1.

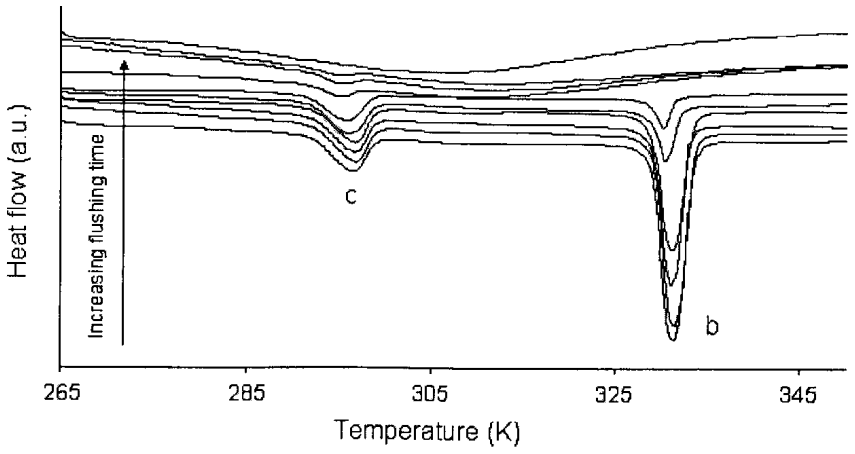

Figure 5.15. Thermograms recorded for various flushing times for sample C1 filled with 2-$C_{10}H_7Cl$.

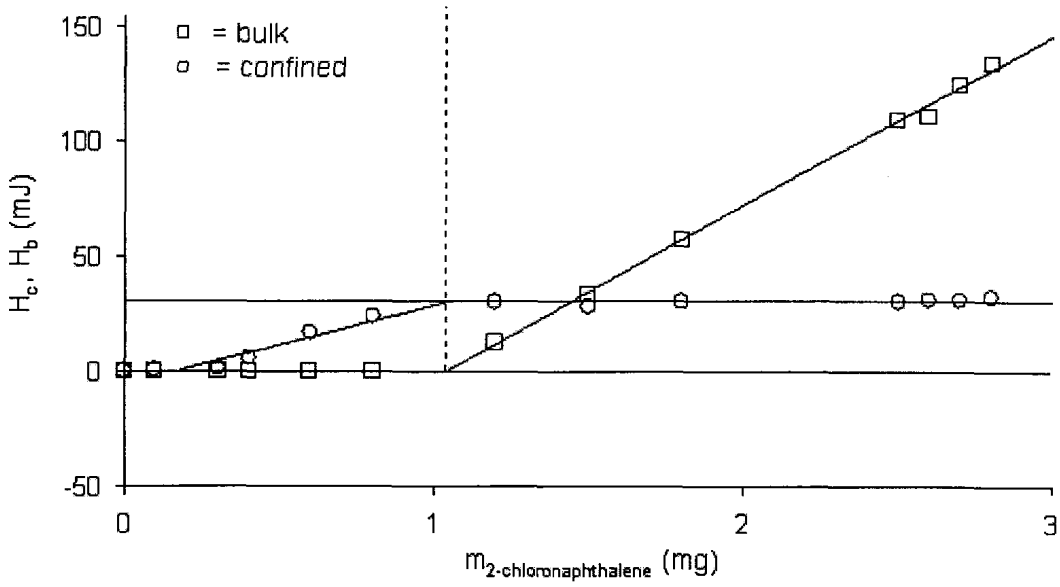

Figure 5.16. Evolution of H_c (○) and H_b (□) as a function of the mass of 2-$C_{10}H_7Cl$ present in sample C1.

Table 5.4. Mass and thickness t, porous volumes and transition enthalpies measured by DSC and N_2 sorption for 2-$C_{10}H_7CH_3$, 2-$C_{10}H_7OCH_3$, and 2-$C_{10}H_7Cl$ in sample C1 (radius 4.0 nm)

Derivative	m_{vp} (mg)	t (nm)	γ_{sl} (mJ m^{-2})	V_p (cm^3 g^{-1})	V_{N_2} (cm^3 g^{-1})	ΔH_c (J g^{-1})
2-$C_{10}H_7CH_3$	0.15	1.2	12.4	0.8	1.03	31
2-$C_{10}H_7OCH_3$	0.12	1.5	25.3	1.0	1.03	70
2-$C_{10}H_7Cl$	0.17	2.1	10.8	1.4	1.03	35

5.3 Comparison of Derivatives

The surface of confining pores may have attractive or repulsive properties which affect the confined material, and it can be surface-modified to replace existing functional groups with other groups.[14] The SBA-15 materials used in this study have not been modified, so their surfaces contain the usual hydroxyl groups[15] which can interact with delocalized π systems through π-type hydrogen bonding.[1,2] This type of bonding has also been found to occur between the hydrogens of water and the π-electronic system of aromatic rings.[16–18] Using the hydrophobic hydration of benzene as an illustrative example of this, there is a small partial negative charge on the carbon atoms of molecule with the periphery hydrogens carrying positive charges. The negative charge on the carbons favours hydrogen bond formation between the central area of the ring and surrounding water molecules.[2] It is known that this π-type hydrogen bonding in naphthalene differs from that of benzene due to a reduction of the negative charge density of the naphthalene π system compared to benzene.[19] To this effect, it is possible that electronic effects from substituent groups on $C_{10}H_8$'s delocalized π system will affect confined phase behaviour.

Because the same system of porous samples was used in this study for each compound, and the only difference between $C_{10}H_8$, 2-$C_{10}H_7CH_3$, 2-$C_{10}H_7OCH_3$, and 2-$C_{10}H_7Cl$ is the group on the 2-position of the parent naphthalene molecule, we were able to draw a comparison between phase behaviour and substituent properties. As $C_{10}H_8$ interacts with the pore surface through its aromatic π system, the electron-withdrawing and electron-donating properties of each substituent affects this interaction through alteration of the electron density.

The strength of the fluid-fluid interaction relative to the fluid-wall interaction plays an important role in determining the sign of the shift of the freezing point,[20]

and the fluid-wall interactions appear to play a crucial role in the melting point depression.[11,14,21] Dosseh *et al.*[11] have found that, using SBA-15 materials with pore diameters between 6 and 14 nm, agreement with the Gibbs-Thomson equation is strongly dependent on surface interactions. According to their study using cyclohexane (C_6H_{12}), benzene, and water in a series of four SBA-15 materials, ΔT_m versus the inverse of the diameter is not linear for cyclohexane, almost linear for benzene, and linear for water. Apparently, the fewer interactions with the surface, the more departure from the Gibbs-Thomson linear relation. This result is questionable as the diameters used in the plot for C_6H_{12} are different than what was reported from the pore-size analysis (though the plotted values for benzene and water do match the reported values). One could also argue that the trendlines are reasonably linear. Furthermore, they compared their results for cyclohexane in SBA-15 with those in the literature for C_6H_{12} in dehydrated porous silica[21] and trimethylsilyl-grafted controlled pore glasses.[14] According to this comparison, the more hydrophobic the pore surface, the more interactions with C_6H_{12} and the smaller the melting point depression. However, geometry is also one of many factors which can affect changes in confined behaviour,[10,22] and in this particular comparison, the three confining materials differ in the surface properties of the pores as well as their geometries. The pores of SBA-15 are cylindrical, those of porous silica are spherical, and CPGs exhibit disordered porous structures of interconnected pores with broad pore size distributions.[23] It is therefore possible that the differences in confined melting point depression could be a result of the hydrophobicities of the various pore surfaces, but could also be attributed to differences in pore shape, pore distribution, or a combination of such factors.

These results by Dosseh et al.[11] are contrary to findings by Takei and coworkers[1], who have shown that for a given pore size, increasing the number of surface hydroxyl groups in the same type of porous silica samples caused a greater melting

point depression for benzene but not for *n*-hexane. *n*-Hexane was determined by IR spectroscopy to have negligible surface interactions with the pore, which is in accordance with their observations that there was no change in the confined melting point with increasing surface hydroxyl groups. They proposed that the interaction between the benzene π electrons with the surface hydroxyl groups causes a change in the liquid structure of benzene, such that benzene molecules in the vicinity of the silica surface are oriented parallel to the surface. Melting point depression occurs as a result, and the degree of orientation depends on the concentration of surface hydroxy groups. Thus a higher degree of interaction results in a greater melting point depression.[1] Based on these findings, the naphthalene derivatives in the present study should follow such trend. As mentioned above, we expect that 2-$C_{10}H_7OCH_3$ will show the greatest depression, followed by 2-$C_{10}H_7CH_3$, $C_{10}H_8$, and 2-$C_{10}H_7Cl$. While our results show that 2-$C_{10}H_7OCH_3$ is indeed further depressed than 2-$C_{10}H_7CH_3$ and 2-$C_{10}H_7Cl$, the overall trend is not in accordance with results by Takei.

$-CH_3$ in 2-$C_{10}H_7CH_3$ is slightly electron donating, and it does this by σ - conjugation from one of the methyl C-H σ bonds.[24] The electron density of the fused-ring portion of 2-$C_{10}H_7CH_3$ is thus increased slightly. In comparison, $-OCH_3$ is heavily electron donating due to the lone electron pair on the oxygen,[24] significantly increasing the electron density of the fused-ring portion of 2-$C_{10}H_7OCH_3$. The increased electron densities in 2-$C_{10}H_7CH_3$ and 2-$C_{10}H_7OCH_3$ in turn improve the molecules' abilities to form hydrogen bonds with surface hydroxyl groups. The greater electron donating capacity of $-OCH_3$ allows 2-$C_{10}H_7OCH_3$ to form stronger π-type hydrogen bonds with the surface. It follows that the melting point depression of 2-$C_{10}H_7OCH_3$ is greater than that of 2-$C_{10}H_7CH_3$, as can be seen in Figure 5.17.

–Cl has three lone pairs of electrons, and one pair may conjugate with the aromatic ring system. However, there is a size mismatch of the 3p orbital of the chlorine atom with the 2p orbital of the carbon atom in the naphthalene ring. For this reason,

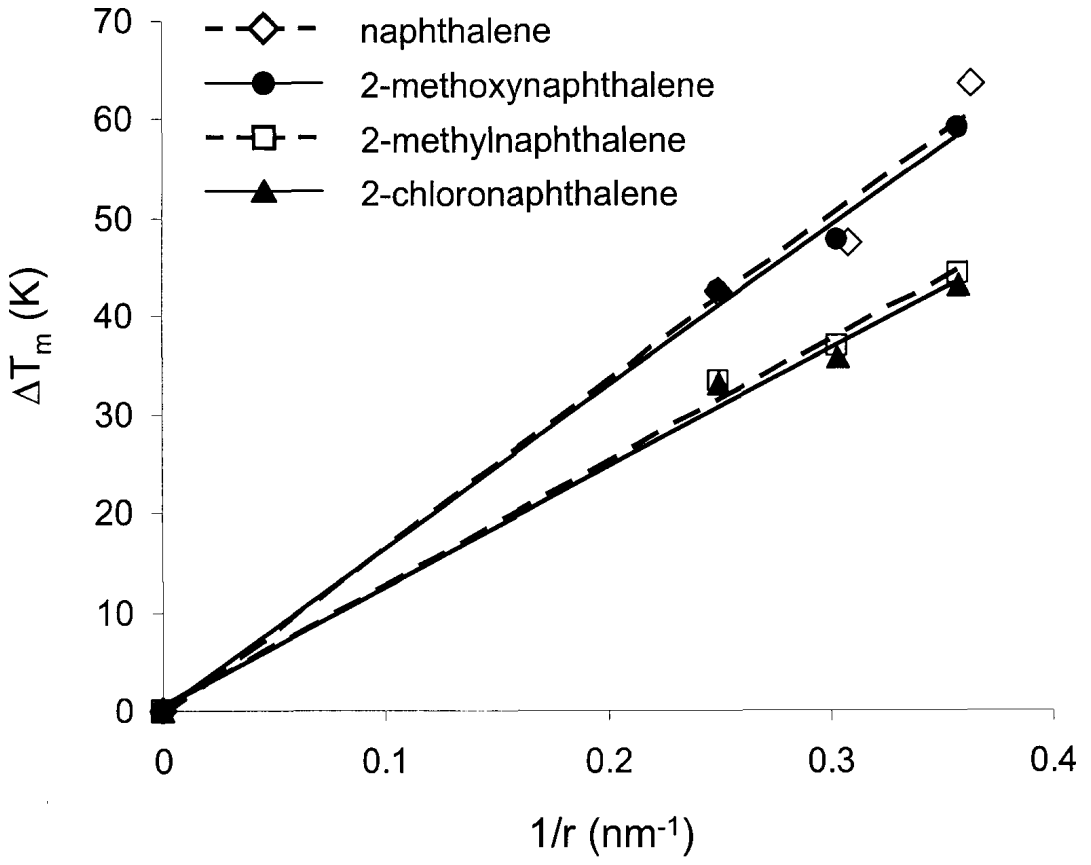

Figure 5.17. Comparison of ΔT_m as a function of r^{-1} for $C_{10}H_8$, 2-$C_{10}H_7CH_3$, 2-$C_{10}H_7OCH_3$, and 2-$C_{10}H_7Cl$.

chlorine is only slightly electron donating; in fact it is strongly electron withdrawing due to its electronegativity.[24] As such, the electron density of 2-$C_{10}H_7Cl$'s π system is decreased, causing a decrease in the molecule's ability to form π-type hydrogen bonds with the surface hydroxyl groups. Of the four compounds, 2-$C_{10}H_7Cl$ generally has the least depressed confined melting point.

However, based on these arguments one would expect that ΔT_m for 2-$C_{10}H_7Cl$ differs more significantly from ΔT_m for 2-$C_{10}H_7CH_3$, and that ΔT_m for unsubstituted $C_{10}H_8$ should be somewhere between 2-$C_{10}H_7CH_3$ and 2-$C_{10}H_7Cl$. However, it is likely that other factors are involved which contribute to ΔT_m. For instance, the effects of size and intermolecular interactions have not been accounted for. Fyfe *et al.*[25] conducted ^{29}Si MAS NMR studies on *p*-dichlorobenzene and *p*-xylene adsorbed in the pores of highly siliceous ZSM-5. They found that it is the shape and size characteristics of organic molecules which are the main factors involved in interactions between the sorbate and the confining walls, as the ^{29}Si NMR spectra of zeolites they obtained were remarkably similar for *p*-dichlorobenzene and *p*-xylene. Furthermore, they found that the spectrum for *p*-chlorotoluene was also very similar, despite the fact that it has a net dipole while the other two do not. This indicates that dipole is not an important factor with regards to the interactions in such systems. Our data shows that 2-$C_{10}H_7CH_3$ and 2-$C_{10}H_7Cl$ have very similar ΔT_m trends, which can be explained by the similar size and shape of the two molecules. However, this reasoning cannot be extended to the similarity of ΔT_m between $C_{10}H_8$ and 2-$C_{10}H_7OCH_3$. In this case, intermolecular interactions may be a factor which requires consideration. In a study of the steric inhibition of such π-π stacking by Moorthy *et al.*,[26] it was found that derivitization of aromatic pyrene molecules with bulky groups impede these interactions. In fact, the sterically hindered aryl rings did not undergo close π-π stacking, leading to solid-state properties that parallel those in the solution state. $C_{10}H_8$, being un-substituted, does not experience steric hinderance of π-π stacking by

functional groups. Interactions between naphthalene rings are therefore undisturbed and the molecules can also interact with the silica surface, which causes molecules near the pore wall to to align in an orderly arrangement, increasing the depression of ΔT_m.[1] In the case of 2-$C_{10}H_7CH_3$ and 2-$C_{10}H_7Cl$, steric hinderance prevents the ordered arrangement of the molecules. The ability for the surface to order the molecules is thus hindered, resulting in a less depressed ΔT_m. Although the methoxy group is a relatively bulky group, its electron donating properties increases the electron density of the aromatic π system of the parent naphthalene moiety. This improves the molecules' ability to form π-type hydrogen bonds with the silica surface as well as π-π stacking interactions with each other. Furthermore, the oxygen from the methoxy group may also interact favourably with hydrogens on the pore surface, increasing the overall ability of 2-$C_{10}H_7OCH_3$ to interact with the surface.

From our results it is clear that electronic effects caused by the different functional groups cannot be the only factor which must be taken into account in the analysis of differences in ΔT_m. Other factors such as relative molecular sizes and shapes and steric hinderance must be considered as well. Ultimately, such factors affect the ability of molecules to interact with the pore surface and the propensity of these interactions determine the degree of depression of ΔT_m. In the case of aromatic molecules in siliceous pores containing surface hydroxyl groups, the surface causes an orderly arrangement of the molecules in its vicinity. This order causes a change in the liquid structure such that it becomes more orderly than the bulk liquid structure. Thus, there is a greater depression in the melting temperature.[1]

5.4 Raman Spectroscopic Studies

Using Raman spectroscopy we were able to show that a non-freezing contact layer does exist for each of these derivatives in confinement, as with naphthalene. We loaded each derivative into sample C1 such that there was only enough to coat the pore walls and form a non-freezing layer. DSC thermograms of the prepared samples were obtained before acquiring the Raman spectra. As shown in Figure 5.18, no phase change occurred in any of the samples, indicating that any material loaded into the pores resides in the vicinity of the pore walls and remain liquid.

All solid spectra were acquired at -100 °C, and the liquid spectra were acquired at room temperature by dissolving in CCl_4. The spectrum of 2-$C_{10}H_7CH_3$ in the contact layer of pore C1 was acquired at -20 °C, 2-$C_{10}H_7OCH_3$ at room temperature, and 2-$C_{10}H_7Cl$ at 0 °C. These temperatures are all below the melting points of their respective $C_{10}H_8$ derivatives confined in pore C1. The spectra are shown in Figures 5.19 through 5.21, and in all cases the pure solid, pure liquid, and contact layer spectra are denoted PS, PL, and CL, respectively.

Figure 5.19 presents some bands from the Raman spectra of pure solid and liquid 2-$C_{10}H_7CH_3$ and 2-$C_{10}H_7CH_3$ in the contact layer of the pore. The differences in the solid and liquid spectra are subtle compared to the differences in $C_{10}H_8$ (Section 4.5), even though the solid spectra were acquired at low temperature. Nevertheless, there are several indicators that contact layer 2-$C_{10}H_7CH_3$ is in the liquid state as the contact layer spectrum resembles that of the liquid spectrum, but not the solid. In the pure solid spectrum, a triplet of peaks can be seen at 2915 cm^{-1} where the most intense of the three occurs at this wavenumber. This triplet is due to the two antisymmetric and one symmetric C-H stretch of the CH_3 group.[27] In the liquid spectrum it is difficult to determine whether all three peaks of the triplet are present

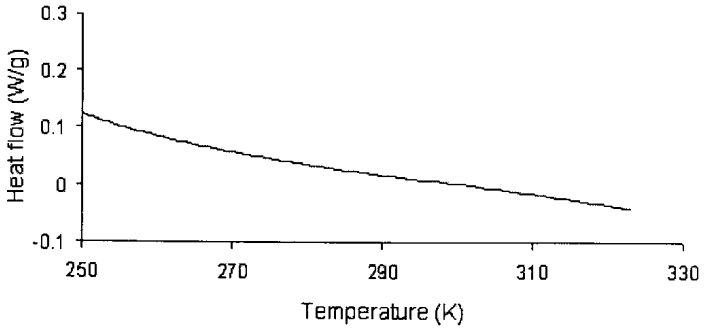

(a)

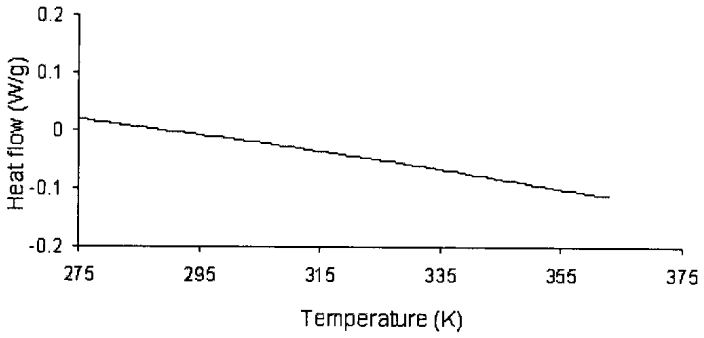

(b)

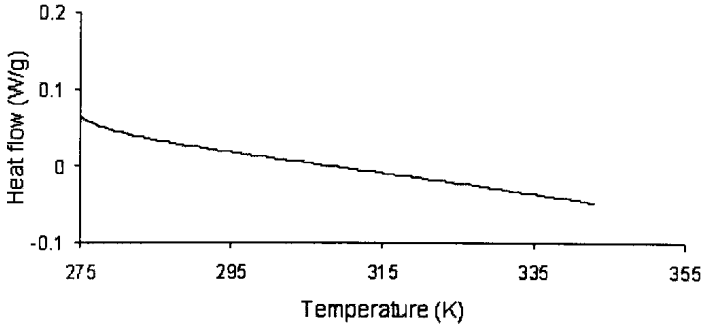

(c)

Figure 5.18. DSC thermograms of (a)2-$C_{10}H_7CH_3$, (b)2-$C_{10}H_7OCH_3$, and (c)2-$C_{10}H_7Cl$ existing as the contact layer in pore C8.

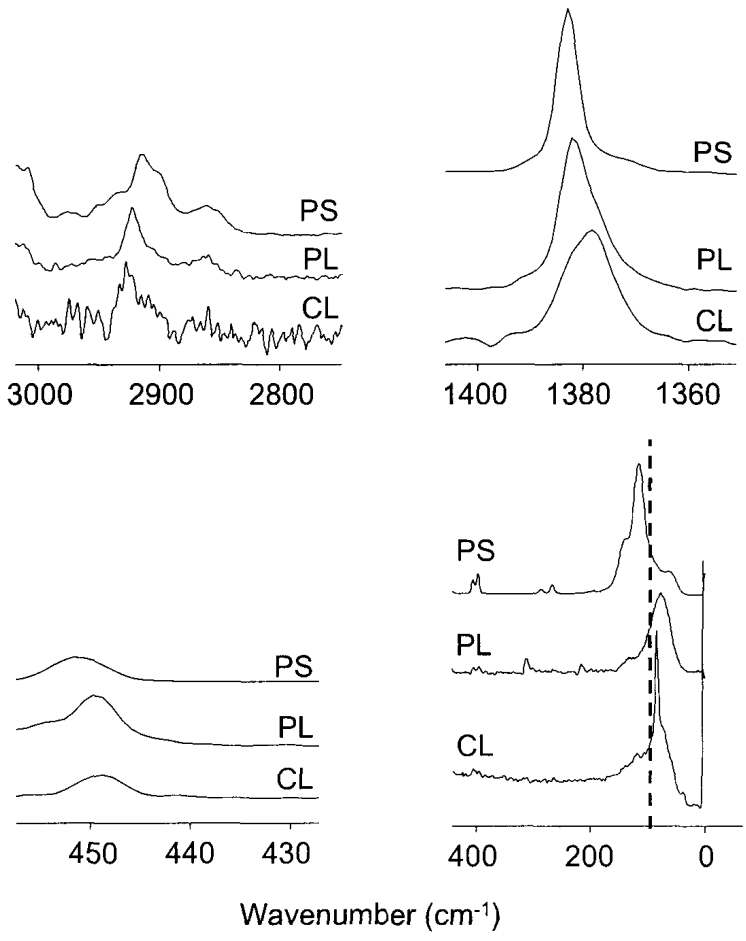

Figure 5.19. Raman spectra of pure solid 2-$C_{10}H_7CH_3$ (PS), pure liquid 2-$C_{10}H_7CH_3$ (PL), and 2-$C_{10}H_7CH_3$ coating the pore walls (CL).

or not because of the low signal intensity, but the maximum of the signal(s) occurs at 2923 cm^{-1}, significantly shifted from the solid spectrum. Similarly, this signal is shifted to 2926 cm^{-1} in the contact layer spectrum. The C-C stretching peak[28] seen in the solid spectrum at 1384 cm^{-1} has a full width at half height (FWHH) of 5 cm^{-1}, and is shifted to 1381 cm^{-1} and broadened to 9 cm^{-1} in the liquid spectrum. The shift and line broadening are even more pronounced in the contact layer spectrum; the peak appears at 1378 cm^{-1} with an FWHH value of 12 cm^{-1}. There is also a low-frequency shift of the ring torsion vibration[28] from 452 cm^{-1} in the solid spectrum

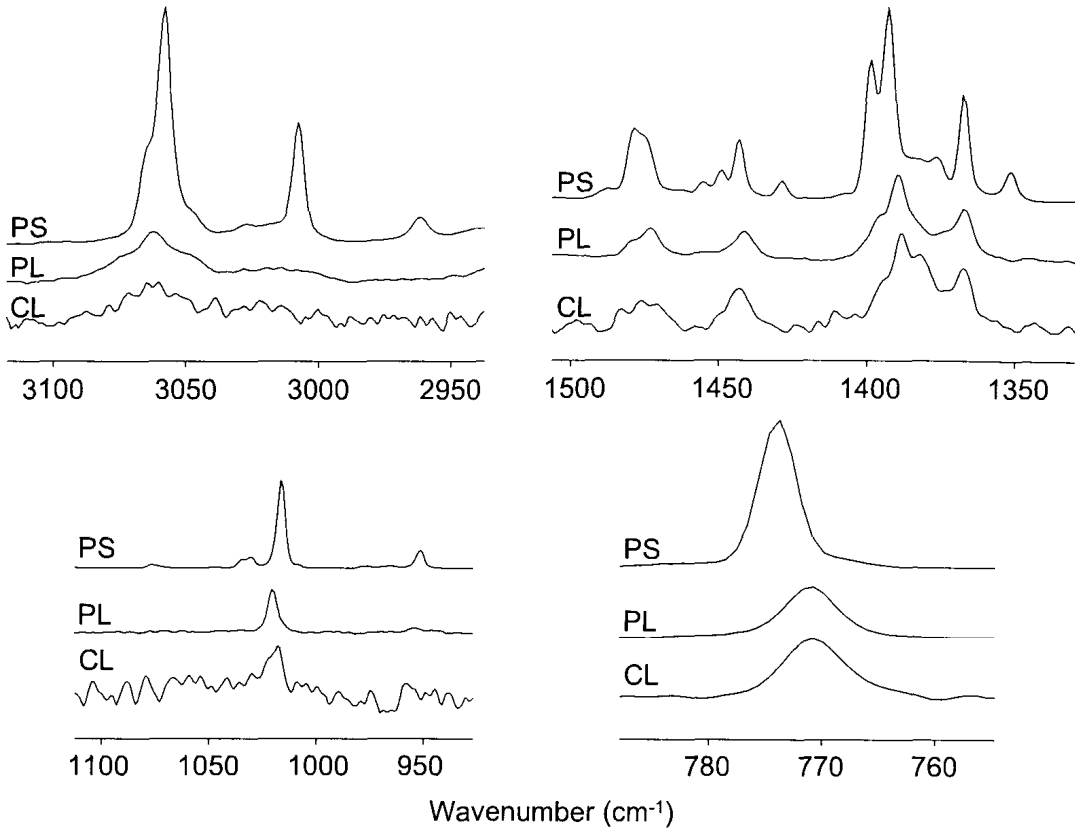

Figure 5.20. Raman spectra of pure solid 2-$C_{10}H_7OCH_3$ (PS), pure liquid 2-$C_{10}H_7OCH_3$ (PL), and 2-$C_{10}H_7OCH_3$ coating the pore walls (CL).

to 450 and 499 cm^{-1} in the liquid and contact layer spectra, respectively. Lastly, we consider the low frequency region of the spectra. As indicated by the dotted line in Figure , peaks arising below 100 cm^{-1} may be due to artifacts and are not considered in our analysis.[29] However, it is clear that there are two peaks above this region at 115 and 142 cm^{-1}; it has been suggested by Librando and Alparone[28] that a peak in this region is indicative of torsion of the methyl group. In the liquid and contact layer spectra, only one weak peak can be seen.

Figure 5.20 presents several peaks from the Raman spectra of pure solid and liquid 2-$C_{10}H_7OCH_3$ and 2-$C_{10}H_7OCH_3$ in the contact layer. The spectra for pure CCl_4 was subtracted from the liquid 2-$C_{10}H_7OCH_3$ in order to reveal peaks of interest

which overlap with CCl_4 vibrations. Several obvious changes can be seen in the 2950-3100 cm^{-1} region. Two aromatic C-H stretches[27] are found in the solid spectrum at 3058 and 3008 cm^{-1}. In the liquid spectrum the high frequency peak is shifted to 3062 cm^{-1}, while the peak at 3008 cm^{-1} decreases in intensity such that it cannot be differentiated from the baseline. The contact layer spectrum shows the same trend. An antisymmetric C-H stretch from the OCH_3 group can be found in the pure solid spectrum at 2962 cm^{-1}; again the intensity of this peaks decreases into the baseline for the pure liquid and contact layer spectra. The 1350 to 1500 cm^{-1} region in Figure 5.20 shows a number of overlapping peaks which correspond to aromatic C-C stretching.[30] Such overlap renders the determination of peak shifts and characteristic changes in the liquid spectrum difficult. To the best of our knowledge, these peaks have not been assigned in the literature for $C_{10}H_7OCH_3$, but it is clear from Figure 5.20 that the overall profile of the contact layer spectrum reflects that of the liquid spectrum and differs from the solid spectrum. The solid peak at 1017 cm^{-1} is also part of the C-C stretching region[30] and is shifted in the liquid and contact layer spectra to 1021 and 1020 cm^{-1}, respectively. The fundamental frequency[31] at 925 cm^{-1} is quite obvious in the solid spectrum but its relative intensity decreases dramatically in the liquid and contact layer spectra. This decrease in intensity can also be seen for the solid doublet at about 1032 cm^{-1}; we have not been able to reference an assignment for this doublet but in comparing the spectra we acquired for naphthalene and its derivatives, we see that it is unique to 2-$C_{10}H_7OCH_3$ and we suggest that it arises from a vibration involving the oxygen of the OCH_3 group. A solid band at 774 cm^{-1}, attributed to a ring breathing motion,[28] is also clearly shifted to a lower frequency of 771 cm^{-1} in the liquid and contact layer spectra.

Lastly, the solid, liquid, and contact layer spectra of 2-$C_{10}H_7Cl$ are presented in Figure 5.21. Assignments are taken from Michaelian and Ziegler[30] and Hanson and Gee.[31] The C-H stretching vibration at 3058 has an FWHH of 11 cm^{-1} in the

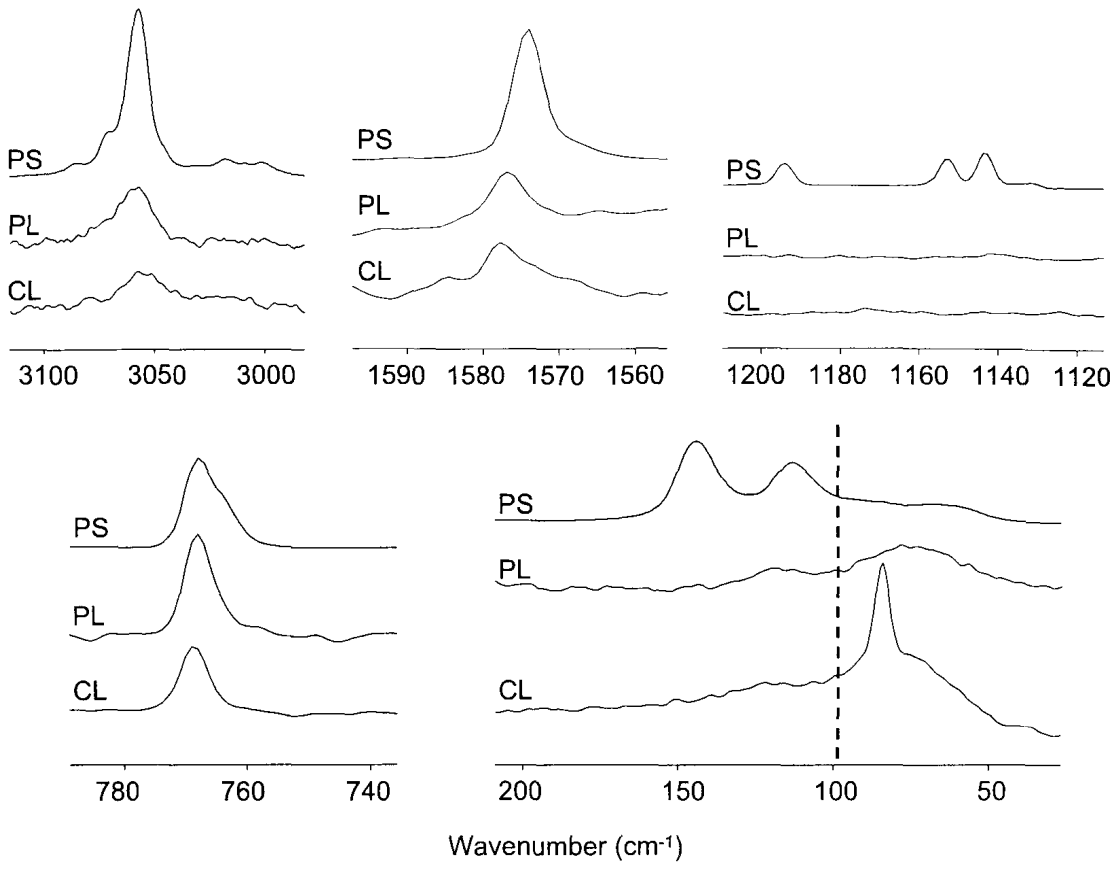

Figure 5.21. Raman spectra of pure solid 2-$C_{10}H_7Cl$ (PS), pure liquid 2-$C_{10}H_7Cl$ (PL), and 2-$C_{10}H_7Cl$ coating the pore walls (CL).

solid spectrum. The peak does not appear to shift significantly in the liquid and contact layer spectra, but the FWHH more than doubles 26 and 30 cm^{-1}, respectively. A C-C stretching vibration at 1574 cm^{-1} in the solid spectrum undergoes a high-frequency shift to approximately 1578 cm^{-1} in the liquid and contact layer spectra. Furthermore, planar C-C-H bending vibrations at 1194, 1153, and 1144 cm^{-1} seen in the solid spectrum all decrease in intensity in the liquid and contact layer spectra, rendering them indistinguishable from the baselines. Band splitting of a C-C stretching vibration at about 769 cm^{-1} in the liquid and contact layer spectra can be seen in the solid spectrum, and the two peaks occur at 765 and 768 cm^{-1}. Finally, in the

low frequency end of the spectra two peaks at 144 and 113 cm^{-1} are quite obvious in the solid spectrum, but only one broad peak can be seen in the other two spectra. We have been unable to assign these peaks from the literature. Again, a dotted line at 100 cm^{-1} is given in the figure to show that lines at lower frequencies may be due to artifacts and are therefore not considered.

For each of 2-$C_{10}H_7CH_3$, 2-$C_{10}H_7OCH_3$, and 2-$C_{10}H_7Cl$, the spectra of the contact layers are in accordance with their corresponding pure liquid spectra but differ from those of the pure solids. Using Raman spectroscopy we were able to show on a molecular level that these three naphthalene derivatives, like naphthalene, remain liquid in the contact layer.

5.5 Conclusions

Because it is important to the understanding of confined phase behaviour to examine the effects of molecular properties, we extended our studies regarding the confined phase behaviour of naphthalene using three 2-substituted derivatives of the molecule. Specifically, we chose 2-$C_{10}H_7CH_3$, 2-$C_{10}H_7OCH_3$, and 2-$C_{10}H_7Cl$ for their differences in electronic properties. Similar to $C_{10}H_8$ we observed an increase in the depression of the phase-transition temperatures for all three systems with decreasing pore size. Although our data agree reasonably with the Gibbs-Thomson equation, we again chose to report our findings based on the modified Gibbs-Thomson equation because we have shown using both DSC and Raman spectroscopy that the contact layer does exist and does not undergo phase change. In this way we were able to account for the thickness t of this layer, and again we have found that it decreases with pore size. Taking t into consideration allows for a more accurate estimate of ΔH in confinement. However, because of the solid-solid transition displayed by 2-$C_{10}H_7Cl$ from 253-320 K which overlaps with the confined phase transition peaks, the value

of t is overestimated in our experiment. The porous volume V_p estimated by this experiment is a further indicator that our data are affected by the overlapping bulk solid-solid transition peak, as we found V_p to be significantly larger than the value found by nitrogen adsorption. In contrast, the V_p values found using 2-$C_{10}H_7CH_3$ and 2-$C_{10}H_7OCH_3$ in the same pore size agree reasonably with the nitrogen adsorption value.

We were able to show using Raman spectroscopy that for each derivative in confinement there is a non-freezing contact layer. Although the differences in the Raman spectra of the pure solid and liquid phases of these derivatives were generally more subtle than the differences in the spectra of solid and liquid $C_{10}H_8$, we were able to see several obvious peak shifts, intensity decreases, and increased FWHHs from the solid to liquid spectra. Comparing the contact layer spectra, acquired at temperatures below the confined melting points, showed that the contact layer spectra resemble the liquid spectra and not the solid spectra. Therefore, confined 2-$C_{10}H_7CH_3$, 2-$C_{10}H_7OCH_3$, and 2-$C_{10}H_7Cl$ in the vicinity of the pore walls exist in the liquid phase even below their respective confined melting points.

In comparing DSC results of $C_{10}H_8$, 2-$C_{10}H_7CH_3$, 2-$C_{10}H_7OCH_3$, and 2-$C_{10}H_7Cl$, we were able to examine the effects of the electron-withdrawing and electron-donating properties of the substituent of each derivative. We expected that 2-$C_{10}H_7OCH_3$ would show the greatest depression of ΔT_m, followed by 2-$C_{10}H_7CH_3$, $C_{10}H_8$, and 2-$C_{10}H_7Cl$ as the pore surfaces of our mesoporous silicas contain hydroxyl groups which interact with the delocalized π system of the fused-ring portion of the four organics. The substituents on the derivatives modify the electron density of their respective π systems, thereby changing the molecules' abilities to form π-type hydrogen bonding with the pore surface. This bonding has been proposed to cause a change in the liquid structure of benzene, such that benzene molecules in the vicinity of the silica surface are oriented to the surface. Melting point depression occurs as a

result, and the degree of orientation depends on the concentration of surface hydroxy groups, or the degree of interaction.[1] Following this reasoning, an increase in the interaction of the pore surface with $C_{10}H_8$ derivatives results in an increase in ΔT_m. However, our results were not as expected; 2-$C_{10}H_7OMe$ and $C_{10}H_8$ show approximately the same ΔT_m depression trend, while that of 2-$C_{10}H_7CH_3$ and 2-$C_{10}H_7Cl$ are comparable. While the greater depression in ΔT_m of 2-$C_{10}H_7OCH_3$ compared to 2-$C_{10}H_7Cl$ can be reasonably explained by electronic effects, our data indicates that it is necessary to consider other effects in order to compare all four molecules. Based on previous studies in the literature,[25] the similar size and shape of the CH_3 and Cl groups cause these two derivatives to interact similarly with the pore wall, resulting in similar ΔT_m trends. Additionally, previous studies[26] regarding the steric inhibition of π-π stacking showed that sterically hindered aryl rings did not undergo close π-π stacking, leading to solid-state properties that parallel those in the solution state. Un-substituted $C_{10}H_8$ does not experience steric hinderance of π-π stacking; thus, interactions between naphthalene rings are undisturbed and the molecules can interact with the silica surface and align parallel to the pore wall. The depression of ΔT_m is therefore increased.[1] However, steric hinderance prevents ordered stacking of 2-$C_{10}H_7CH_3$ and 2-$C_{10}H_7Cl$ molecules, diminishing the ability for the surface to order the molecules. ΔT_m is therefore relatively less depressed. While the methoxy group is a relatively bulky group, its electron donating properties increases the electron density of the aromatic π system the 2-$C_{10}H_7OCH_3$ molecule. This improves its ability to form π-type hydrogen bonds with the silica surface as well as π-π stacking interactions with each other. Furthermore, the oxygen from the methoxy group may also interact favourably with hydrogens on the pore surface, increasing the overall ability of 2-$C_{10}H_7OCH_3$ to interact with the surface. It is clear from our results that besides electronic effects, factors such as molecular size and shape and steric hinderance must be considered in comparing ΔT_m.

References

[1] Takei, T.; Konishi, T.; Fuji, M.; Watanabe, T.; Chikazawa, M. *Thermochim. Acta* **1995**, *267*, 159–167.

[2] Svishchev, I. M.; Plugatyr, A.; Nahtigal, I. G. *J. Chem. Phys.* **2008**, *128*, 124514-1–124514-7.

[3] Lide, D. R. *Enthalpy of Fusion in CRC Handbook of Chemistry and Physics, 88th Edition*; CRC Press/Taylor and Francis, Boca Raton, FL, 2007.

[4] Chanh, N. B.; Haget, Y.; Bonpunt, L.; Meresse, A.; Housty, J. *Anal. Cal.* **1977**, *4*, 233–240.

[5] Bolte, M.; Bauch, C. *Acta Cryst. C* **1998**, *C54*, 1862–1863.

[6] Chanh, N. B.; Haget, Y.; Leroy, F.; Hannoteaux, F. *Acta. Cryst.* **1973**, *29*, 1469–1473.

[7] Chanh, N. B.; Haget, Y.; Meresse, A.; Housty, J. *Mol. Cryst. Liq. Cryst.* **1978**, *45*, 307–312.

[8] Haget, Y.; Bonpunt, L.; Meresse, A.; Chanh, N. B. *Mol. Cryst. Liq. Cryst.* **1983**, *96*, 211–214.

[9] Loyzance, P. L.; Rey-Lafon, M. *J. Phys. Chem. Solids* **1978**, *39*, 967–970.

[10] Faivre, C.; Bellet, D.; Dolino, G. *Eur. Phys. J. B* **1999**, *7*, 19–36.

[11] Dosseh, G.; Xia, Y.; Alba-Simionesco, C. *J. Phys. Chem. B* **2003**, *107*, 6445–6453.

[12] Meziane, A.; Grolier, J.-P. E.; Baba, M.; Nedelec, J. M. *Faraday Discuss.* **2007**, *136*, 384–394.

[13] Meresse, A.; Haget, Y.; Chanh, N. B. *Cryst. Struct. Comm.* **1980**, *9*, 699–703.

[14] Jackson, C. L.; McKenna, G. B. *J. Chem. Phys.* **1990**, *93*, 9002–9011.

[15] Moreno, J.; Sherrington, D. C. *Chem. Mater.* **2008**, *20*, 4468–4474.

[16] Ravishanker, G.; Mehrotra, P. K.; Mezei, M.; Beveridge, D. L. *J. Am. Chem. Soc.* **1948**, *106*, 4102–4108.

[17] Linse, P. *J. Am. Chem. Soc.* **1990**, *112*, 1744–1750.

[18] Schravendijk, P.; van der Vegt, N. F. A. *J. Chem. Theory Comput.* **2005**, *1*, 643–652.

[19] Tsuzuki, S.; Honda, K.; Uchimaru, T.; Mikami, M. *J. Chem. Phys.* **2004**, *120*, 647–659.

[20] Radhakrishnan, R.; Gubbins, K. E.; Sliwinska-Bartkowiak, M. *J. Chem. Phys.* **2000**, *112*, 11048–11057.

[21] Mu, R.; Malhotra, V. M. *Phys. Rev. B* **1991**, *44*, 4296–4303.

[22] Petrov, O.; Furó, I. *Phys. Rev. E* **2006**, *73*, 011608-1 – 7.

[23] Alba-Simionesco, C.; Coasne, B.; Dosseh, G.; Dudziak, G.; Gubbins, K. E.;

Radhakrishnan, R.; Sliwinska-Bartkowiak, M. *J. Phys.: Condens. Matter* **2006**, *18*, R15–R68.

[24] Clayden, J.; Greeves, N.; Warren, S.; Wothers, P. *Organic Chemistry*; Oxford University Press Inc., New York, 2001.

[25] Fyfe, C. A.; Strobl, H.; Gies, H.; Kokotailo, G. T. *Can. J. Chem.* **1988**, *66*, 1942–1947.

[26] Moorthy, J. N.; p. Natarajan,; Venkatakrishnan, P.; Huang, D. F.; Chow, T. J. *Org. Lett.* **2007**, *9*, 5215–5218.

[27] Gussoni, A.; Zerbi, G.; van Es, J. J. G. S.; Biemans, H. A. M.; Meijer, E. W. *Synthetic Met.* **1996**, *80*, 201–204.

[28] Librando, V.; Alparone, A. *Polycycl. Aromat. Comp.* **2007**, *27*, 65–94.

[29] Barron, L. D.; Vrbancich, J. *J. Raman Spectrosc.* **1984**, *15*, 47–50.

[30] Michaelian, K. H.; Ziegler, S. M. *Appl. Spectrosc.* **1973**, *27*, 13–21.

[31] Hanson, D. M.; Gee, A. R. *J. Chem. Phys.* **1969**, *51*, 5052–5062.

Chapter 6

General Conclusions

It is well known that the properties of materials confined in pores differ from those of their bulk counterparts due to geometrical confinement and interaction with the surface of the pore wall.[1] Most commonly observed are the hysteresis between freezing and melting cycles and the shift in phase transition temperatures.[2,3]

Using the Broekhoff-de-Boer Frankel-Halsey-Hill (BdB-FHH) method, we were able to accurately differentiate between cylindrical and spherical geometries based on the pore size distributions calculated from adsorption and desorption isotherm branches and our results are comparable to work done by Lukens *et al.*[4] Using the pore size distributions we were able to determine values for the pore diameters. Transmission electron microscopy imaging provided further evidence of both pore morphology and dimension. Having verified the accuracy of the BdB-FHH method for determination of pore morphology and size, we were able to apply this method to the different pore samples synthesized. We were able to access a range of diameters for both cylindrical and spherical pores by synthesizing several MCM-41, SBA-15, MCF, MTS, and SBA-16 mesoporous silicates. From these samples we selected a series of cylindrical and spherical pores for our studies. The cylindrical system ranges in pore diameter from 2.6 to 8.0 nm, and the spherical system from 6.6 to 28.5 nm.

Using differential scanning calorimetry (DSC) we have shown that confined naphthalene and its 2-substituted methyl-, methoxy-, and chloro- derivatives exhibit

a phase transition temperature depression which is dependent on both pore size and geometry, where a greater degree of confinement results in greater depression. Our results agree reasonably with the Gibbs-Thomson equation, which implies that the melting temperature depression varies inversely with pore radius. However, it is known that in confinement there is a layer near the pore surface which does not undergo phase transitions; instead it is non-freezing and remains in the liquid state. The modified Gibbs-Thomson equation, which accounts for the thickness t of this contact layer, is therefore used in the determination of ΔH in confinement. Although t has sometimes been assumed constant, this assumption is unreasonable for our case and we have found that t generally decreases with decreasing pore size.

The origin of hysteresis in confinement differs from that of the bulk and is related to the differences in pore geometry of the two systems, specifically the surface-to-volume ratios and curvatures.[5] We have found that hysteresis generally increases with decreasing pore size in both the spherical and cylindrical systems. The increase in ΔT_f relative to ΔT_m is 1.6 times faster for spherical pores than cylindrical pores, and this trend is consistent with the literature.[5] From our data, we find that the relationship between hysteresis and pore radius for both geometries cannot be linear, as this would imply that hysteresis becomes negative as pore size increases. We therefore propose that the change in hysteresis is exponential and approaches zero for large pores. Moreover, the difference in hysteresis values calculated for a range spherical and cylindrical pores ($Hyst_{sph} - Hyst_{cyl}$) of comparable radii decreases exponentially with increasing effective pore radius. At approximately 26 nm, however, the $Hyst_{sph} - Hyst_{cyl} = 0.0$ and hysteresis appears to become independent of pore geometry.

In order to address the question of whether or not confinement causes a change in crystal structure, we used powder X-ray diffraction to examine solid $C_{10}H_8$ in confinement. We found that there was no difference in the powder patterns of the

solid and bulk $C_{10}H_8$, meaning that the crystal structure is the same. However, there is a lattice expansion indicated by the shifting of the reflections in the confined pattern to lower 2θ angles. The resulting lattice expansion inside the pore occurs due to the interfacial energy and surface tension attraction in confinement.[6] In comparing the spectra of bulk and confined $C_{10}H_8$ we have found that there is a global line broadening of up to 0.18° in the confined spectrum, further verifying that the shift in 2θ occurred as a result of confinement.

We have also demonstrated on a molecular level using Raman spectroscopy that the contact layers of confined $C_{10}H_8$ and its derivatives are indeed non-freezing. Through frequency shifts, band splitting, and intensity changes we were able to differentiate solid from liquid spectra and compare our spectra of the respective contact layers with them. In all cases, the contact layer spectrum resembles that of the pure liquid, but not the pure solid.

In comparing DSC results of $C_{10}H_8$, 2-$C_{10}H_7CH_3$, 2-$C_{10}H_7OCH_3$, and 2-$C_{10}H_7Cl$, we examined the effects of the electron-withdrawing and electron-donating properties of the substituent of each derivative. The pores contain surface hydroxyl groups which interact with the delocalized π system of the fused-ring portion of the four aromatics. Substituents on the derivatives modify the electron density of the π system, thereby reducing or increasing its ability to form π-type hydrogen bonding with the pore surface. This bonding has been proposed to cause a change in the liquid structure of aromatic molecules in the vicinity of the silica surface such that they become ordered along the pore walls.[7] Melting point depression occurs as a result, and the degree of orientation depends on the concentration of surface hydroxy groups, or the degree of interaction. We have found that 2-$C_{10}H_7OMe$ and $C_{10}H_8$ show approximately the same ΔT_m depression trend, whereas that of 2-$C_{10}H_7CH_3$ and 2-$C_{10}H_7Cl$ are comparable. While the greater depression in ΔT_m of 2-$C_{10}H_7OCH_3$ compared to 2-$C_{10}H_7Cl$ can be reasonably explained by electronic effects, it is necessary to consider

other effects in order to compare all four compounds. The similar size and shape of the CH_3 and Cl groups cause their respective 2-substituted naphthalene derivatives to interact similarly with the pore wall,[8] resulting in similar ΔT_m trends. Furthermore, steric hinderance prevents stacking of 2-$C_{10}H_7CH_3$ and 2-$C_{10}H_7Cl$ molecules, impeding the ability for the surface to order the molecules. ΔT_m is therefore relatively less depressed. The oxygen from the methoxy group may also interact favourably with hydrogens on the pore surface, increasing the overall ability of 2-$C_{10}H_7OCH_3$ to interact with the surface. From our results, it is clear that besides electronic effects, factors such as molecular size and shape and steric hinderance must be considered in explaining the trends of ΔT_m for confined aromatic systems.

References

[1] Smirnov, P.; Yamaguchi, T.; Kittaka, S.; Kuroda, Y. *J. Phys. Chem. B* **2000**, *104*, 5498–5504.

[2] Mu, R.; Zue, Y.; Henderson, D. O.; Frazier, D. O. *Phys. Rev. B* **1996**, *53*, 6041–6047.

[3] Morishige, K.; K., K. *J. Chem. Phys.* **2000**, *112*, 11023–11029.

[4] Lukens, W. W., Jr; Schmidt-Winkel, P.; Zhao, D.; Feng, J.; Stucky, G. D. *Langmuir* **1999**, *15*, 5403–5409.

[5] Petrov, O.; Furó, I. *Phys. Rev. E* **2006**, *73*, 011608–1 – 7.

[6] Wei, Z.; Xia, T.; Ma, J.; Feng, W.; Dai, J.; Wang, Q.; Yan, P. *Mat. Char.* **2007**, *58*, 1019–1024.

[7] Takei, T.; Konishi, T.; Fuji, M.; Watanabe, T.; Chikazawa, M. *Thermochim. Acta* **1995**, *267*, 159–167.

[8] Fyfe, C. A.; Strobl, H.; Gies, H.; Kokotailo, G. T. *Can. J. Chem.* **1988**, *66*, 1942–1947.